UNIVERSITÀ DEGLI STUDI DI URBINO "CARLO BO"

Dipartimento di Scienze Pure e Applicate

Ph.D. Programme in:
Research methods in Science and Technology
Cycle XXXVI

A search for Gravitational Waves signals emitted by Binary Black Holes systems with precessing spins

SSD: FIS/01

Coordinator: Prof.
Alessandro Bogliolo

Supervisor: Prof.
Gianluca M. Guidi

Ph.D. student:
Maria Assiduo

Academic Year 2022/2023

Contents

List of Figures

List of Tables

Abstract

During the inspiral of two merging black holes, if the spin of one or of both bodies are misaligned with respect to the orbital angular momentum $\hat{L}$, the total spin $\hat{S}$ and $\hat{L}$ will have a precessing motion around the direction of the total angular momentum $\hat{J}$ of the system. The orbital plane of the system will also precess over time due to the general relativistic spin-spin and spin-orbit interactions. The imprinting of the precession will appears as phase and amplitude modulations in the observed signal, thus precessing gravitational waves will have a more rich structure than the charasteristic chirp-shape of the aligned-spin ones. These precession-induced modulations will be important not only for waves from binary black holes which lie in the current LIGO-Virgo frequency band sensitivity, but also for waves emitted by supermassive BBH and for binary neutron stars mergers or stellar mass BH spiraling into supermassive black holes (these low frequency gravitational waves will be the target signals for space based GW detectors like LISA). Imprints of precession have been investigated in several signals of the current $\simeq 90$ BBH detections of Advanced LIGO and Virgo detectors, and there are almost two signals with evidence of marginal precession: GW190412 [3] and GW200129 [4]. In addition, the observation of GW signals with precession not only have the goal to test General Relativity in strong field regime and to study binary formation channels using spin-distribution population [5], [6], but the most promising challenge is to improve the performance of early warning alerts for electromagnetic follow-up of the GW sources [7]. In this research work a search for GW signals emitted by BBH with precession of the spins is proposed. The thesis is divided in five chapters organized as follow: the first chapter is dedicated to an introduction of GWs, who's existence is predicted by the theory of General Relativity. After showing that they are solutions of Einsten's linearized field equations, an useful formalism used to describe the interaction between a GW and a detector is illustrated. Also, the main astrophysical sources of GWs are described; In the second chapter GW detectors and the interferometric technique are described. In addition, several noise sources at different frequency ranges which affect the detectors output data are illustrated. In the third chapter the theory of precession of spins in BBH systems is introduced. In particular, the *simple precession* motion, which occurs when the direction of the binary's total angular momentum is approximatly constant in time, will be analized and the equations to describe the orbital plane of the system and the spin-induced modulations in the gravitational signature will be derived. The fourth and the fifth chapters contain the main contribution of this work. In the fourth chapter the tools Sbank and Banksim of the pipeline PyCBC are described, used for the generation of the precessing-spin and aligned-spin template banks and the computation of their effectualness respectively. In the fifth chapter, first an outline of the pipeline MBTA based on the matched-filtering technique is depicted; then the results of Monte Carlo tests, performed running MBTA to analize the capability of the template banks to recover simulated signals of GW with precession of the spins in Gaussian noise and in a file of O3 data, are discussed.

"Un punto microscopico brilla,
poi un altro, poi un altro: è l'impercettibile,
è l'enorme. Questo lumicino è un focolare,
una stella, un sole, un universo;
ma questo universo è niente. Ogni numero è zero
di fronte all'Infinito. L'inaccessibile unito
all'impenetrabile, l'impenetrabile unito
all'inespicabile, l'inespicabile unito
all'incommensurabile: questo è il cielo."
Victor Hugo, Les contemplations

Chapter 1

Gravitational Waves Astronomy

Albert Einstein, more than 100 years ago in his General Relativity (GR) theory, described no longer the Gravity as a force acting in a flat space-time: Gravity is embedded in the geometry of the space-time determined by the energy and momentum contents of the Universe. Gravitational Waves (GWs) are oscillations of the space-time metric which, accordingly to GR, propagate in the free space with the speed of light in vacuum. Their coupling with matter and radiation is extremely weak making them very challenging to detect. Astrophysical objects with extremly high accelerations generate waves of distorted space-time carrying away energy and momentum from the source, and in 2015 the two LIGO (Laser Interferometer Gravitational Wave Observatory) Interferometers in USA detected for the first time a GW signal emitted by the coalescence of two black holes orbiting each other in a binary system, matching the predictions of GR. This event is a milestone in physics and marked the beginning of the Gravitational Wave Astronomy, providing not only the first direct proof of the existence of GWs, but also the first direct evidence of the existence of black holes. Few years later, in 2017, the first GW signal emitted by the merger of a pair of neutron stars was discovered. Unlike all previous GW detections, corresponding to BBH mergers and not expected to produce a detectable electromagnetic signal, the aftermath of this merger was seen by 70 observatories across the world in the electromagnetic spectrum, marking the beginning of the Multi-Messenger Astronomy between GWs and Electromagnetic radion.
In the first chapter will be introduced the Einstein's GR theory and the linearized Einstein's field equations, then will be decribed how GWs propagate in a flat space-time as waves with two independent polarizations and the properties of their sources.

1.1 From Einstein's equations to Gravitational Waves

The theory of GR describes space-time as a four-dimensional variety with a pseudo-Riemannian metric. By choosing a local coordinate system x_μ, the infinitesimal length ds is expressed as a function of the infinitesimal change in coordinates dx^μ, and the metric tensor $g_{\mu\nu}$ which rapresent the distance element between two events, evaluated in a given space-time point x, is given by:

$$ds^2(x) = g_{\mu\nu}(x)dx^\mu dx^\nu \tag{1.1}$$

In order to find $g_{\mu\nu}$ and the equations of motion for matter and energy, Einstein's field equations must be solved:

$$R_{\mu\nu} - \frac{1}{2}g_{\mu\nu}R = \frac{8\pi G}{c^4}T_{\mu\nu} \tag{1.2}$$

where $R_{\mu\nu} = R^{\lambda}_{\mu\lambda\nu}$ and $R = g_{\mu\nu}R^{\mu\nu}$ are the Ricci's tensor and the Ricci's scalar respectively, $G = 6,67 \cdot 10^{-11}Nm^2/kg^2$ is the gravitational constant, $c = 3 \cdot 10^8 m/s$ is the speed of light, $T^{\mu\nu}$ is the energy-momentum tensor that describes the distribution and evolution of mass and energy densities in space-time, in particular the components T_{00} and T_{i0} correspond to the mass and momentum densities respectively[1]. The constant term $8\pi G/c^4$ it is required to reproduce the Newtonian limit in the case of weak field and non relativistic motion. Equation 1.2 can be interpreted as follows: matter defines the geometry of space-time, geometry determines the motion of matter[2], which means that the distribution of matter and its motion cannot be described independently from the gravitational field generated by them and the Gravity represent the curvature of space-time. The equations 1.2 corresponds to a 10 coupled, non-linear, partial derivatives equations system, (since the Ricci's tensor $R_{\mu\nu}$ depends on the first and second partial derivatives of the metric tensor $g_{\mu\nu}$ which in turn is coupled to the GW's source $T_{\mu\nu}$). To solve them one can take advantage of the Einstein's Principle of Equivalence, which in its more general formulation asserts that it's always possible to choose a reference system in space-time such that, around each event $\bar{x}^{\mu}$, it's possible to define a system of locally inertial coordinates for which the effects of acceleration due to the gravitational field are null:

$$g_{\mu\nu}(\bar{x}) = \eta_{\mu\nu} \tag{1.3}$$
$$\partial_{\rho}g_{\mu\nu}(\bar{x}) = 0 \tag{1.4}$$

That is, the gravitational field propagates in a flat space-time described by the Minkowski metric $\eta_{\mu\nu}$. Suppose we are interested in to find the solutions for a source with $T_{\mu\nu} = 0$; the solutions are given by small perturbations of the flat space-time metric, and it is possible to write the metric tensor as the sum of a perturbative term $|h_{\mu\nu}| \ll 1$ and the metric tensor of Minkowski's flat space-time $\eta_{\mu\nu}$:

$$g_{\mu\nu} = \eta_{\mu\nu} + h_{\mu\nu} \tag{1.5}$$

with

$$\eta_{\mu\nu} = \begin{bmatrix} -1 & 0 & 0 & 0 \\ 0 & 1 & 0 & 0 \\ 0 & 0 & 1 & 0 \\ 0 & 0 & 0 & 1 \end{bmatrix}$$

The assumptions we made define the so-called weak field approximation or the linearized GR theory and allow to write the Einstein's equations in a flat space-time. The

---

[1]The Latin indices indicate the spatial components, the Greek indices the spatio-temporal components.

[2]J. A. Wheeler, in Geons, Black Holes, and Quantum Foam (2000),p. 235.

only contractions of the Riemann tensor are the Ricci tensor and the scalar of curvature R, therefore in the first order in $h_{\mu\nu}$ the Riemann tensor becomes:

$$R_{\mu\nu\rho\sigma} = \frac{1}{2}(\partial_\nu\partial_\rho h_{\mu\sigma} + \partial_\mu\partial_\sigma h_{\nu\rho} - \partial_\mu\partial_\rho h_{\nu\sigma} - \partial_\nu\partial_\sigma h_{\mu\rho}) \tag{1.6}$$

replacing this expression in 1.2, we obtain the linearized field equations:

$$\Box \bar{h}_{\mu\nu} + \eta_{\mu\nu}\partial^\rho\partial^\sigma \bar{h}_{\rho\sigma} - \partial^\rho\partial_\nu \bar{h}_{\mu\rho} - \partial^\rho\partial_\mu \bar{h}_{\nu\rho} = -\frac{16\pi G}{c^4}T_{\mu\nu} \tag{1.7}$$

where $\Box = \eta_{\mu\nu}\partial^\mu\partial^\nu = \partial_\mu\partial^\mu$ is the D'Alambertian operator of the flat space-time and for a more compact form of the eq.1.7, the metric perturbation "trace-reversed" has been introduced:

$$\bar{h}_{\mu\nu} = h_{\mu\nu} - \frac{1}{2}\eta_{\mu\nu}h \tag{1.8}$$

$$h = \eta^{\mu\nu}h_{\mu\nu} \tag{1.9}$$

It should be noted that $-h = h - 2h = \eta^{\mu\nu}\bar{h}_{\mu\nu} = \bar{h}$, therefore the above expressions can be inverted. it is possible to choose the Lorenz gauge $\partial^\nu\bar{h}_{\mu\nu} = 0$ which provides 4 conditions for the symmetric matrix $\bar{h}_{\mu\nu}$, reducing the 10 independent components to 6. In this gauge the last 3 terms in the left part of the eq. 1.7 are zero and we obtain a wave equation:

$$\Box \bar{h}_{\mu\nu} = -\frac{16\pi G}{c^4}T_{\mu\nu}. \tag{1.10}$$

The Lorenz gauge and the eq. 1.10 together imply that $\partial^\nu T_{\mu\nu} = 0$, which represents the law of energy-momentum conservation in the GR linearized theory. In the next paragraph an advantageous reference frame to study GW will be introduced.

1.1.1 The Gauge Transformations

In order to study the properties of GW and their interaction with matter (including a detector), one should explore the properties of the eq. 1.10 away from the source, that is for $T_{\mu\nu} = 0$. The associated homogeneous eq. of the eq. 1.10 is defined as:

$$\Box \bar{h}_{\mu\nu} = 0 \tag{1.11}$$

where $\Box = \nabla^2 - (1/c^2)\partial_0{}^2$. The eq. 1.11 provides the existence of a free gravitational field that travels at the speed of light in vacuum. The Lorenz gauge does not completely solve the gauge invariance, but choosing $\bar{h} = 0$ we obtain $\bar{h}_{\mu\nu} = h_{\mu\nu}$ and the Lorenz condition became:

$$\partial^0 h_{00} + \partial^i h_{0i} = 0 \tag{1.12}$$

the additional condition $h_{0i} = 0$ implies that $\partial^0 h_{00} = 0$, then the Newtonian potential h_{00} of the source that generated the GW, becomes constant over time. For the spatial

components h_{ij} the Lorenz condition reads $\partial^j h_{ij} = 0$. We now define the Transverse-Traceless gauge (TT-gauge) [1]:

$$h^0{}_\mu = 0; h^i{}_i = 0; \partial^i h_{ij} = 0 \qquad (1.13)$$

In the TT-gauge the symmetric matrix $h_{\mu\nu}$ is further reduced to only 2 degrees of freedom (d.o.f.) which correspond to the two GW polarizations. We will indicate the metric in the TT-gauge with h_{ij}^{TT}. A generic solution of the eq. 1.11 can be written as a superposition of plane waves $h_{ij}^{TT}(x) = \epsilon_{ij}(\mathbf{k})e^{i\mathbf{k}_\mu \mathbf{x}^\mu}$, where $\mathbf{k} = (\omega/c, \vec{k})$ is the wave vector, and $\epsilon_{ij}(\mathbf{k})$ is defined as the polarization tensor. The non-zero components of h_{ij}^{TT} lies in the plane transverse to the direction of the propagation vector. In the particular case of a wave traveling in the direction $\hat{z}$, with $\mathbf{k} = (\omega, 0, 0, \omega/c)$, one has [8]:

$$\epsilon_{ij} = h_+ \epsilon_{ij}^+ + h_\times \epsilon_{ij}^\times \qquad (1.14)$$

where h_+ and $h_\times$ define the plus and cross GW's amplitudes respectively:

$$\epsilon^+ = \begin{bmatrix} 0 & 0 & 0 & 0 \\ 0 & 1 & 0 & 0 \\ 0 & 0 & -1 & 0 \\ 0 & 0 & 0 & 0 \end{bmatrix}$$

$$\epsilon^\times = \begin{bmatrix} 0 & 0 & 0 & 0 \\ 0 & 0 & 1 & 0 \\ 0 & 1 & 0 & 0 \\ 0 & 0 & 0 & 0 \end{bmatrix}$$

A general solution can be written in an intuitive form as follows:

$$h_{ab}^{TT}(t,z) = \begin{bmatrix} h_+ & h_\times \\ h_\times & -h_+ \end{bmatrix}_{ab} \cos[\omega(t - z/c)]$$

plus an arbitrary phase in the cosine, where *a,b* are the indices in the transverse plane x-y. The reference system corresponding to the TT-gauge will be indicated as TT-frame. Note that the TT-frame is not the reference system normally used in experiments, infact it can be shown that in this frame any test particles that are at rest before the arrival of a GW, remain at rest after the passage of the wave. In the next section we describe the effects of a GW interacting with a ring of test masses.

1.1.2 Gravitational Waves propagation and interaction with matter

Let be an idealized detector rapresented by a ring of free-falling masses. In GR the trajectory of an object under the influence of gravity only is called geodesic, and the geodesic deviation equation relates the Riemann curvature tensor to the relative acceleration of two neighboring geodesics. So if $\xi^\mu = x_2^\mu - x_1^\mu$ is the four-vector distance between two free falling masses, the motion equation is given by [8]:

$$\frac{D^2 \xi^\mu}{D\tau^2} + R^\mu{}_{\nu\rho\sigma} \xi^\rho \frac{dx^\nu}{d\tau}\frac{dx^\sigma}{d\tau} = 0 \qquad (1.15)$$

where $D/D\tau$ is the covariant derivative. In the weak field approximation the eq. 1.15 can be written as:

$$\frac{d^2\xi^i}{d\tau^2} + R^i_{0j0}\xi^j\left(\frac{dx^0}{d\tau}\right)^2 = 0 \qquad (1.16)$$

which represents the classical equation of the tidal force. The Riemann tensor R^i_{0j0} is of the order $o(h)$, since we are neglecting all the background effects. Limiting ourselves to considering only the terms of linear orders in h, the proper time τ measured by a clock placed on a test particle initially at rest is equal to the time of the coordinates t, and one can write $t = \tau$ and $dx^0/d\tau = c$, so the previous eq.1.16 becomes:

$$\ddot{\xi}^i = -c^2 R^i_{0j0}\xi^j \qquad (1.17)$$

The next step is to compute the tensor R^i_{0j0} in the detector's own reference frame. Since in the GR linearized theory the Riemann tensor is invariant, it's convenient to compute it in the TT-frame and we obtain $R^i_{0j0} = -1/2c^2\ddot{h}^{TT}_{ij}$. Finally, the geodesic deviation equation in the detector's own reference frame becomes [8]:

$$\ddot{\xi}^i = \frac{1}{2}\ddot{h}^{TT}_{ij}\xi^j \qquad (1.18)$$

which allows us to immediately write the effects of a GW interacting with particles of mass m in terms of a Newtonian force (also called Riemann force):

$$F_i = \frac{m}{2}\ddot{h}^{TT}_{ij}\xi^j \qquad (1.19)$$

Ground-based GW detectors are in a non-inertial reference frame (due to Earth's rotation motion), however thanks to the eq. 1.19 the detector's response to GW can be analyzed in Newtonian limit. The effects of GWs cannot be seen on isolated bodies, infact a single test mass in a reference in free fall with it remains at rest. Let's consider now a ring of particles of mass m initially at rest in the proper reference of the detector. By fixing the origin in the center of the ring, ξ^i describes the distance of the mass from the origin. If the ring is placed in the x-y plane and the GW propagates in the $\hat{z}$ direction, then the components of h^{TT}_{ij} with $i = 3, j = 3$ are null, a particle initially placed in $z = 0$ remains in this position even after the passage of the GW. Let's consider a plus polarized GW ($h_\times = 0$) and let be $h^{TT}_{ij} = 0$ with the initial conditions $z = 0$ e $t = 0$, we have:

$$h^{TT}_{ab} = h_+ \sin\omega t \begin{bmatrix} 1 & 0 \\ 0 & -1 \end{bmatrix}$$

Indicating with x_0, y_0 the unperturbed positions, and with $\delta x(t), \delta y(t)$ the displacements induced by the GW, from the eq. 1.18 we can compute:

$$\begin{aligned} \delta\ddot{x} &= -\frac{h_+}{2}(x_0 + \delta x)\omega^2\sin\omega t \\ \delta\ddot{y} &= \frac{h_+}{2}(y_0 + \delta y)\omega^2\sin\omega t \end{aligned} \qquad (1.20)$$

Notice that δx is of the order $o(h_+)$ on the right side, therefore the terms $\delta x, \delta y$ can be neglected with respect to x_0, y_0. Integrating the eq. 1.20 we get:

$$\delta x(t) = \frac{h_+}{2} x_0 \sin \omega t$$
$$\delta y(t) = -\frac{h_+}{2} y_0 \sin \omega t$$

(1.21)

Similarly, for a cross polarized GW ($h_+ = 0$) and with the same initial conditions, one has:

$$\delta x(t) = \frac{h_x}{2} y_0 \sin \omega t$$
$$\delta y(t) = -\frac{h_x}{2} x_0 \sin \omega t$$

(1.22)

The resulting displacements are shown in the figure 1.1. The effect of a GW interacting
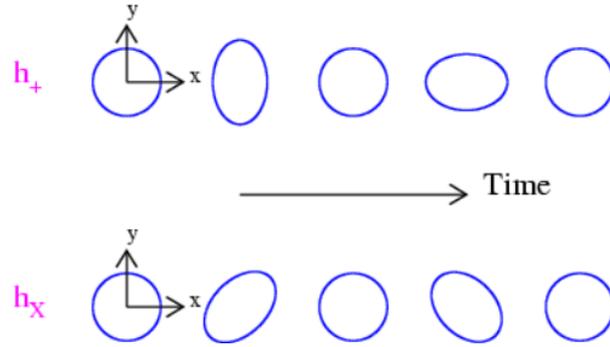
Figure 1.1: Graphical rapresentation of the effects of polarized waves (top + polarization, bottom × polarization).

with free-falling masses is to vary the relative distances along the directions perpendicular to the waves propagation direction. The effect is proportional to the distance between the masses. In particular, a plus polarized GW alternately stretches and compresses the ring of particles in the x and y directions, while a cross polarized GW exhibits the same behavior in the rotated direction of $\pi/4$. Within the GR it's not possible to define a local energy carried by a single wave. What one can do is to compute an integrated average of the energy-momentum tensor, on a region of space-time smaller compared to the background curvature. In such conditions the energy carried by a plane wave turns out to be:

$$T_{00}^{GW} = \frac{c^4}{16\pi G} < \dot{h}_+^2 + \dot{h}_x^2 >$$

(1.23)

and also:

$$\partial_i F_i = \frac{m}{2} \ddot{h}_{ij}^{TT} \delta_{ij} = 0$$

(1.24)

since h_{ij}^{TT} has null trace, the Newtonian force has null divergence. By drawing the lines of force in the x-y plane for the polarized waves h_+ and $h_\times$ shown in the figure 1.2 , it is

6

observed that the axes of symmetry have a typical quadrupolar model, which highlights the difference between electromagnetic (vector field) and gravitational (tensor field) radiation. The physical effects of GW can be evaluated, alternatively, considering the
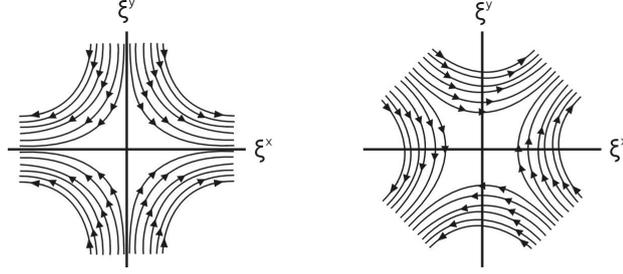
Figure 1.2: Lines of force corresponding to the "plus" on the left and "cross" on the right polarizations of the GW. The arrows follow the direction of the force when $\sin \omega t$ is positive, they go in the opposite direction if $\sin \omega t$ is negative. [1].

proper distances [1]. The perturbed metric in terms of the polarizations h_+ and $h_\times$ can be used to write the invariant interval as:

$$
ds^2 = -c^2 dt^2 + dz^2 + 1 + h_+ cos[\omega(t - z/c)]dx^2 +
$$
$$
1 - h_+ cos[\omega(t - z/c)]dy^2 + 2h_\times \cos[\omega(t - z/c)]dxdy \tag{1.25}
$$

Consider now two events with coordinates $(t, x_1, 0, 0)$ and $(t, x_2, 0, 0)$. In the TT-gauge the distance $x_2 - x_1 = L$ remain constant, even if there is a GW which propagates along the $\hat{z}$ axes. While, the proper distance s between the two events, in linear terms in h_+, is given by:

$$
s = L[1 + h_+ \cos \omega t]^{\frac{1}{2}} \simeq L[1 + \frac{1}{2}h_+ \cos \omega t] \tag{1.26}
$$

that is, the proper distance changes periodically over time due to the GW. In order to find the geodesic equation in terms of the proper distance, let be L the distance vector between the two events, thus $s^2 = L^2 + h_{ij}(t)L_iL_j$. In linear terms in h it is possible to write $s \simeq L + h_{ij}(L_iL_j/2L)$ which implies:

$$
\ddot{s} \simeq \frac{1}{2}\ddot{h}_{ij}\frac{L_i}{L}L_j \tag{1.27}
$$

If $L_i/L = n_i$ and defining $s_i = s/n_i$, we obtain:

$$
\ddot{s}_i \simeq \frac{1}{2}\ddot{h}_{ij}L_j \simeq \frac{1}{2}\ddot{h}_{ij}s_j \tag{1.28}
$$

where the identity $L_j = s_j$ was used, valid for lower orders. The 1.28 is the equation searched. If two mirrors play the role of free masses, between which a beam of laser light makes a round trip, it is the proper distance between the mirrors that determines the time taken by the light for the path, consequently it is possible to reveal the effects of GW by measuring this "round-trip" time. The application of this principle to a gravitational interferometer will be discussed in the second chapter.

1.1.3 Gravitational Waves Energy

The eq. 1.11 is valid in vacuum, in order to identify the properties of the GW sources it's necessary to solve the eq. 1.10 when $T_{\mu\nu} \neq 0$. By choosing the Gauge condition such that [8]:

$$\partial_\mu h^\mu_\nu = \frac{1}{2} \partial_\nu h^\mu_\mu \tag{1.29}$$

we have:

$$\Box h_{\mu\nu} = -\frac{16\pi G}{c^4}[T_{\mu\nu} - \frac{1}{2}\eta_{\mu\nu}T^\lambda_\lambda] \tag{1.30}$$

The eq. 1.30 it's a non-homogeneous equation of known solution (called retardet potential):

$$h_{\mu\nu}(t, \vec{x}) = \frac{4G}{c^4} \int d^3\vec{x} \frac{[T_{\mu\nu} - (1/2)\eta_{\mu\nu}T^\lambda_\lambda]_{t-r/c}}{|\vec{x} - \vec{x'}|} \tag{1.31}$$

Assuming that the size of the source R is very small compared to the distance of the observation point and to the wavelength λ of the emitted GW, it is possible to carry out a multipoles series expansion similarly to what is done in electromagnetism (this expantion allows to approximate, at great distances, the electric potential generated by a system of elettric charges). It can be demonstrated that, as a consequence of the conservation laws of the total momentum and of the angular momentum, the quadrupole expantion is the first efficient non-null term for GW radiation. To determine the components of the quadrupole momentum tensor we use an analogy with the electromagnetic case [9]. Defined the electric quadrupole tensor as:

$$Q_{jk} = \sum_i q_i(x_{ij}x_{ik} - \frac{1}{3}\delta_{jk}r_i^2) \tag{1.32}$$

replacing the charge q with a continuous mass distribution ρ, in the TT-gauge the projection of the mass quadrupole tensor I_{jk} is given by:

$$I_{jk} = \int \rho(x_j x_k - \frac{1}{3}\delta_{jk}r^2)d^3x \tag{1.33}$$

Thus for the amplitude we get[3]:

$$h_{jk}^{TT} = \frac{2G}{rc^4}\left(\frac{d^2 I_{jk}^{TT}}{dt^2}\right)_{t-r/c} \tag{1.34}$$

Note that there is no radiation associated with a time-varying mass monopole or dipole, meaning that an object undergoing a spherically-symmetric collapse or explosion does not radiate. The power emitted in the electromagnetic case is given by $\dot{E}_{el} = 1/(20c^5)Q_{ij}^{(3)}Q_{jk}^{(3)}$, where (3) indicates the third derivative with respect to time. Therefore we can express the power emitted in GW as:

$$\dot{E}_{GW} = \frac{G}{5c^5}\left\langle I_{jk}^{(3)} I_{jk}^{(3)} \right\rangle \tag{1.35}$$

---

[3]This is a solution obtained by integrating a delayed Green function, hence the delay time t-r/c.

where the angle brackets indicate a value averaged over the set of frequencies of the quadrupole motions. It is now possible to estimate the order of magnitude of the energy emitted in the form of GW from a source. Consider a body with mass M, size R, with the quadrupole tensor varying in times of scale T, we have:

$$I_{jk}^{(3)} \approx \frac{MR^2}{T^3} \tag{1.36}$$

from the eq. 1.35 we get:

$$\dot{E}_{GW} \approx \frac{G}{c^5}\left(\frac{MR^2}{T^3}\right)^2 \approx \frac{G}{c^5}\left(\frac{Mv^3}{R}\right)^2 \approx L_0\left(\frac{v}{c}\right)^6\left(\frac{R_S}{R}\right)^2 \tag{1.37}$$

where we introduced $v = R/T$ the speed of the body, the constant $L_0 = c^5/G = 3,6 \cdot 10^{59} erg/s$, and $R_S = 2GM/c^2$ the Schwarzschild radius associated to the mass M. Note that the weak field approximation for a self-gravitating system is equivalent to neglect the velocities of the internal motions typical of the source, so $v/c \ll 1$. If we consider an astrophysical system that satisfies the virial theorem, we have:

$$\frac{GM^2}{R} \approx Mv^2 \tag{1.38}$$

from which $R_S/R \approx v^2/c^2$, and the eq. 1.37 becomes:

$$\dot{E}_{GW} \approx L_0\left(\frac{R_S}{R}\right)^5 \tag{1.39}$$

It can be deduced from the eq. 1.39 that the power emitted in the form of GW increases as the source approaches its Schwarzschild radius, therefore the emission of GW assumes importance for relativistic and compact objects. From the eq.1.33 one can derive the order of magnitude of the amplitude of the GW emitted:

$$h \approx \frac{G}{rc^4}\frac{MR^2}{T^2} \approx \frac{R_S}{r}\left(\frac{v}{c}\right)^2 \tag{1.40}$$

where r is the distance of the astrophysical source. In order to give an example, for a source in the Virgo cluster of galaxies (about $10\ Mpc$ from Earth)[4] we typically have $h \approx 10^{-21}$. To this end, it is important to understand what frequency the GW emitted must have in order to be detectable from Earth, that is, they enter in the sensitivity frequency band of the interferometers. The maximum frequency of a GW is found to be:

$$f \leq \frac{c^3}{4\pi GM} \simeq 10^4 Hz\frac{M_\odot}{M} \tag{1.41}$$

From now on the Sun will be identified by the symbol $\odot$ and its mass by $M_\odot$, which cames from its hyerogliphic rapresentation.

---

[4]The parsec (symbol pc and meaning parallax of one arcsecond) is used in astronomy to measures distances to objects outside the Solar System. It corresponds to approximately 3.26 light-years.

1.2 Sources of Gravitational Waves

The equations of Einstein's GR theory couple the metric of space-time with the energy and momentum of matter and radiation, thus providing the mechanism to generate GW as a consequence of radially asymmetric accelerations of masses. At largest scales (low frequencies $10^{-15} - 10^{-18} Hz$) the expected sources can be classified as:

- *Stochastic sources*: fluctuations of the primordial Universe;

- *Extreme Inspiral*: Supermassive black holes binaries, formed when galaxies merged.

At lower scales (high frequencies $10^{-4} - 10^4$Hz) the expected sources can be identified as:

- *Continuous sources*: Pulsars or mini mountains on neutron stars (caused by phase transitions on the crust);

- *Inspiral sources*: stellar mass black holes binaries, neutron stars binaries, neutron star- black hole binaries, characterized by a coalescence time smaller than the age of the Universe;

- *Burst sources*: Supernovae or Hypernovae explosions (last phase of the life of stars with masses $> 100 M_\odot$) which collapse in neutron stars or black holes.

In the following paraghrafs some of the aforementioned sources will be described.

1.2.1 Supernovae

The term Supernova indicates stella nova, a term invented by Galileo Galilei to indicate objects that appeared to be new stars, that had not been observed before in the sky. The name is a bit ironic, since Supernovae are actually stars at the end of their life cycle. Pratically, a Supernova explosion is a catastrophic event in which large stars disintregate completely. Vast clouds of stellar debris are ejected and rapidly heated to temperatures of millions of degrees. These expanding clouds of hot gas shine with a great variety of shapes and are referred as *remnants* of the Supernovae. Five supernovae have been seen with naked eye during the last millennium: On 1 May 1006, in the Lupus constellation, visible for 3 months during daylight e only after 3 years faded below naked-eye visibility at night; in the year 1054 in the Taurus constellation, this one was the progenitor of the Crab Nebula, in 1572 observed by Tycho Brahe in the Cassiopea constellation and one observed by Kepler in 1604; to the great of joy of modern astronomers, on 23 February 1987, a supernova appeared in the Large Magellanic Cloud (SN 1987A). Nowdays more than 5000 have been detecte. Supernovae are classified into two types. If a supernova's spectrum contains lines of hydrogen it is classified Type II; otherwise it is a Type I. In each of these two types there are subdivisions according to the presence of lines from other elements or the shape of the light curve. A supernova remnant is the structure left over after a supernova explosion: a high-density neutron star (or a black hole) lies at the center of the exploded star [10], whereas the ejecta appear as an expanding bubble of hot gas that shocks and sweeps up the interstellar medium. The emitted

GW's amplitude depends on the speed and asymmetry of the collapse. If f is the characteristic frequency (the inverse of the collapse time) and E_{GW} is the energy emitted in the form of gravitational radiation, an observer along the direction perpendicular to the collapse can measure a strain of the order [8]:

$$h \sim 2,7 \cdot 10^{-20} \left(\frac{E_{Gw}}{M_\odot c^2} \right)^2 \left(\frac{1\ kHz}{f} \right) \left(\frac{10\ kpc}{r} \right) \tag{1.42}$$

where $10\ kpc$ is the Milky Way radius. The detection technique used to characterize the short-lived signal of SN's asymmetric collaps consists in to find excess power in the data. In figure 1.3 it is possible to observe an example of GW burst signal.
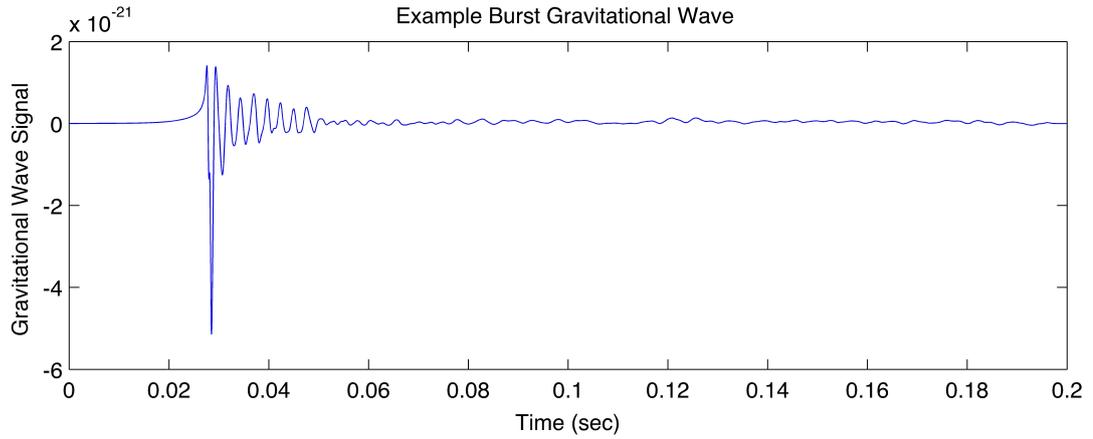
Figure 1.3: An example of GW burst signal. Imagine from https://www.ligo.org/science/GW-Burst.php.

1.2.2 Neutron Stars and Pulsars

The only object that can squeeze matter until all the electrons and protons merge into neutrons is the gravitational collapse of the core of a massive star. When a star collapses into a neutron star, its size shrinks to some $10 - 20\ km$, with a density of atomic nucleus $\approx 10^{14}\ g/cm^3$ and enormuous gravitational field close to the surface. The inner structure is described by the relationship of volume, pressure and temperature, an equation of state (EoS). These stars exists and the masses of a few have been computed in binary systems. Since angular momentum is conserved, the rotation can become very fast, with periods of the order few ms up to $1\ s$. Neutron Stars in young Supernovae remnant are typically Pulsars (short for pulsating stars), i.e., for these NSs the magnetic dipole is not aligned with the axis of rotation (the magnetic poles are in different places then the poles of rotation) and so as the star rotates, a pulse of radiation is observed every time one of the magnetic poles passes through our field of view. The first pulsar was discovered by chance in 1967, when Jocelyn Bell Burnell announced that she had discovered a regularly blinking star. If we define the three main moments of inertia as $I_1 = (1/5)M(b^2 + c^2), I_2 = (1/5)M(a^2 + c^2), I_3 = (1/5)M(a^2 + b^2)$, where a,b,c are

the three semiaxis of the rotating star with angular velocity ω, then the power emitted in GW is given by [9]:

$$\dot{E}_{GW} = \frac{32G}{5c^5}(I_1 - I_2)^2\omega^6 \tag{1.43}$$

which highlights the dipendence of the radiation on the angular velocity of the Pulsar, and that for symmetrical axis rotations ($I_1 \equiv I_2$) there isn't GW emission. The waves amplitudes depends on the moment of inertia I_3, on the star's distance from Earth, on the ellipticity in the equatorial plane $\epsilon \equiv \frac{I_1 - I_2}{I_3}$, and on the emitted frequency f (twice the rotation frequency)[9], accorting to the following relation :

$$h \sim 8 \cdot 10^{-19}\epsilon \left(\frac{I_{33}}{10^{38}K\ g\ m^2}\right)^2 \left(\frac{f}{1\ kHz}\right)^2 \left(\frac{10\ kpc}{r}\right) \tag{1.44}$$

For a Pulsar with mass $M \simeq 1.4\ M_\odot$ and radius $R \simeq 10\ km$, an irregularity on the stellar surface of the order $< 1\ mm$ and with a rotational frequency of 5 rounds per second is sufficient in order to have a detectable signal by current detectors. The signal of these sources is weak, considering that they evolve in long periods of time and generally the ellipticity is supposed to be very small ($\epsilon \approx 10^{-5}$). It should be noticed, however, that the periodicity allows integration over sufficiently long times to increase the signal-to-noise ratio of the signal. An interesting technique for finding these long strains is to try to extract the GW signals in the data generated by an *ensemble* of Pulsars observed for a long period of time.

1.2.3 Binary Systems

Chandrasekhar in 1934 demostrated that a star with mass larger than $1.44M_\odot$ (Chandrasekhar limit) cannot die into a white dwarf and will collapse; it will become a neutron star or, if its mass is larger than 3–5 times the mass of the Sun, a black hole. The first analytical solution of Einstein's equations was found in 1915, just a month after the publication of Einstein's original paper, by Karl Schwarzschild[9]. Schwarzschild's solution describes the gravitational field in the vacuum surrounding a single, spherical, non-rotating massive object. In this spacetime metric (called the Schwarzschild metric) an object with radius R and a mass M would be a black hole if $M > \frac{Rc^2}{2G}$, thus the Schwarzschild radius associated to a body of mass M is $r_S = \frac{2GM}{c^2}$. In 1963, the mathematician Roy Kerr found an exact solution to Einstein's equations for the case of a rotating non-charged black hole and two years later Ezra Newman extended it to the more general case of rotating charged black holes. In fact, according to the so-called no-hair theorem [11] a black hole can be completely described by three parameters: mass, angular momentum and electric charge. Black holes are not just exotic solutions of the GR theory. In the first chapter we have shown that they form by gravitational collapse of massive stars and there are striking evidences that they are part of several binary systems and that they are present in the center of most galaxies, including our own (the Milky Way hosts in its center a black hole of roughly 4 million solar masses, as determined from the orbit of nearby stars). Binary systems in which one object is a compact object (a pulsar, a neutron star, or a black hole) have been observed to be periodical emitters of gamma radiation. A particular class of binary systems are microquasars, binary systems

comprising a black hole, which exhibit relativistic jets (they are morphologically similar to the AGN). In quasars, the accreting object is a supermassive (millions to several billions of solar masses) BH; in microquasars, the mass of the compact object is only a few solar masses. LIGO-Virgo interferometers are sensitive enough to detect signals coming from binary systems composed by two neutron stars (BNS), two black holes (BBH), or a neutron star and a black hole (NSBH). The system loses energy due to gravitational radiation, and thus spirals closer and closer providing an enormous quantity of energy at the moment of the merger, which last only a few seconds. The objects perform a sequence of Keplerian orbits with slowly-decreasing orbital period and radius, while the emitted GW amplitude and frequency slowly increase. The Inspiral GW signal is thus called *chirp* (see the waveform in figure 1.4).
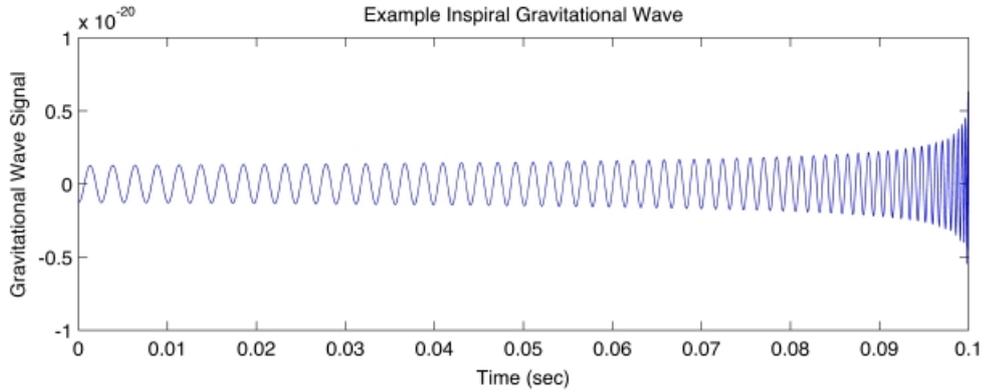
Figure 1.4: Example of the Inspiral GW (chirp signal). Imagine from: https://www.ligo.org/science/GW-Inspiral.php.

While the compact stars are well separated, the computation of the signal can be developed in the context of the linearized theory and well-modeled waveforms are obtained. When the two stars merge, the new single stellar object will find itself in an "excited" state before returning to equilibrium, during which the frequency changes from Hz to kHz. The fundamental features of the gravitational radiation emitted by a compact binary can be derived by modeling the binary as two point masses m_1, m_2 in a non-relativistic circular keplerian orbit with the angular momentum vector directed along the $\hat{z}$ axis. By calculating the quadrupole moment of the system and using it in eq. 1.34, the resulting GW polarization amplitudes are given by:

$$h_+(t) = A\frac{(1 + \cos^2 \iota)}{2}\cos(2\pi f_{gw}t_{ret} + 2\phi) \tag{1.45}$$

$$h_\times(t) = A\cos\iota\sin(2\pi f_{gw}t_{ret} + 2\phi) \tag{1.46}$$

$$A = \frac{4}{r}\left(\frac{G}{c^2}M_c\right)^{5/3}\left(\frac{\pi}{c}f_{gw}\right)^{2/3} \tag{1.47}$$

where we have introduced the *chirp mass* $M_c = \mu^{3/5}M^{2/5}$, with $\mu = m_1 \cdot m_2/M$ and $M = m_1 + m_2$ the reduced mass and the total mass of the system respectively, f_{gw} is twice the orbital frequency, ι (inclination) is the angle between the orbital angular

momentum and the line of sight of a distant observer and ϕ is a reference orbital phase. The orbital frequency ω_s is related to the orbital radius R by the third Keplero's law: $\omega_s^2 = GM/R^3$. If $f_{GW} = \omega_{GW}/2\pi$ is the GW frequency, where $\omega_{GW} = 2\omega_s$, the temporal evolution of the chirp signal can be expressed as [1]:

$$f_{gw}(t) = \frac{1}{\pi} \left(\frac{5}{256} \frac{1}{t_c - t} \right)^{3/8} \left(\frac{GM_c}{c^3} \right)^{-5/8} \tag{1.48}$$

where t_c is the coalescence time i.e. the instant at which, when the separation distance between the two stars is $r = 0$ the frequency becomes formally infinite. In terms of coalescence time measured by an observer $\tau = t_{coal} - t$, with t retarded time, the 1.48 became:

$$f_{GW}(\tau) \simeq 134 \; Hz \left(\frac{1.21 \; M_\odot}{M_c} \right)^{5/8} \left(\frac{1 \; s}{\tau} \right)^{3/8} \tag{1.49}$$

having set $M_c = 1.21 \; M_\odot$ as the chirp mass for a system of two neutron stars of equal mass $1.4 \; M_\odot$. Equivalently, one can write:

$$\tau \simeq 2.18s \left(\frac{1.21 \; M_\odot}{M_c} \right)^{5/3} \left(\frac{100 \; Hz}{f_{GW}} \right)^{8/3} \tag{1.50}$$

from which we can compute that for $10 \; Hz$ we obtain the radiation emitted at $\tau = 17$ minutes before the coalescence, for $100 \; Hz$ in the last 2 seconds, for $1 \; kHz$ in the last milliseconds. The polarization of the radiation depends on the inclination of the source: for *face-on* or *face-off* sources ($\iota = (0, \pi)$) the polarization is circular, for *edge-on* sources ($\iota = (\pi/2)$) the polarization it's linear and for intermediate inclinations it is elliptical. In chapter three we wil see that for binary BBH systems where the BH spins are misaligned with respect to the orbital angular momentum, precession effects leave characteristic modulations in the emitted gravitational waveforms.

1.2.4 Stochastic Gravitational Wave Background

Just like the Cosmic Microwave Background (CMB), which could be defined as the remaining light of the Big Bang, the Cosmic Gravitational Wave Background is an isotropic background of GW that could have been originated from the Big Bang [12]. Being composed by a random superposition of numerous emission events, they would provide indications of the evolutionary history of the early Universe, approximately between the instants $t \approx 10^{-36} - 10^{-32} \; s$ after the Big Bang,while it is known that the CMB was produced about 300 thousand years after the Big Bang, when the Universe became transparent to photons due to the electromagnetic decoupling. The strain of these GWs would be very similar to the spectrum of continuous noise at frequencies lower than $1 \; Hz$ (figure 1.5), with uniform distribution. The amplitude of the signal depends on the cosmological model and sometimes on unknown parameters. One possible way to detect them could be through the use of spaced based rather than ground based interferometers such as the Laser Interferometer Space Antenna (LISA) future NASA's project[5]. LISA will consist of three spacecraft in heliocentric Earth-trailing

---

[5]https://lisa.nasa.gov/
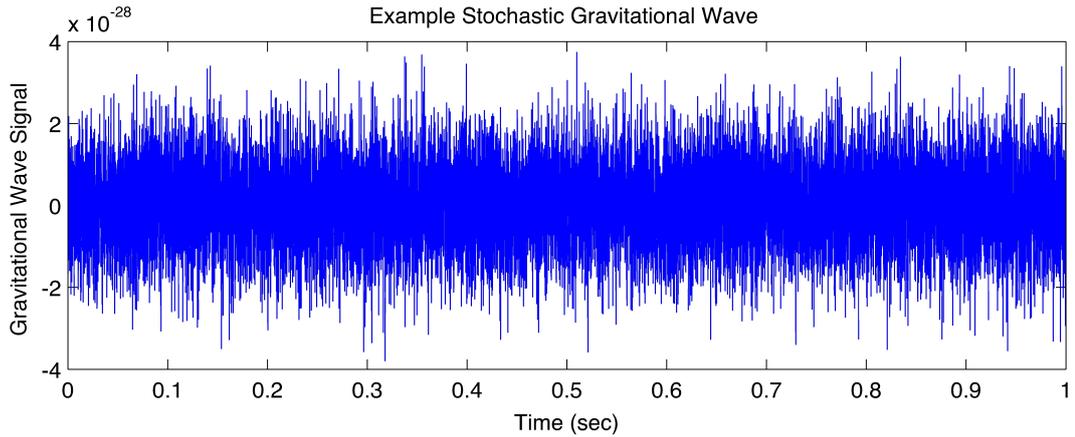
Figure 1.5: Example of GW signal from a stochastic source. Imagine from https://www.ligo.org/science/GW-Stochastic.php.

orbits, 5 million kilometres apart at the corners of an (approximately) equilateral triangle. Each of LISA's spacecraft house freely falling test masses. Unlike ground-based detectors LISA will not suffer from low frequency noise caused by seismic activity and has been designed for the detection of GW emitted by inspiral supermassive black holes up to distances of a few Gpc, the merger of supermassive black holes at cosmological distances $z \approx 3.5$ and the inspiral of binary White Dwarf stars in the nearby Universe.

1.3 Evidences of Gravitational Waves existence

In 1974 Hulse and Taylor discovered the Pulsar binary systems $PRS\ 1913 + 16$, now known as Hulse-Taylor Pulsar, and they observed that the orbital period of the binary, at a distance of about $6400\ pc$, was decreasing in agreement with the prediction of Einstein's GR theory (about $40\ s$ in 30 years). It was possible to deduce, from the time of arrival of the detected pulses, the binary orbital parameters. The masses of the two NSs were estimated to be $\approx 1.4\ M_\odot$ with period $7.75\ hours$ and the maximum and the minimum separation to be 4.8 and 1.1 solar radii respectively. The indirect evidence of GW was established after years of data taking and Hulse and Taylor were awarded with a Nobel Prize in Physics in 1993. The GWs emitted by such a system induce a GW strain of the order of 10^{-23} when they now reach the Earth, and their direct observation is out of the frequency sensitivity for the current ground-based GW detectors. The first direct evidence of GW existence was established in 2015 by the LIGO Observatory, which captured the signal emitted by the merger of a pair of black holes gravitationally bounded in a binary system (Nobel Prize in Physics 2017 awarded to Rainer Weiss, Barry C. Barish and Kip S. Thorne). The GW signal labelled as GW150914[6] was

---

[6]GW names represent the date and time when the signals are detected in Coordinated Universal Time (UTC). Previous event names only include the date, but as the detectors improve their sensitivity, it's possible to detect more than one event per day. So, recently is added the time to the names. As an example GW200208222617 was observed on the 8th February 2020 at 22:26:17 UTC time.

detected on September 14th, 2015 during the first observig run (O1, September 2015-Jenuary 2016). The shape of the GW waveform observed is shown in Figure 1.3 where three phases are well identified:

- *Inspiral*: the approach of the two BHs, in this phase frequency and amplitude increase slowly;

- *Merger*: the plunge of the BHs, frequency and amplitude increase rapidly;

- *Ringdown*: the newly formed BH is instable and the radiation emitted is the sum of contributions from different quasi-normal modes; each quasi-normal mode is an harmonic oscillation with exponential damping. After this phase no radiation is emitted.

The observed frequencies of the event are in the range $[35 - 350]$ Hz. The masses of the initial BHws were estimated to be 36^{+5}_{-4} and 29^{+4}_{-4} $M_\odot$ with the final BH having a total mass of about 62^{+4}_{-4} $M_\odot$, releasing a quantity of energy in GWs corresponding to about 3 $M_\odot c^2$. The luminosity distance of the binary system was estimated to be 410^{+160}_{-180} Mpc.
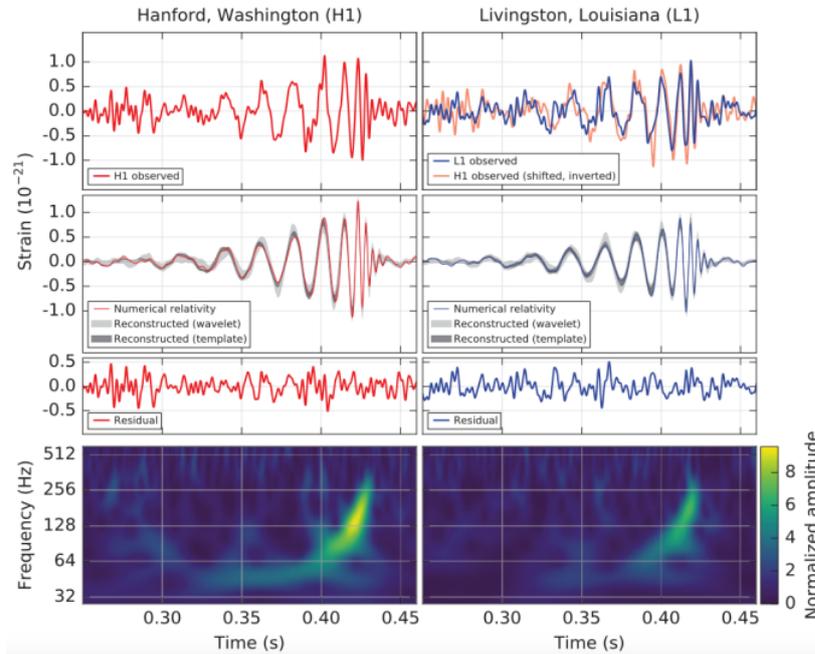
Figure 1.6: The first gravitational-wave event (GW150914) observed by LIGO: left from the Hanford (H1) site; right from the Livingston (L1) site. Credit Phys. Rev. Lett. 116, 061102 (2016).

A handful of GWs events associated to BBH mergers were detected during O1, but a special GW event, different in nature from the previous, has been detected on August 17, 2017. The italian Virgo Observatory joined LIGO during the second run (O2) and the LIGO-Virgo Collaboration detected a GW signal (GW170817) associated with the merger of two neutron stars and (1.75 ± 0.05) s later, the NASA's satellites Fermi
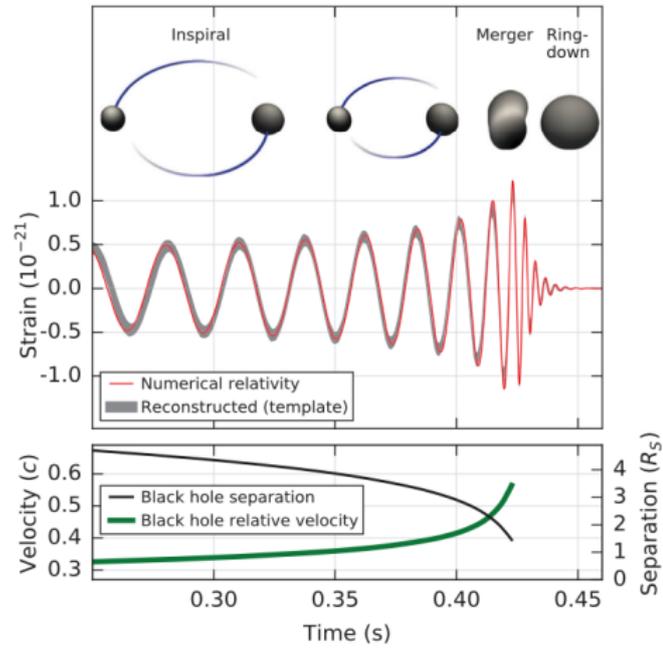
Figure 1.7: Top: The waveform of the merger of a BBH system with the parameters measured from GW150914. Estimated gravitational-wave strain amplitude from GW150914 projected onto H1. Bottom: The BH separation in units of Schwarzschild radii and the relative velocity normalized to the speed of light c. From Phys. Rev. Lett. 116, 061102 (2016).

and INTEGRAL observed independently in the same sky region a short Gamma-ray Burst (GRB 170817A). The masses of the initial NSs were estimated to be in the range $[1.36, 2.26]$ $M_\odot$ and $[0.86, 1.36]$ $M_\odot$ respectively, with the mass of the final object of about 2.82 $M_\odot$. The signal appeared much weaker in Virgo because of the lower sensitivity, however its information permitted to drastically reduce the position of the source in 28 squared degrees at 90% confidence level. These observations were followed by an extensive multimessenger campaign covering all the electromagnetic spectrum: a bright optical transient (SSS17a) was discovered in the NGC 4993 galaxy located at 40 Mpc of the Earth by the Swope Telescope in South America and shortly after the event was followed-up by ground and space observatories all around the world: X-ray and radio counterparts were discovered respectively 9 and 16 days after the merger, while no neutrino candidates were seen. The BNS event also generated a kilonova radiation, characterized by a longer optical afterglow. A total of 16000 times the mass of the Earth in heavy elements is believed to have formed, for some of them spectroscopical signatures have been observed. These observations had a far-reaching impact in nuclear and high-energy astrophysics, just quoting two aspects:

- strong evidence that the merger of BNS are progenitors of short GRBs;

- BNS mergers are one of the main sites of production of r-process nucleosynthesis elements.

The third observing run (O3) started on 1 April 2019 (divided in two data collection periods, O3a and O3b, separated by a month long break in October 2019) and concluded on April 2020 and about 90 new GWs candidate events have been reported, including the first intermediate high mass black holes (IHMBH) event GW190521, the first inequal-mass BBH event GW190412 (with marginal precession), and the first NS-BH candidate events GW190814 and GW190426. All the confirmed detections to date can be found in the third Gravitational Wave Transient Catalog (GWTC-3), which combines observations of the three observing runs (O1-O2-O3) [13].

"La filosofia (la natura) è scritta in questo grandissimo libro che perpetuamente ci sta aperto innanzi a gli occhi (io dico l'Universo), ma non si può intendere se prima non s'impara a intender la lingua e conoscer i caratteri ne' quali è scritto."
Galileo Galilei, Il Saggiatore

Chapter 2

Detection of Gravitational Waves

In the previous chapter we have shown that GW are generated by aspherical motions of matter distributions bringing information about the curvature of the space-time. In the weak-field approximation, the local metric is deformed by the addition of a dynamical tensor term $h_{\mu\nu}$ fulfilling the equation $\Box h_{\mu\nu} = 0$. This is a wave equation whose simplest solutions are transverse plane waves propagating at the speed of light. These waves changes the distance L between two masses by an amount of $\delta L = Lh$, oscillating in time. A figure of merit for a GW detector will be the space strain $h = \delta L/L$ and another one will be the horizon distance, i.e., the maximum distance to which the coalescence of two $1.4 M_\odot$ BNS could be seen. The amplitude of these signals it'si very weak ,especially if the source is too far (h is proportional to $1/R$, where R is the distance of the source), and are expected to cause changes in distances of the order 10^{-20} on Earth. The first attempt to detect gravitational waves on Earth was to detect the elastic energy induced by the compression and relaxation of a metal bar due to the variation of distances. The detectors were metal cylinders, and the energy converted into longitudinal oscillations of the bar was measured by piezoelectric transducers. The first large gravitational wave bar detector, built by Joseph Weber in the early 1960s, was a 1.2 ton aluminum cylindrical bar of 1.5 m length and 61 cm diameter working at room temperature isolated from acoustic and ground vibrations. The sensitivity of Weber's antenna was of the order of $h \approx 10^{-16}$ over timescales of $10^{-3}s$. Bar detectors (for example ALLEGRO, AURIGA, Nautilus) reached a strain sensitivies of the order $h \approx 10^{-21}$, thanks to the introduction of cryogenic techniques which allow for a substantial reduction of the thermal noise and the use of superconducting sensors. However, their frequency bandwidths remain very narrow (tens of Hz) and the resonant frequencies (1 kHz) correspond to typical acoustic wavelengths of the order of the detector length. Nowadays the most sensitive GW detectors are Michelson-type interferometers with kilometer-long arms and very stable laser beams. Resonant Fabry-Perot cavities are installed along their arms in a way that the light beams suffer multiple reflections increasing by a large factor the effective arm lengths. The lengths of the perpendicular arms of the interferometer will be differently modified by the incoming GW and the interference pattern will change accordingly. These detectors are per nature broadband, being their sensitivity limited only by the smallest time difference they are able to measure. The largest GW observatories currently operating are the Laser Interferometer Gravitational Wave Observatory (LIGO) and the italian observatory VIRGO.

LIGO is built over two sites in the USA (at Hanford, Washington, and at Livingston, Louisiana, 3000 km apart), each one with a 4 km-long arm interferometer, while Virgo is installed in the countryard of Pisa in Italy, and consists of a 3 km long-arm interferometer. Others Interferometers exists: GEO600 is a British German interferometer with 600 m-long arms located near Hannover, in Germany; KAGRA with 3 km-long arms is located underground at the Kamioka Observatory in Gifu Prefecture, in Japan. Another LIGO detector (INDIGO[1].) is planned to be built in India within 2035. A close collaboration among all of the GW observatories is in place. The networfk data together with the development of new detectors (for example interferometers in space) will allow us to explore different frequency bands and to detect GW generated by different astrophysical sources. The LISA (Laser interferometer Space Antenna) project, approved by ESA[2] will consists of three spacecrafts in heliocentric Earth-trailing orbits, 5 million km apart in the corners of an (approximately) equilateral triangle. Each of LISA's spacecraft house freely falling test masses. Unlike ground-based detectors, LISA will not suffer from low frequency noise caused by seismic activity and has been designed for the detection of GW emitted by the inspiral of supermassive black holes up to distances of about few Gpc; the merger of supermassive black holes at cosmological distances $z \simeq 3.5$ and the inspiral of binary White Dwarf in the nearby Universe. In this chapter the interferometric technique and the principal detector's noise sources will be introduced, and the response of an Interferometer to GW signals and the detector sensitivity will be described.

2.1 Characterization of a Gravitational Waves detector

The idea of using the interferometric technique to measure the space-time metric perturbations caused by a passing GW was proposed by Gertsensshtein and Pustovoit for the first time in 1963 [14]. In a simple model the beam of a laser source is divided in two by a semi-reflective mirror (*beam-splitter*) placed on the vertix of the "L" formed by the IFO's arms, which ideally reflects the 50% of the incident light and transmits the other 50%; each beam travels along the two orthogonal arms, travelling towards the highly reflective mirrors which are placed at the end of the arms; from here the beams go back and recombine in the beam-splitter. The resulting beam is finally collected by the photodiode which measures the power of the incident light. The output of the photodiode is sometimes called the asymmetric door [1] while the position of the input laser is called the symmetric door. The quantity of light collected by the asymmetric door depends on the interference between the beams when they recombine: constructive interference occurs if the optical paths differs by an integer number of the wavelength λ_0 of the laser light; destructive interference occurs if the optical paths differs by $(n + 1/2)\lambda_0$. In the second case, a null signal is detected in the asymmetric door, which corresponds to the dark fringe condition. Let L_x and L_y be the lengths of the IFO's arms in the x-y plane, the electric field resulting in the asymmetric door is given by [8]:

$$E = \frac{iE_0}{2}(e^{2ik_0 L_x} + e^{2ik_0 L_y}) \tag{2.1}$$

---

[1]www.gw-indigo.org
[2]https://lisa.nasa.gov

where $k_0 = 2\pi/\lambda_0$ is the wave number. Defining $L = (L_x + L_y)/2$ and $\Delta L = L_y - L_x$, one can rewrite the eq. 2.1 as:

$$E = \frac{iE_0}{2}e^{2ik_0L}(e^{ik_0\Delta L} + e^{-ik_0\Delta L}) = iE_0 e^{2ik_0L}\cos(k_0\Delta L) \tag{2.2}$$

thus we can write the output power in the asymmetric door as:

$$P_{out} = |E|^2 = |E_0|^2 \cos^2(\frac{2\pi\Delta L}{\lambda_0}) = \frac{P_{in}}{2}[1 + \cos\left(\frac{4\pi\Delta L}{\lambda_0}\right)] \tag{2.3}$$

Note that it depends on the difference of the path length ΔL. Defining the phase difference of the optical path as:

$$\Delta\phi = \frac{4\pi}{\lambda_0}\Delta L \tag{2.4}$$

the eq. 2.3 reads:

$$P_{out} = \frac{P_{in}}{2}[1 + \cos(\Delta\phi)] \tag{2.5}$$

The IFO translates the arms-length difference into a modulation of the output electric field. In an appropriate frequency range with mirrors suspended by mechanical pendulums and perfectly isolated, a ground-based IFO can be considered in free fall (with respect to the horizontal plane). Let be ω_0 the pendulum resonance frequency, the mirrors will behave like free-falling masses if $\omega_{GW} \gg \omega_0$, where $\omega_{GW} = 2\pi f_{GW}$ and f_{GW} is the GW's frequency. Let's consider the case of a GW h_+ that travel along the $\hat{z}$ axis, with the IFO placed in the x-y plane. The photon geodesic equation is $ds^2 = 0$. When a GW (with frequency $\omega_{GW} = L/c \ll 1$) interacts with an IFO, the eq.1.21 provide the following equations for the motion of the mirrors:

$$\begin{aligned}\Delta x &= \frac{1}{2}h_+ L_x \\ \Delta y &= -\frac{1}{2}h_+ L_y\end{aligned} \tag{2.6}$$

The minus sign for the eq. for Δy indicate that when one arm stretches, the other one shortens. If the two arms have the same length $L_x = L_y = L$, the total displacement is $\Delta L = \Delta x - \Delta y = hL$, thus:

$$\Delta\phi = \frac{4\pi}{\lambda_0}hL \tag{2.7}$$

By measuring the output power it is also possible to compute the amplitude strain h of the GW, because the phase shift is proportional to the length of the arms. We show this with the following analytical example. Let Virgo be the reference IFO with $L = 3$ km, laser wavelenght $\lambda_0 = 1 \cdot 10^{-6}$ m (infrared light), and the GW's amplitude $h \approx 10^{-21}$ (typical value for a GW signal from a SN explosion, see section 1.2.1). We obtain $\Delta L = hL \simeq 3 \cdot 10^{-18}$ m and with the eq. 2.7 we can compute the phase-shift $\Delta\phi \simeq 3,6 \cdot 10^{-11}$. Because of the weakness of these signals, it's necessary to amplify
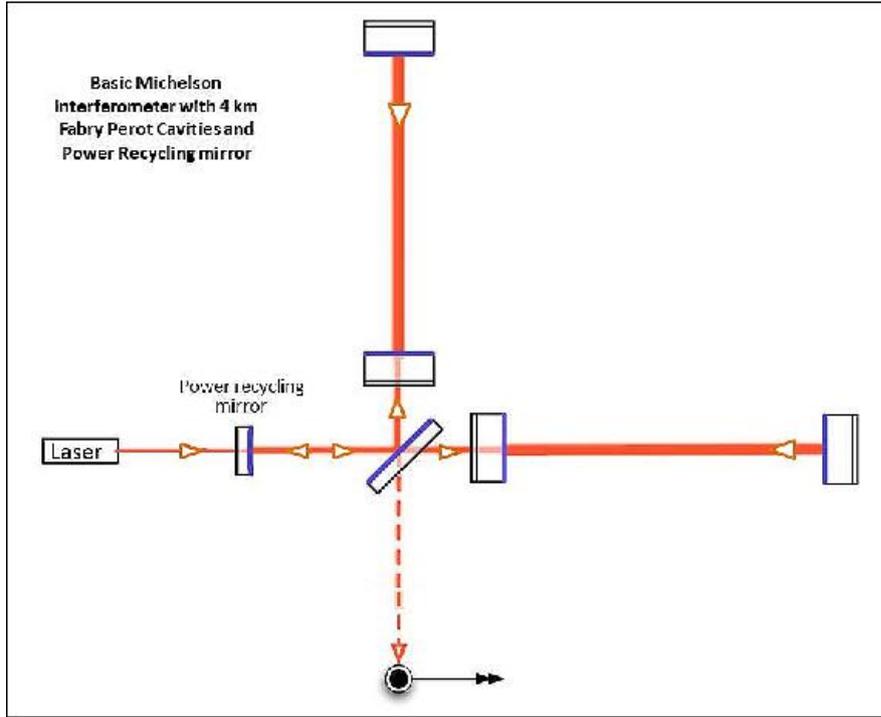
Figure 2.1: IFO scheme implemented with Fabry-Perot cavities. Imagine from: ligo.caltech.edu.

the phase difference as much as possible trying to leave unchanged the lenght of the detector's arms. A way to do it is to increase the optical path of the light by adding a Fabry-Perot cavity in each of the two arms (figure 2.1). A Fabry-Perot cavity is a resonant system composed by two semi-reflective mirrors facing each other. It works as follows: if the distance L between the two mirrors is an integer multiple of the laser wavelength λ_0, the laser field is trapped inside the cavity and travels back and forth undergoing multiple reflections. Since each interaction is in phase with the previous one (resonance condition), the resulting laser field is strongly amplified. The light remains in the cavity for a time proportional to the *Finesse* of the cavity, which is a characteristic of the cavity and describes the sharpness of the resonance [15]. The general formula for the Finesse, in the case of mirrors highly reflective, is given by:

$$F \simeq \frac{\pi \sqrt{r_I r_E}}{1 - r_I r_E} \tag{2.8}$$

where r_I and r_E are the reflection coefficients of the Input and End mirrors respectively. The Fabry-Perot cavity induces a phase variation according to the following formula [8]:

$$\Delta\phi_{FP} = \frac{2F}{\pi}\Delta\phi = \frac{8F}{\lambda_0}hL \tag{2.9}$$

this equation tell us that for each round-trip the phase shift is increased by an amount of $2F/\pi$, defined as the gain of the cavity. Now we define the time of *storage* as the

time that the photons spends in the cavity $\tau_s = 2L/c$. Considering that a wave in the cavity makes a path equal to F times the distance between the mirrors, the storage time becomes $\tau_s = L/c \cdot F/\pi$. If the IFO arms-length is intended as the length of the F-P cavity itself, then the higher the Finesse value, the greater the phase shift signal. Suppose we want to know how much the suspended masses can move when the IFO is in the resonant condition. The phase shift is $\Delta\phi = 4\pi/\lambda \cdot \Delta x$, for the next resonance condition it must be $\Delta\phi \ll 2\pi/F$, if now we use the Virgo's values for the finesse and laser wavelenght $F \simeq 450$ and $\lambda \simeq 1.064 \ \mu m$ respectively, then by the two expressions for $\Delta\phi$ we obtain that the pendulum suspended masses can move at a maximum of $\Delta x = \lambda/2F = 1.064 \ \mu m/900 \approx 1 \ nm$. Therefore the phase change of the reflected beam can be quite steep if the resonance condition is not constantly maintained. To keep the cavity in resonance, and therefore to ensure asymmetrical output in a dark fringe condition, the motion of the mirrors is controlled in real time by a "feed-back" system (or feedback circuit). An IFO can also be defined as a "null instrument", that is, a measuring instrument which in the absence of a signal records zero at the output. In fact, in the absence of a GW signal, no signal is observed at the output of the asymmetric door. This means that much of the initial laser field is reflected back through the symmetrical door. It is possible to reuse this light by placing a highly reflective mirror called *Power Recycling Mirror* (PRM), before the beam-splitter. This technique is known as "recycling light" or recirculation of light, and the purpose is to increase the effective power of the laser circulating inside the IFO. The PRM and the whole IFO built up a new cavity, called *recycling cavity*, which increases the laser power according to the Finesse of the new cavity. Virgo is a Michelson interferometer with 3 km longs arms. The mirrors that delimit them are suspended, by chains of pendulums, inside gigantic vacuum bells 2 m in diameter and 11 m high, in order to isolate them from the seismic vibrations always present on the ground and from the sound vibrations transmitted by the air. The laser light beams propagate within ultra-high vacuum tubes of 1.2 m in diameter and 3 km in length, so as not to be disturbed by the convective motions of the air. The surfaces of the mirrors are perfectly smooth, at the level of a few nanometers (billionths of a meter). The laser is ultra-stabilized in wavelength and intensity of the light beam. The Finesse of the arm cavities is about 450, which means that the effective length travelled by the beams is increased by a factor 290 with respect to the physical arm length. Advanced Virgo employs the squeezing technique: a carefully prepared state of vacuum of the optical field, a so-called squeezed vacuum, is injected into the interferometer from the output port.

2.1.1 Noise Sources

Many phenomena can mimic the effect of a GW by moving the mirrors or disturbing the laser beam. Several extreme technologies, in many different areas including optics, mechanics, electronics, and ultra-high vacuum, have been developed in order to beat the noises that can generate false signals. The sensitivity of a ground-based GW detector is mainly limited by three different sources of noises, classified as thermal, readout, and seismic:

- The thermal noise is associated with the internal dissipation phenomena of mechanical systems in thermal equilibrium with the environment, which in turn is

connected to the thermal motion of the microscopic elements that make up the mechanical system itself (Brownian motion of the test masses due to the impact of the surrounding air molecules). It's dominant at intermediate frequencies (10-500 Hz). The main contribution comes essentially from the thermal oscillations of the suspensions (pendulum modes, vertical modes, violin modes) and thermal oscillations of the mirrors (normal modes). To minimize such effects the test masses are placed in very high vacuum environments and the frequencies of the intrinsic resonances of the system are set as far as possible from the target signal frequency band;

- The intrinsic readout noise is due to the fluctuations induced by the quantum nature of the interactios between the laser light beam and the mirrors, and it's dominant at high frequencies (> 500 Hz). The light beam may be modeled as a discrete set of photons obeying in their arrival time to the mirror to Poisson statistics. The number of photons measured has a statistical intrinsic fluctuation called "shot noise", which decreases with the increasing of the laser power. On the other hand, the increase of the laser power can increases the momentum transfer to the mirrors ("radiation pressure"), which will change the phase of the beams. In fact, the mirrors are subject to a force due to radiation pressure that can be expressed as $F = 2n \cdot \hbar\omega_0/c$, where n is the number of photons hitting the mirror per unit of time. Each fluctuation of the photon flux causes a variation of the phase difference given by [8]:

$$\Delta\tilde{\phi} = \frac{4\pi}{\lambda} \frac{\sqrt{8P_0\hbar\omega_0}}{M\omega^2 c} \tag{2.10}$$

where M is the mass of the mirror, P_0 is the imput laser power. The sum in quadrature of the radiation pressure force and the eq. 2.10 gives the total contribution of the shot-noise on the phase-shift at the output of the IFO:

$$\Delta\tilde{\phi}_n = \sqrt{\frac{2\hbar\omega_0}{\eta P_0} + \left(\frac{4\pi}{\lambda}\right)^2 \frac{8P_0\hbar\omega_0}{(M\omega^2 c)^2}} \tag{2.11}$$

where η is the quantum efficiency of the photodiode. It can be shown that there is an optimal power for which $\Delta\tilde{\phi}_n$ has a minimum, and it is given by:

$$\Delta\tilde{\phi}_{QL} = \frac{4\pi}{\lambda} \frac{1}{\eta^{1/4}} \sqrt{\frac{4\hbar}{M\omega^2}} \tag{2.12}$$

The eq. 2.12 represents the quantum limit for the computation of the phase shift in the signal. To minimize such effect, the tests masses should be as heavy as possible and the Heisenberg uncertainties relations (the quantum limit) carefully handled. One way to overcome this limit would be to make the two noises related to each other. Devices designed to achieve this goal are called *Quantum non-demolition*, which are used to inject Squeezed light states (that is non-classic light states) into the detector. For more details see the reference [16];

- The seismic noise dominate at low frequencies (<10 Hz) and accounts for all the natural or human-made perturbations comprising a large range of phenomena like earthquakes, environment perturbations or nearby motor vehicles traffic.

The measured spectrum of such noise, in a quiet location, decreases with the frequency. These vibrations can produce a displacement of the mirrors of the order $\delta\tilde{x} \sim 10~\mu m$ that can mimic a GW signal. To minimize such effects the test masses are isolated from the ground through several attenuation stages (pendulums systems) characterized by resonance frequencies much lower than the expected signal frequencies. For frequencies much greater than the resonance frequency $\omega \gg \omega_0$, if we describe the motion of the mirrors in terms of the movement of the suspension point as a function of the movement of the oscillating mass $\frac{\delta\tilde{x}}{\tilde{x}} = -\frac{\omega_0^2}{\omega^2}$, then the seismic vibrations are attenuated by a factor of ω_0^2/ω^2 with a single pendulum and by a factor of $(\omega_0^2/\omega^2)^n$ with n pendulums in cascade. To access lower frequencies (1–10 Hz), the possibility to build large interferometers underground in a low seismic region are being studied (For istance the Einstein Telescope[3]).

Among several improvements the Phase I of Advanced Virgo Plus foresees the installation of a Signal Recycling mirror to implement a technique that will increase the sensitivity in the mid-high frequency range; the suspended SR mirrors will replace the SR lens. The squeezing technique will also be improved by the addition of a 300 m long Fabry-Perot Filter cavity that the squeezed vacuum state will travel through before being injected into the interferometer: this will allow to improve the sensitivity not only at high frequency by beating the quantum photon counting noise but also at low frequencies by overcoming the quantum noise coming from the pressure exerted on the mirrors by the impinging laser radiation. In section 2.1.3 the sensitivity plot of Advanced Virgo counting for all the noises sources is shown.

2.1.2 Detector response to Gravitational Waves

We want to write down the GW signature of a binary system measured under the approximation of the Newtonian quadrupole-moment which neglects spins. A convenient choise for the Cartesian coordinates is to direct the $\hat{\mathbf{x}}$ and $\hat{\mathbf{y}}$ axes along the IFO's arms and the $\hat{\mathbf{z}}$ axis along the vertical direction as shown in figure 2.2. Let be $\hat{\mathbf{N}}$ the unit vector pointing towards the GW source and (θ, ϕ) the spherical polar coordinates of $\hat{\mathbf{N}}$ with respect to the Cartesian coordinates [2]. The orbital angular momentum is given by $\mathbf{L} = \mu\sqrt{Mr}\hat{\mathbf{L}}$, where $M = m_1 + m_2$ is the binary total mass, μ the reduced mass, r the orbital distance between the two stellar objects. The binary's circular orbit if projected onto the plane of the sky at the detector's location (i.e. orthogonal to the wave's propagation direction) looks elliptical. The principal axis of this ellipse which points towards $\pm\hat{\mathbf{N}} \times \hat{\mathbf{L}}$ will be called the principal " + " direction and an axis rotated counterclokwise from it by $\pi/4$ will be called the the principal " × " direction. Any plane-fronted GW traveling in the $-\hat{\mathbf{N}}$ direction can be written as a linear combination of $h_+(t)$ and $h_\times(t)$. Then, the gravitational fields are given by:

$$h_+(t) = -\frac{2\mu M}{rD}\left[1 + (\mathbf{L} \cdot \hat{\mathbf{N}})^2\right]\cos 2\phi(t) \tag{2.13}$$

$$h_\times(t) = -\frac{2\mu M}{rD}\left[-2\hat{\mathbf{L}} \cdot \hat{\mathbf{N}}\right]\sin 2\phi(t)$$

---

[3]https://www.einstein-telescope.it

D is the distance from the source and $\phi(t)$ is the angle in the orbital plane from the principal directions to the diameter r. The strain $h(t)$ produced by a GW in the IFO will be a linear combination of $h_+(t)$ and $h_\times(t)$ but also of the antenna pattern functions F_+ and $F_\times$, which depend on the source direction (θ, ϕ) and on the polarization angle ψ [17]:

$$F_+ = -\frac{1}{2}(1 + \cos^2\theta)\cos 2\phi \cos 2\psi - \cos\theta \sin 2\phi \sin 2\psi$$
$$F_\times = \frac{1}{2}(1 + \cos^2\theta)\cos 2\phi \sin 2\psi - \cos\theta \sin 2\phi \cos 2\psi$$
(2.14)

The polarization angle ψ is given by (up to an arbitrary multiple of π):

$$\psi = \arctan\left(\frac{\mathbf{L}\cdot\hat{\mathbf{z}} - (\mathbf{L}\cdot\hat{\mathbf{N}})(\hat{\mathbf{z}}\cdot\hat{\mathbf{N}})}{\hat{\mathbf{N}}\cdot(\mathbf{L}\times\hat{\mathbf{z}})}\right)$$
(2.15)

Thus, the GW strain at the output of a detector can be expressed as [18]:

$$h(t) = h_+(t)F_+(\theta, \phi, \psi) + h_\times(t)F_\times(\theta, \phi, \psi)$$
(2.16)

The detector response is greatest when the GW propagates along the $\hat{z}$ axis and it's null on the bisectors of the x -y quadrants. Note that, for $\theta = 0$ and $\psi = \pi/4$, the effect in the two arms of the IFO is the same, and no phase shift is produced. The raw data from a GW detector comes from the time-varying intensity of the laser light measured at the interferometer output, that's why they need to be calibrated to obtain the corresponding strain amplitude. We will see that for quantify the precession modulation effects on a
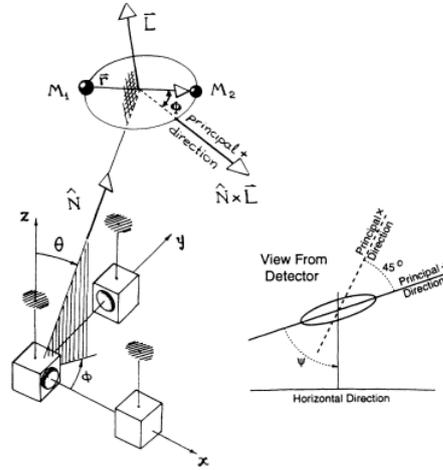
Figure 2.2: A Cartesian coordinate system $(\hat{\mathbf{x}}, \hat{\mathbf{y}}, \hat{\mathbf{z}})$ attached to a GW detector, and the geometry of a coalescing binary relative to these coordinates. Figure from [2].

GW signal, it's convenient to divide the GW in an amplitude modulation and a phase modulation, for this reason we shall rewrite the strain in the convetional amplitude-phase form:

$$h(t) = -A(t)\cos[2\phi(t) + \varphi]$$
(2.17)

where $A(t)$ and φ are given by:

$$A(t) = \frac{2\mu M}{rD} \left([1 + (\hat{\mathbf{L}} \cdot \hat{\mathbf{N}})]^2 F_+^2(\theta, \phi, \psi) + 4[\hat{\mathbf{L}} \cdot \hat{\mathbf{N}}]^2 F_\times^2(\theta, \phi, \psi) \right)^{1/2} \qquad (2.18)$$

$$\varphi = \tan^{-1} \left(\frac{2\hat{\mathbf{L}} \cdot \hat{\mathbf{N}} F_\times(\theta, \phi, \psi)}{[1 + (\hat{\mathbf{L}} \cdot \hat{\mathbf{N}})]^2 F_+(\theta, \phi, \psi)} \right)$$

We will refer to φ as the signal's polarization phase. When precession of the spins is ignored, all the parameters in the previous formulas are constant in time except the orbital distance and the orbital phase. The orbital diameter can be computed integrating the inspiral rate $dr/dt = (dE/dt)(dE/dr)$, where the Newtonian expression for the energy $E = -1/2\mu M/r$ can be used, and the energy loss is given by the quadrupole formula $dE/dt = -32/5\mu^2 M^3/r^5$. The orbital diameter $r(t)$ is given by the equation:

$$r(t) = \left(\frac{256}{5} \mu M^2 \right)^{1/4} (t_c - t)^{1/4} \qquad (2.19)$$

with t_c the collision time at which formally $r \to 0$. In absence of precession the variation in time of the orbital phase $\dot{\phi}$ is simply the angular velocity Ω of the two stars in the orbital plane. However, this is no longer valid in presence of precession, because $\hat{L}$ vary in time. To deal with this, the *carrier phase* of the waveform is defined $\phi_C(t) \simeq \int \Omega(t) dt$. It's convenient to specify the constant of integration in carrier phase equation so that $\phi_C(t_c) \simeq \phi(t_c)$ whether the orbit is precessing or not. Computing the integral using $\Omega = M^{1/2}/r^{3/2}$ using the equation 2.19, at the lowest order in M/r, we find:

$$\phi_C(t) = \phi(t_c) - \left[\frac{1}{5} (\mu^{3/5} M^{2/5})^{-1} (t_c - 1) \right]^{5/8} \qquad (2.20)$$

We will compute in section 3.2.1 the precessional correction needed when the precession of the orbital plane is not neglected.

2.1.3 Detector Sensitivity

Over the years the sensitivity of LIGO and Virgo has improved due to a combination of detector upgrades, improved data quality and data analysis techniques. During O3 many upgrades and repairs were completed, including mirror cleaning at LIGO Livingston, replacing vacuum equipment at LIGO Hanford, and increasing the laser power in Virgo. Continuous maintenance throughout the observing runs allows the detectors to maintain or increase their sensitivity. There are several ways to estimate the sensitivity of a GW detector, one is in terms of the BNS range, that is the distance at which the merger of a BNS system gives a signal-to-noise ratio (SNR) equal to 8; the distance is averaged over all the possible sky localizations and binary orientations. The wider the range, the farther you look and greater is the probability to capture signals. Figure 2.3 shows the median BNS range for each detector between O3a and O3b, the range is increased by 13.3% for Virgo, 6.5% for LIGO Hanford, and stayed around the same for LIGO Livingston (the most sensitive detector) with a slight decrease in sensitivity of 1.5%.
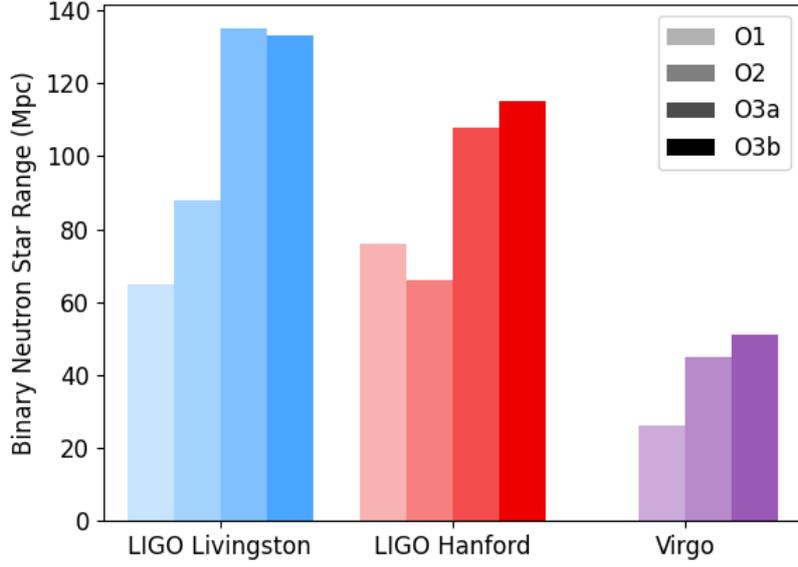
Figure 2.3: The median binary neutron star ranges for each detector during the first (O1) and second observing runs (O2), the first part of observing run 3 (O3a), and the second part of observing run 3 (O3b). The ranges are shown in units of megaparsecs. Credits: LIGO-Virgo-KAGRA Collaborations/Hannah Middleton/OzGrav.

Another way to define the sensitivity of a GW detector is to express it as function of the GW frequency in terms of the amplitude spectral density of the interferometer output noise, expressed in units of GW strain $|h|/\sqrt{Hz}$. Thus, the lower the curve (and hence the lower the noise), the more sensitive the detector in that frequency range. Suppose we want to measure the signal h(t), and that the contribution of noises can be expressed as an additive function n(t). The total signal can be written as the sum of contributions $s(t) = h(t) + n(t)$. The power Spectral density is defined as:

$$S_h(\omega) = \lim_{T \to \infty} \frac{1}{T} \int_{-T/2}^{T/2} p(t)e^{-i\omega t}dt \tag{2.21}$$

that is, it's the Fourier transform of the autocorrelation function p(t) of the total signal:

$$p(t) = \frac{1}{T} \int_{-T/2}^{T/2} s(t)s(t-\tau)d\tau \tag{2.22}$$

where T is the observation time. The linear power spectral density is given by the square root of the equation 2.21, $S_h^l(\omega) = \sqrt{|S_h(\omega)|}$. Advanced Virgo is sensitive in the frequency interval from a few Hertz to several thousands of Hertz (kHz). The plot in figure 2.4 shows the projected sensitivity for the fifth observation run, O5, foreseen to start in the year 2026. The final expected sensitivity (black curve) results from the sum of all the noises contribution expected to be the most relevant during O5.
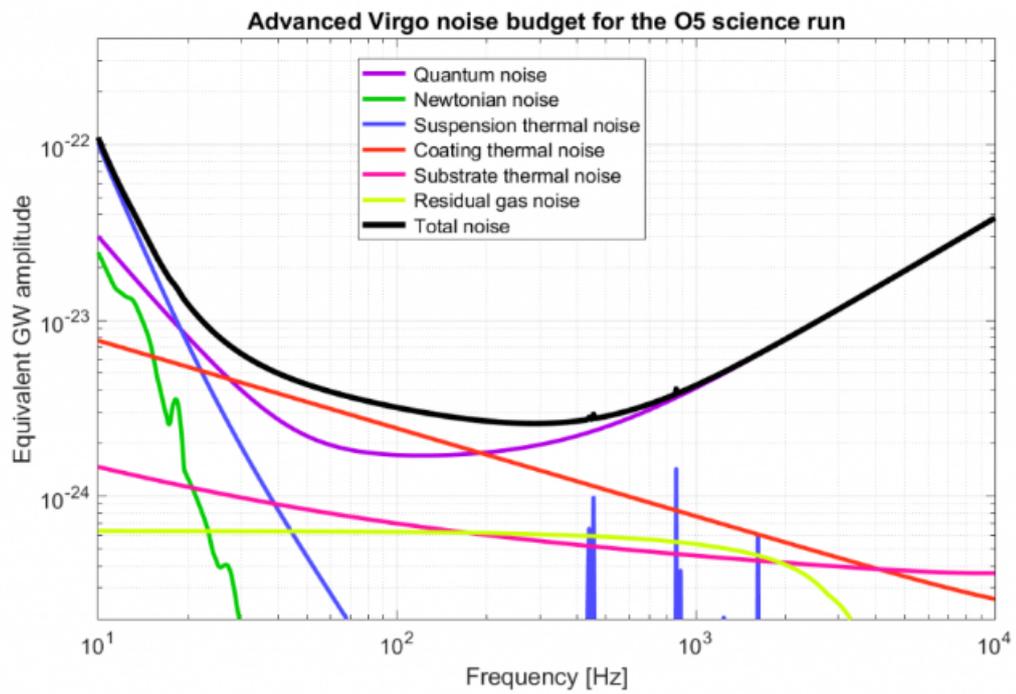
Figure 2.4: The projected sensitivity of Advanced Virgo for the future O5 science run. The black curve rapresent the final expected sensitivity with the contribution of all noises. Reference https://www.virgo-gw.eu/it/science/detector/sensitivity/.

"E qual sfavilla
nei notturni sereni in fra le stelle.
Espero il più leggiadro astro del cielo;
tale l'acute cuspide lampeggia
nella destra d'Achille
che l'estremo danno in cor volge
dell'illustre Ettorre."
Omero, Iliade

Chapter 3

Binary Black Holes systems

Measurement of spin-precession in GW signals from BBH is a blossoming field in GW astronomy, as it relates to both general relativistic dynamics in strong field regime and astrophysical binary formation scenarios. The signal GW190412 was recorded during LIGO's and Virgo's O3a observing run with a network signal-to-noise ratio (SNR) of 19. It is different from others observations due to its asymmetric masses: a $30\ M_\odot$ BH merged with a $8\ M_\odot$ BH companion, with a final renmant BH of $37\ M_\odot$. In addition, it shows marginal precession (with parameters values consistent with the ones expected for precessing sources) and strong evidence for gravitational radiation beyond the leading quadrupolar order. The signal GW200129 was recorded during O3b with single mass values $m_1 = 39\ M_\odot$, $m_2 = 22\ M_\odot$ and total mass of $M_{tot} = 61\ M_\odot$, and the binary's orbit precesses at a rate ten orders of magnitude faster than previous weak-field measurements from binary pulsars. According to current binary population estimates a GW200129-like signal is extremely unlikely, and therefore presents a direct challenge to many current binary formation models. Until recently it was believed that BHs in nature appear in two broad mass ranges: stellar mass BH with ($M \approx 3 - 50\ M_\odot$), produced by the core collapse of massive stars (commonly classified as first generation BHs), and supermassive BH ($M \approx 10^5 - 10^{15} M_\odot$), which are found in the centers of galaxies and are produced by a still uncertain combination of processes. However, there are evidences for an Intermediate-Mass BH class (IMBH) with masses in the range $M \approx 10^2 - 10^4\ M_\odot$, classified as second (or higher) generation black holes, representing the remnant of others BBH mergers. Such a sub-population of hierarchically assembled BHs presents distinctive GW signatures: high masses within the so called Pair-Instability mass gap (sometimes also referred to as "upper mass gap", in contrast with the "lower mass gap" between BHs and NSs) and dimensionless spins clustered at the characteristic value of 0.7. Then, repeated mergers are expected to cluster in the high mass - high spin region of the parameter space, especially if different generations of mergers are combined. It is expect that a mixed binary, composed by a first generation BH and a second generation BH, will present a mass ratio more unequal compared to other events where both components come from the same generation. For these reasons, IMBH mergers are promising candidates for GW observation of spin-induced orbital precession [19]. To date there is a single IMBH hierarchical-merger candidate, represented by the GW signal GW190521 recorded during O3b [20], with the primary and secondary BHs masses falling in the mass gap predicted by PI theory: $85^{+21}_{14}\ M_\odot$

and $66^{+17}_{-18}\ M_\odot$, with the highest final mass ever recorded of about $\approx 142^{+28}_{-16}\ M_\odot$. This signal was characterized by a very short duration (approximately $0.1\ s$) and bandwidth (around 4 cycles in the frequency band $(30-80\ Hz)$)with a three-detector SNR of 14.7 and a peak luminosity close to the merger of about $E_{peak} = 3.7^{+0.7}_{-0.9} \cdot 10^{56}\ erg\ s^{-1}$. The signal also shows mild evidence of precession due to non-zero in-plane spins components and evidences for higher-order multipoles beyond the dominant $(2, \pm 2)$ mode. A brief review of the current formation channels proposed for IMBH class as well as the basic theory of spin-precession motion will be addressed in this chapter. Furthermore, for the study of the precession motion, two cases of interest will be analized: the case when the two bodies have nearly equal masses and the case when one of the bodies has negligible spin. For both the dynamic of the system is characterized by the *simple precession* motion, which occurs when the direction of the binary's total angular momentum $\hat{J}$ is constant in time and the orbital plane precesses around this direction. The approximate, analytical solutions for the simple precession motion will be derived.

3.1   X-Ray Binaries

Stars form by gravitational instabilities of interstellar masses and gases. For given conditions of density and temperature, gas clouds (mostly hydrogen and helium) collapse and if their mass is suitable eventually start termonuclear reactions. Stellar masses are limitated by the conditions that i) nuclear reaction can switch-on in the stellar core and ii) the radion drag of the produced luminosity on the plasma does not disrupt the star's structure. The heavier the star, the stronger its gravitational energy, and the more effective are the nuclear processes powering it. Average stars like the Sun spend the most of their lifetime in the so called *main sequence* of the Hertzsprung-Russell diagram[1] burning hydrogen into helium through proton-proton nuclear reactions. At the end of the principal fuel, the star will have a massive core of helium and new fusion reactions may start, converting it into carbon. Further reactions coverting carbon in heavier elements will continue until the thermonuclear process become inefficient (the most abundant elements heavier than carbon created by the stellar fusion processes are nitrogen, oxygen and iron, the latter being the most stable atom). The fate of a star depends on it's mass:

- Progenitor stars with masses $M < 0.1\ M_\odot$ are left with an inert core at the end of nuclear fuel combustion and the stellar object will became Brown Dwarf with $M < 0.08\ M_\odot$;

- Stars with masses $M \leq 8\ M_\odot$ will give White Dwarf, while stars with $M > 10\ M_\odot$ could produce neutron stars or black holes;

- Stars with masses $M \leq 20 M_\odot$ results in either an oxygen-neon- magnesium core or iron core. The object undergoes electron capture converting mostly proton-electron pairs into neutrons and collapsing violently on a time scale of seconds. The outer infalling material is thought to bounce on the newly formed neutron

---

[1]Usually abbreviated to H-R diagram, is a theoretical tool that relates the effective temperature and luminosity of stars.

core, producing a supernova explosion which includes a burst of neutrinos from the neutronization process. The resulting collapsed core is a degenerate and compact sphere of neutrons with density comparable to atomic nuclei. Asymmetries in the supernova explosion can lead to an extremely fast spinning neutron star or Pulsar;

- Stars with masses above $20 M_\odot$ have an extremely strong gravitational field and the collapse can't be contrasted: they will produce black holes.

The existence of the bright cosmic X-ray sources discovered in the 1960s represented an exciting and challenging astrophysical problem. No physical process known was able to produce the enormous X-ray luminosity observed. The optical identifications of the sources Sco X-1 and Cyg X-2 stimulated theorists and observers to learn more about these new X-ray stars. The general deal about the nature of these exotic objects was to consider them candidates for either white dwarfs, neutron stars or black holes, because these sources were only theoretical concepts. It was the discovery by Uhuru satellite (launched in december 1971) of the eclipsing X-ray source Cen X-3 which revealed the existence of a binary system in which the X-ray energy source was a rapidly spinning NS exchanging mass in a binary system. There are two scenarios widely accepted for compact objects in which the mass can be transferred from a star onto its orbiting compact object:

- High-mass X-ray binaries (HMXBs): the material transferred onto the compact object is provided by a powerful stellar wind from an early-type massive star (OB type stars), creating a comet-shaped shock front (see figure 3.1). The accretion disc is small and fluctuations in wind density are converted in X-ray flux. For instance, the X-ray binary systems Cen X-3 and Cyg X-1 belongs to this class;

- Low-mass X-ray binaries (LMXBs): the mass-losing star is a low mass object, it will not have a strong stellar wind and hence cannot power the X-ray source by the same mechanism as in HMXBs. In LMXBs a low-mass star transfer it's mass to a companion because it fills its Roche lobe (surface of equal gravity) and the mass flows through the inner Lagrangian point, L_1 (see figure 3.1). The Matter flowing out of the star forms a stream that impacts the accretion disc (creating a bulge or thickened region) and, by viscous forces, is gradually accreted onto the compact object where the X-rays are generated. This mass transfer is only stable if the donor star is less massive than the acceptor companion. X-ray binaries of this type are for example Sco X-1 and Her X-1.

Uhuru satellite discoveried several eclipsing X-ray binaries, and from it's data was possible to observe that HMXBs and LMXBs systems have a non-homogeneous distributions in the sky. The mass donors in HMXBs have a very short lifetime, and they are found close to their formation site, generally in the spiral arms of the Milky way. The much longer lived LMXBs are associated with older stellar populations distributed in the central regions of the Galaxy.
All the discussion of interacting binaries so far has been in terms of a compact object which is accreting matter from its companion, the basic model of the binary is almost independent of what type of compact object it contains. However, the accretion rates vary depending on the compact objects involved.
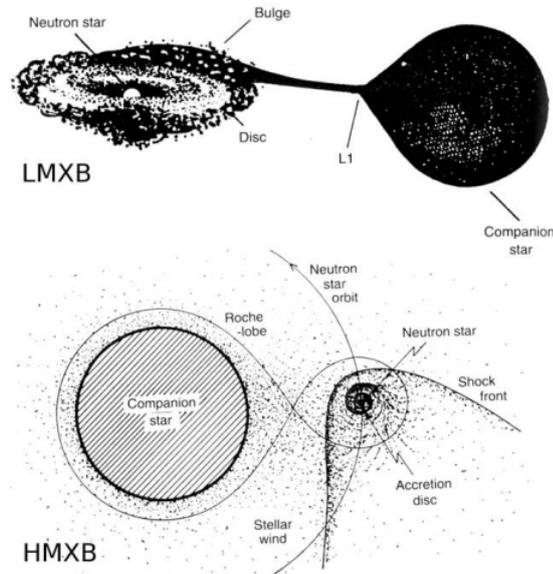
Figure 3.1: Artist's conception of the two principal mechanisms by which matter is transferred onto a compact object in a X-ray binary system. On top a LMXB system and on bottom a HMXB system are rapresented. Figure from the book "Exploring the X-ray Universe", Seward FD and Charles PA.

3.1.1 Evolutionary Scenarios

The evolutionary scenarios of binary systems, from a pair of main-sequence stars to a relativistic binary consisting of NSs or BHs, is fully confirmed by more than 30 years of astronomical observations and is now considered standard [21]. Initially the two stellar objects are orbiting each other in their Roche lobes. As the more massive star evolves away from the main sequence, it will expand until overflowing its Roche lobe. The material outside of the lobe will fall onto the companion and this can lead to a stable mass-transfer or to a common-envelope between the stars. During this phase the star accreting mass from the companion achieve a large angular momentum, and the donor, if massive enough, eventually undergo core collapse to form a BH, and the system as a whole would become an High Mass X-ray binary. As the secondary body expands and evolves it would eventually fill its own Roche lobe and the binary would then go through a common-envelope phase. The common-envelope phase is highly dissipative and would probably lead to both contraction and circularization of the binary's orbit, in addition the accretion-mass process can allow the BH to spin-up. The secondary body would undergo supernova explosion and form a stellar mass BH (or a NS) leaving a pair or BHs (or NS-BH). Before the supernova explosion of the secondary body, it is expect that the spin of the BH is aligned with the binary's orbital angular momentum. However, the kick associated with the supernova explosion can cause the orbital angular momentum to became tilted with respect to the total angular momentum. Thus, it is expected that the BH's spin can be misaligned with respect to the post-supernova orbital angular momentum. At some point the inspiral must terminate: the two objects fall towards each other with a plunge and then merge. The remaining object will be

a BH. When NSs are involved the physics of the merger is greatly complicated: tidal forces before the plunge may in fact distrupt one or both NSs, dispersing neutron-rich matter onto the circumstellar environment. Tidal disruption can held the production of electromagnetic emission from the system at different wavelengths, possibly an accretion disk around the remaining compact object and a jet orthogonal to the disk due to relativistic beaming (Gamma-Ray Bursts emission). Neutron-rich matter released during NS disruption may undergo rapid neutron-capture process (r-process) resulting in the production of heavy elements which will produce an infrared emission (kilonova emission), as observed for the event GW170817.

In the case of LMXB, an evolved late type star fill its Roche lobe and transfer material through its inner Lagrangian point to the giant companion. Because of the angular momentum conservation law, the material of the donor can't fall directly onto the acceptor companion, but orbits around it forming an accretion disc. The major difference between this model and the one for HMXBs is the mechanism of the mass-transfer.

The coalescence rate density, i.e. the number of coalescence events per unit of time and volume, can be computed via population synthesis codes, which evolve large numbers of simulated binaries assuming particular distributions of initial parameters. Current uncertainties in modeling common envelopes and supernova kicks imply a large uncertainty of the theoretical estimates [13]. However, from the population properties of the GWs detections through GWTC-3 it was possible to infer for NS-BH systems a merger rate of $7.8 \ Gpc^{-3}yr^{-1} - 140 \ Gpc^{-3}yr^{-1}$, and for BBH systems a merger rate of $17.9 \ Gpc^{-3}yr^{-1} - 44 \ Gpc^{-3}yr^{-1}$ at a fiducial redshift of z=0.2.

3.1.2 Mass-Spin Constrains

Determining stellar masses in binaries by measuring their relative velocities and the size of the orbit, has been the fundamental method used by astronomers for almost 100 years. The velocity of each object can be determined with the Doppler effect, one in the optical and the other one in X-rays. If they are eclipsing, the inclination of the system is known to an high degree of accuracy, and therefore It's possible to solve the mass function $f(M)$ of the system defined as:

$$f(M) = \frac{P_{orb}K^3}{2\pi G} = \frac{m_1 sin^3 \iota}{(1 + m_2/m_1)^2} \tag{3.1}$$

where P_{orb} is the orbital period of the binary, K is the velocity amplitude of the rotating object and ι is the inclination angle. By measuring the K velocity is possible to compute the mass ratio of the two stars. The most direct measurement comes from optical spectroscopy, which gives the orbital radial velocity curve of either the secondary (mass losing) star or, if it's present, the accretion disc around the compact object. For a BH-NS system it's possible to measure the velocity amplitude of the mass donor K_2, and the mass function became:

$$f(M) = \frac{PK_2^3}{2\pi G} = \frac{m_x^3 sin^3 \iota}{(m_x + m_2)^2} \tag{3.2}$$

which depends only on the directly observable quantities P and K_2. To compute m_x it's necessary to know m_2 and ι accurately. Recent measurements consistently indicate that

BHs masses span in the range $5M_\odot \leq M_{BH} \leq 5\times10^8 M_\odot$. From GWs signals collected by LIGO-Virgo the BHs masses distribution in binaries has been localized with peaks emerging at chirp masses of $8.3^{+0.3}_{-0.5}M_\odot$ and $27.9^{+1.9}_{-1.8}M_\odot$. A BH can be completely described by three parameters, the mass, spin angular momentum J and charge ("No hair" theorem). The maximum value possible for the spin is given by $J_{max} = GM^2/c$. It is customary to use a dimensionless spin parameter $\chi = cS/Gm^2$ with values in the range $[-1,\ 1]$: negative values implies a counter-rotating BH; zero corresponds to a non-spinning BH which is referred to as a Schwarzschild BH; 1 corresponds to a maximally spinning BH and is known as a Kerr BH. A Schwarzschild (non-spinning) BH has $R_{ISCO} = 3\ R_S$, where R_S is the radius of the event horizon. For a Kerr BH is $R_{ISCO} = 0.5\ R_S$, which means that the accretion disc can extend much closer to the event horizon. The angular momentum J can be estimated by measuring the temperature of the accreting material, which depends on R_{ISCO}. Observations of HMXB indicate that BH spins can be nearly maximal, values range from < 0.25 for the system LMC X-3 to ≈ 1 for the system $1915 + 10$. BHs in binaries may develop high spins because of the mass-transfer process [22][23]. Alternatively, BHs born from the merger of two smaller BHs are expected to have high natal spins[24]. In O3 data collected by LIGO-Virgo there are evidences of negative aligned-spins, an increase of spin magnitude for systems with large unequal mass ratio, and evidences of misalignment of the spins [25]. The mass-spin properties of BBHs inferred from their GW signatures reveal important clues about how these binaries form. BHs that evolved together from the same binary system will have spins that are preferentially aligned with the orbital angular momentum, otherwise if the BHs formed separately from each other and became gravitationally bound there is no preference for aligned-spins configuration [26]. The fidelity with which GW detectors can measure off-axis spins, and therefore to observe precession, will have important implications for the use of GW to study BBH formation channels[27][28].

The computation of NS masses is difficult due to the unknown equation of state (EOS) of neutron matter. However, maintaining hydrostatic equilibrium requires an upper limit on the mass (maximum stiffness) to be $\approx 3M_\odot$. From LIGO-Virgo data a broad and relatively flat NS's mass distribution extending in the range $1.2-2M_\odot$ has been observed, with a narrow cluster at $1.35M_\odot$. The spin of a NS can be characterized by the dimensionless vector $\chi = cS/Gm^2$ with m the NS's mass, and it is limited by the break-up velocity to be $\chi \leq 0.7$. Known NSs are far from this limit, with the fastest-spinning one with $\chi \approx 0.4$ [29]. In the following discussions the upper limit $|S_i| \leq m_i^2$ for all bodies will be applied.

3.1.3 IMBH and merger rates

Intermediate-mass black holes (IMBH), classified as the BHs with masses in the range $10^2-10^5\ M_\odot$, bridge the gap between stellar BHs and supermassive BHs (SMBH) [30]. IMBH are predicted to form or via direct collaps of highly massive stars ($\geq 230\ M_\odot$), commonly referred as population III stars, or via hierarchical mergers of smaller BHs, in poor metal star clusters or in active galactic nuclei (AGN) [31], [32]. More exotic possible scenario like primordial BBH (multiple) mergers are also proposed [33]. Several ultra-luminous X-ray sources, defined as those with a total isotropic luminosity

of $\geq 10^{39}\ erg\ s^{-1}$, have been studied as IMBH candidates but only a few support evidences consistent with the predictions. Some IMBH candidates lies in the center of dwarf galaxies and are associated with low-luminosity AGN. The only strong candidate IMBH event in the LIGO-Virgo collected data is the signal GW190521, with the mass of the primary component in the range where Pair Instability supernova theory (PI) is expected to suppress BH formation[34], [35]. PI develops when a star have an helium core mass of about $\geq 32\ M_\odot$, and the effective production of electron-positron pairs in the stellar core constrast the radiation pressure [36]. This leads to a contraction of the core, raising-up the internal temperature for the ignition of oxygen or silicon. If the star collapses into a BH before its helium core enters the PI regime and it is inside a dense stellar environment, it has a chance to capture a companion by dynamical exchange. For example, BHs in AGN disks might pair with other BHs and are expected to merge due to gas torques, producing second generation BHs. For stars with helium core mass in the range $32 \geq M_{He}/M_\odot \geq 64$, the instability manifests as Pulsational Pair Instability (PPI): the star undergoes a number of oscillations that eject material and remove the stellar envelope, bringing the star back to a stable configuration after the mass loss. After PPI, the star ends its life with a core-collapse supernova and if it is in a dense stellar environment and is not ejected by the gravitational recoil, it has a chance to form a new binary system with another BH. Alternatively, a gravitational bond between a carbon-oxygen core and a main sequence star might form a binary with an over-sized envelope that will finish it's life collapsing into a giant BH. For larger star's helium core mass $64 \geq M_{He}/M_\odot \geq 135$, PI drives to a complete disruption of the star leaving no compact object, or to a direct collapse to a giant BH. The combined effect of PI and PPI is expected to carve a mass gap in the BH mass function, with a lower boundary of $\approx 50 - 65\ M_\odot$ and an upper boundary of $\geq 120\ M_\odot$. However, these boundaries of the mass-gap are highly uncertain because they depend on stellar evolution and on our understanding of PI and PPI supernovae instabilities.

The mechanisms which could fill the PI gap for BBH masses can be divided in the following possible scenarios:

- Hierarchical merger scenario [37]: A second generation (2g) BH can be formed by a previous first generation-first generation (1g-1g) BHs merger in a dense star cluster or through migration-mediated interactions in an AGN disk. When formed, a 2g BH is subject to a relativistic gravitational recoil velocity (kick) which can eject it from its birth-place, subsequently may acquire a new companion through dynamical exchanges. The companion can be a 1g BH or a 2g BH [38]. The relativistic kick at birth strongly depends on BH spin: maximally spinning BHs or counter-aligned spin BHs receive the largest kicks. Hierarchical mergers are expected to happen more likely in globular clusters which have the highest escape velocity, rather than in open clusters and young star clusters. Concerning the predicted mass ratios, from simulations studies results that $1g + 2g$ BHs mergers tend to have more unequal mass ratios than $2g + 2g$ BHs mergers. The preference of GW190521 for a mass ratio $q \approx 1$ suggests that this system is more likely consistent with a $2g + 2g$ BHs (or higher) merger. Spin measurements can be a distinguishing feature of 2g BHs, because merger remnants are expected to be rapidly rotating with $\chi \approx 0.7$. Since they acquire companions through dynamical exchanges, spins are expected to be isotropically distributed with respect

to the orbital angular momentum.

- Stellar merger scenario: If a star grows an over-sized hydrogen envelope with respect to its helium core, it might directly collapse to a BH with mass in the range $\approx 60-100$ $M_\odot$ without entering the PI/PPI regime [34]. For a star to develop this over-sized hydrogen envelope, one or more mergers between a giant helium-core star and a main-sequence star are required [39]. A BH formed by a stellar merger in a globular cluster can acquire a new companion, then a BH can form from triple or multiple stellar systems. The primary mass distribution predicted by the stellar merger model scales approximately as m^{-5} with $m > 60$ $M_\odot$. The expected mass ratio is $q \approx 0.4-0.6$. Hence, the primary mass and the mass ratio predicted by this scenario are compatible with the ones measured for the event GW190521. This scenario predicts high spins isotropically distributed. The key difference between the hierarchical merger scenario and the stellar merger scenario is that the latter does not imply relativistic kicks at birth, hence it might be more common in star clusters [40].

- AGN disk scenario [41]: The nucleus of an active galaxy might hosts tens of thousands of stellar-mass BHs that moved into the innermost orbit. In this dense gaseous environment, BH orbits are efficiently torqued by gas-drag until they align with the AGN disk, where they can acquire companions and merge. When these BHs merge there is a high chance that they are not ejected, because of the high escape velocity (thousands of km s^{-1}). Hence, AGN disks are expected to host 2g BHs with masses in the PI mass-gap. The prediction of mass ratios are highly uncertain but the spin magnitudes are expected to be as high as $\chi \approx 0.7$. Since BH orbits tend to align with the AGN disk, there might be some preference for the aligned-spin configuration. BBH mergers in an AGN disk may have an associated electromagnetic counterpart (ultra-violet flare [42]), however there are no observational evidences.

Searches for IMBH binaries with total mass ≤ 500 $M_\odot$ and primary mass > 100 $M_\odot$ were carried out from initial LIGO and Virgo and from the first and second observing runs, but no significant candidates were identified. From those studies a stringent upper limit of the local IMBH merger rate of ≈ 0.20 $Gpc^{-3}yr^{-1}$ for binaries with equal component masses $m_1 = m_2 = 100$ $M_\odot$ was estabilished. The signal GW190521, under the assumption of stellar merger scenario, yield an estimates of the merger rate for similar systems to be $\approx 0.13^{+0.30}_{-0.11}$ $Gpc^{-3}yr^{-1}$. The merger rate for IMBH formed via AGN disk scenario is $\approx 1 - 10$ Gpc^{-3} yr^{-1} In upcoming future observing runs is expected the detector network's sensitivity to BBH mergers to increase significantly, with potentially several hundreds of detections per year, reaching out redshifts in the range $z = 0.01 - 0.1$ and $z > 100$. We may thereby observe a large sample of events similar to GW190521. This will enable us to better understand the still uncertain natal spin and mass distribution of BHs as a product of stellar collapse including PI, stellar cluster dynamics, merger kicks due to GW emission, and formation channel of highly spinning BHs.

3.2 Spin-induced orbital Precession

When one or both components of a compact binary system are rapidly rotating and the spins form a non-zero angle with the orbital angular momentum $\mathbf{L}$, the spin-spin and spin-orbit interactions cause the binary's orbital plane to precess. The direction of the total angular momentum $\mathbf{J} = \mathbf{L} + \mathbf{S}$ remains constant except for small radiation-reaction effects. For semplicity, it will be assumed the inspiral of the binary in the adiabatic limit so that it's possible to assume that the binary has in every istant circular orbits. With these assumptions the precession equations take the following form, accurate through post[2]-Newtonian order [2]:

$$\dot{\mathbf{L}} = \frac{1}{r^3}\left[\frac{4M_1 + 3M_2}{2M_1}\mathbf{S_1} + \frac{4M_2 + 3M_1}{2M_2}\mathbf{S_2}\right] \times \mathbf{L} \tag{3.3}$$

$$-\frac{3}{2r^3}[(\mathbf{S_2} \cdot \hat{\mathbf{L}})\mathbf{S_1} + (\mathbf{S_1} \cdot \hat{\mathbf{L}})\mathbf{S_2}] \times \hat{\mathbf{L}}$$

$$-\frac{32\mu^2}{5r}\left(\frac{M}{r}\right)^{5/2}\hat{\mathbf{L}}$$

$$\dot{\mathbf{S_1}} = \frac{1}{r^3}\left[\frac{4M_1 + 3M_2}{2M_1}(\mu M^{1/2}r^{1/2})\hat{\mathbf{L}}\right] \times \mathbf{S_1} \tag{3.4}$$

$$+\frac{1}{r^3}\left[\frac{1}{2}\mathbf{S_2} - \frac{3}{2}(\mathbf{S_1} \cdot \hat{\mathbf{L}})\hat{\mathbf{L}}\right] \times \mathbf{S_1}$$

$$\dot{\mathbf{S_2}} = \frac{1}{r^3}\left[\frac{4M_2 + 3M_1}{2M_2}(\mu M^{1/2}r^{1/2})\hat{\mathbf{L}}\right] \times \mathbf{S_2} \tag{3.5}$$

$$+\frac{1}{r^3}\left[\frac{1}{2}\mathbf{S_1} - \frac{3}{2}(\mathbf{S_1} \cdot \hat{\mathbf{L}})\hat{\mathbf{L}}\right] \times \mathbf{S_2}$$

These are a set of coupled differential equations. In the formula of $\dot{\mathbf{L}}$ the terms in the first square bracket which involve one spin are due to post[1.5]-Newtonian order spin-orbit coupling; the terms in the second square bracket involving two spins are due to post[2]-Newtonian order spin-spin coupling; the last term is due to radiation-reaction and it's the only term that changes the magnitude of any of the angular momenta. To the lowest order, radiation-reaction causes $\mathbf{L}$ to decrease in module but does not affect the single spins $|\mathbf{S_1}|$ and $|\mathbf{S_2}|$, i.e. $d\mathbf{S_i}/dt = 0$ the magnitude of the spins is constant during the inspiral. The previous equations implies that:

$$\dot{\mathbf{J}} = \dot{\mathbf{L}} = -\frac{32\mu^2}{5r}\left(\frac{M}{r}\right)^{5/2}\hat{\mathbf{L}} \tag{3.6}$$

Therefore, the loss in magnitude of the total angular momentum $\mathbf{J}$ experienced by the system is caused by the loss of the orbital angular momentum $\mathbf{L}$ rather than the spin. To compute the evolution of a precessing binary we numerically integrate these equations until the adiabatic approximation is no longer valid. This occurs when the binary reaches its Minimum Energy Circular Orbit (MECO, also known as the innermost circular orbit for non-spinning binaries) after which the two compact objects plunges in one other [43]. In the next section we will compute approximate, analytic, solution for $\mathbf{L(t)}$ in two cases of interest. The solution of the precession equations for the case of binaries

with general masses and spins distributions need numerical simulation solutions and it is beyond the scope of this dissertation.

3.2.1 Simple Precession motion

In this section we derive the solutions of the inspiral and precession equations for two cases: 1) $M_1 = M_2$, which could rapresent a symmetric BBH system; 2) $\mathbf{S_2} = 0$, which could represent a very asymmetric system ($m_1 >> m_2$). In the latter case, the spin $\mathbf{S_1}$ of the larger body will dominate the orbital precession, unless it is parallel or anti-parallel to $\hat{\mathbf{L}}$. Spin-Spin effects can be ignored since they occur at higher post-Newtonian order (2PN) and are therefore typically smaller than the leading spin-orbit term (1.5PN). Also, spin-spin effects are not present for a system with only one spinning component. For both cases under examination, the motion of $\hat{\mathbf{L}}$ is a rotation around the nearly fixed direction of $\hat{\mathbf{J}}$ occurring in a time scale much longer than the orbital period. Precession can result in a short epoch characterized by a qualitatively different motion of $\hat{\mathbf{J}}$ if the spins are large and initially approximately anti-aligned with $\hat{\mathbf{L}}$. In fact, $\hat{\mathbf{L}}$ slowly shrinks due to GW emission while $\mathbf{S_1}$ and $\mathbf{S_2}$ are constant. At some point $\hat{\mathbf{J}}$ will transition from being dominated by $\hat{\mathbf{L}}$, to being dominated by $\mathbf{S_1} + \mathbf{S_2}$. This phenomenon is called *transitional precession* and leads to an episode of complicated three- dimensional tumbling of the binary. Once the vectors have been re-oriented and the transition ends, simple precession is typically restored. Neglecting the spin-spin coupling, the equations governing the orbital plane's precession become[2]:

$$\dot{\mathbf{L}} = \frac{-32\mu^2}{5r} \left(\frac{M}{r} \right)^{5/2} \tag{3.7}$$

$$\dot{\mathbf{S}} = 0 \tag{3.8}$$

$$\dot{\hat{\mathbf{L}}} = \left(2 + \frac{3M_2}{2M_1} \right) \frac{\mathbf{J}}{r^3} \times \hat{\mathbf{L}} \tag{3.9}$$

$$\dot{\hat{\mathbf{S}}} = \left(2 + \frac{3M_2}{2M_1} \right) \frac{\mathbf{J}}{r^3} \times \hat{\mathbf{S}} \tag{3.10}$$

Following the discussion in [2], let's describe qualitatively the solutions of the evolution equations obtained. The orbital evolution consists in two motions: a precession of the plane containing $\mathbf{L}$ and $\mathbf{S}$ and the motion of these vectors in this plane. The in-plane evolution is driven by radiation-reaction induced orbital shrinkage, $|S|$ will remain almost constant during the course of inspiral while $|L|$ will decay with time. The precession of the plane containing $\mathbf{L}$ and $\mathbf{S}$ can take two different behaviours: i)*simple precession* occurs when $\mathbf{J} > 0$ and both $\mathbf{L}$ and $\mathbf{S}$ precess around a near constant $\mathbf{J}$ with an angular velocity given by:

$$\Omega_p = \left(2 + \frac{3M_2}{2M_1} \right) \frac{\mathbf{J}}{r^3} \tag{3.11}$$

$\mathbf{J}$ changes in magnitude but not in direction; ii) *transitional precession* occurs when $\mathbf{L}$ and $\mathbf{S}$ are anti-aligned such that $\mathbf{J} \sim 0$ and the system tumble randomly in space

---

[2]To derive these simplified precession equations we used the result that $J \times L = (L + S) \times L = (L \times L) + (S \times L)$ reduces to $J \times L = S \times L$ (and similarly $J \times S = L \times S$)[44].

and causes **J** to swing around a new direction (see figure 3.2). At this point **L** and **S** resume their simple precession motion but now around the new direction of **J** [2]. The strenght of the precession can be characterized by the precession angle defined
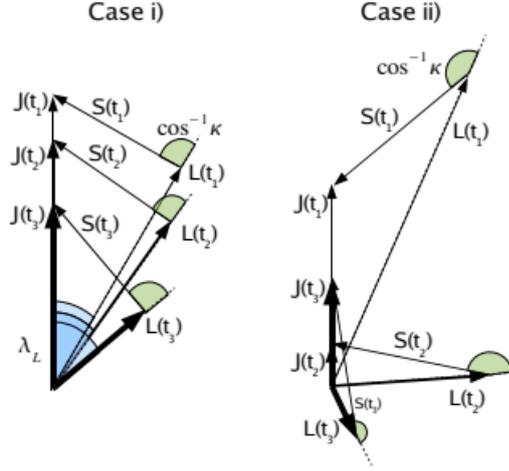
Figure 3.2: The evolution of orbital angular momentum L, spin angular momentum S and total angular momentum J during simple and transitional precession. In case i) only simple precession occurs as J remains relatively large and roughly constant in direction while L and S precess about it. In case ii) the evolution undergoes simple precession at early times t_1 until the time t_2 when L has become anti-aligned with S with equal magnitudes, so that $\mathbf{J} = \mathbf{L} + \mathbf{S} \sim 0$. The system will undergo a period of transitional precession, during which the system will tumble randomly in space, until $|\mathbf{L}| < |\mathbf{S}|$ and simple precession is resumed at time t_3. This figure is based upon figure 2 in [2].

as $d\alpha/dt = \Omega_p$ and by the opening angle of the precessing cone λ_L between **J** and **L**, which is determined primarily by the total spin in the plane and the binary's mass-ratio. At leading order, the magnitude of the binary's orbital angular momentum is $L = \mu\sqrt{Mr}$, then we can write [45]:

$$\cos \lambda_L(t) = \hat{\mathbf{L}} \cdot \hat{\mathbf{J}} = \frac{\mu\sqrt{Mr(t)} + S_{||}}{\left[(\mu\sqrt{Mr(t)} + S_{||})^2 + S_{\perp}^2\right]} \tag{3.12}$$

where $S_{||}$ and $S_{\perp}$ are the total spin components parallel and perpendicular to L respectively, and rest approximately constant during the inspiral (see figure 3.3). In general, the larger the opening angle and stronger is the precession. However, in the regime of simple precession motion λ_L slowly increases during inspiral and also tipically varies very little over the duration that is visible in GW detectors, so that it's possible to make the semplifying assumption that it remains constant in time. By integrating the equation 3.12, one can obtain an estimate of the number of precessions observable in the frequency sensitivity range of GW detectors, and how it scales with the frequency of the emitted GWs. For this purpose we consider two options: i) when $\mathbf{L} \gg \mathbf{S}$ we
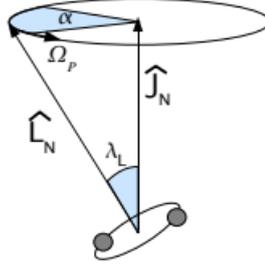
Figure 3.3: During simple precession the orbital angular momentum L of the binary will precess about the total angular momentum J with frequency Ω_p. The opening angle λ_L and the precession angle α are also identified.

have $\mathbf{J} \simeq \mathbf{L}$, and the precessing angle is $d\alpha/dt \propto L/r^3 \propto r^{-5/2}$, since the Newtonian angular momentum is $L = \mu M^{1/2} r^{1/2}$ and equation 2.19 implies that $dr/dt \propto r^{-3}$. From these two relations we can compute $d\alpha/dr$ in this way:

$$\frac{d\alpha}{dr} = \frac{r^{-5/2} dt}{r^{-3} dt} \propto r^{1/2} \tag{3.13}$$

integrating in dr we have $\alpha(r) \propto r^{3/2}$ or $\alpha(f) \propto f^{-1}$ where f is the frequency of the emitted GW at orbital separation r^3. That is, most of the precessions occurr at low frequencies and the precessing angle takes preferentially small values (the cone of precession is narrow when S is small); ii) when $S >> L$ we have $J \simeq S$, then $d\alpha/dr \propto S/r^3$. But we know that the total spin is constant in time, i.e. $dS/dt = 0$, therefore $d\alpha/dt$ is also constant and we have $\alpha(r) \propto r$ or $\alpha(f) \propto f^{-2/3}$. Putting back the constant factors that we omitted for the computation, we find the following power law:

$$\frac{\alpha(f)}{2\pi} \approx \begin{cases} 11(1 + \frac{3M_1}{4M_2})\frac{10M_\odot}{M}\frac{10Hz}{f} & \mathbf{L} >> \mathbf{S} \\ 1.9(1 + \frac{3M_1}{4M_2})\frac{M_1}{M_2}\frac{S}{M_2}\left(\frac{10M_\odot}{M}\frac{10Hz}{f}\right)^{2/3} & \mathbf{S} >> \mathbf{L} \end{cases} \tag{3.14}$$

An interesting consideration is that in the case $L >> S$ the number of precessions is independent of the total spin and we can assume that slowly spinning bodies produce roughly as many as precessions as rapidly spinning ones. However, during the inspiral the precessing motion is much slower than the orbital motion, as a consequence the precessing motion contributes relatively little to the loss of energy due to gravitational radiation, and therefore is weak during the inspiral. The main effect of precession will be an amplitude modulation as the orbital plane precesses and radiates GWs predominantly in the direction orthogonal to the orbital plane.

3.2.2 Algebraic solution to Simple Precession equations

Following the analysis given in [2], we derive now an algebraic expression for the formulas needed to compute the simple precession motion. It is convenient to introduce

---

[3] From the third Kepler's law $\omega_{GW}^2 = GM/r^3$ and knowing that $f = \omega/2\pi$, we derive $f^2 \propto r^{-3}$

the following notation:

$$\kappa \equiv \mathbf{S} \cdot \mathbf{L} \qquad\qquad \gamma(t) \equiv \mathbf{S}/\mathbf{L(t)} \qquad (3.15)$$

where κ is a constant of the motion as a consequence of the eq. (3.7) and (3.8), γ grows with time but it is bounded above by:

$$\gamma \leq \frac{M_1^2 + M_2^2}{M_1 M_2} \left(\frac{M}{r}\right)^{1/2} \qquad (3.16)$$

The magnitude and direction of the total angular momentum can be expressed as:

$$\mathbf{J} = \mathbf{L}\sqrt{1 + 2\kappa\gamma + \gamma^2} \qquad (3.17)$$

$$\hat{\mathbf{J}} = \frac{\hat{\mathbf{L}} + \gamma\hat{\mathbf{S}}}{\sqrt{1 + 2\kappa\gamma + \gamma^2}} \qquad (3.18)$$

$\hat{\mathbf{L}}$ and $\hat{\mathbf{S}}$ are precessing around $\hat{\mathbf{J}}$ with the precessional angular velocity given by:

$$\Omega_p = \left(2 + \frac{3M_2}{2M_1}\right)\sqrt{1 + 2\kappa\gamma + \gamma^2}\frac{\mathbf{L}}{r^3} \qquad (3.19)$$

and now we want to determine the motion of $\hat{J}$. This can be achieved differenziating the eq. 3.18 and using the corresponding eq. 3.9 and 3.10, then we obtain:

$$\dot{\hat{\mathbf{J}}} = \frac{\dot{\gamma}[\hat{\mathbf{S}}(1 + \kappa\gamma) - \hat{\mathbf{L}}(\kappa + \gamma)]}{(1 + 2\kappa\gamma + \gamma^2)^{3/2}} \qquad (3.20)$$

From this eq. we can deduce that the motion of $\hat{\mathbf{J}}$ is a circular motion along the great-circle arc (see figure 3.4) produced by the motion of $\hat{\mathbf{L}}$ towards $\hat{\mathbf{S}}$.
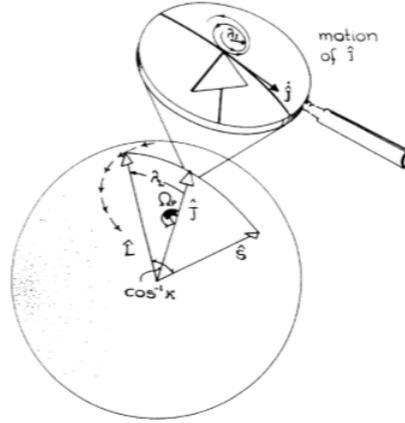
Figure 3.4: Simple precession. $\hat{\mathbf{J}}$ udergoes tight-spiral motion with fixed direction, $\hat{\mathbf{L}}$ and $\hat{\mathbf{S}}$ are precessing around $\hat{\mathbf{J}}$.

The opening angle of the cone generated by the precessing motion of $\hat{\mathbf{J}}$ takes the following expression:

$$\lambda_J = \arcsin\left(\frac{|\dot{\hat{\mathbf{J}}}|}{\Omega_p}\right) = \arcsin\left(\frac{\frac{16}{5}(M/r)^{3/2}\gamma\sqrt{1 - \kappa^2}}{1 + \frac{3}{4}(M_1/M_2)(1 + 2\kappa\gamma + \gamma^2)^{3/2}}\right) \qquad (3.21)$$

Similarly, the opening angle of the precessing cone generated by $\hat{\mathbf{L}}$ in it's motion is given by:

$$\lambda_L = \arcsin\left(\frac{|\dot{\hat{\mathbf{L}}}|}{\Omega_p}\right) = \arcsin\left(\frac{\gamma\sqrt{1-\kappa^2}}{(1+2\kappa\gamma+\gamma^2)^{1/2}}\right) \tag{3.22}$$

Their value changes in time because of the inspiral motion, so $\hat{\mathbf{J}}$ and $\hat{\mathbf{L}}$ undergo tight spirals rather than precise circular motions. Note that even if the precession timescale is much shorter than the inspiral timescale $\Omega_p^{-1} << \mathbf{L}/\dot{\mathbf{L}}$, $\hat{\mathbf{J}}$ can still change significantly in one precession period if it's magnitude is much smaller than the magnitude of $\hat{\mathbf{L}}$ (as can happen if $\mathbf{L}$ and $\mathbf{S}$ are antialigned and have equal magnitude). For this reason, a paremeter $\epsilon = (\mathbf{L}/\mathbf{J})\times$ (ratio of precession timescale to inspiral timescale) is defined, that is:

$$\epsilon = \frac{\mathbf{L}}{\mathbf{J}}\frac{\dot{\mathbf{L}}/\mathbf{L}}{\Omega_p} = \frac{16}{5}\frac{(M/r)^{3/2}}{(1+\frac{3}{4}M_2/M_1)(1+2\kappa\lambda+\lambda^2)} \tag{3.23}$$

being small compared to unity in simple precessionregime. It can be demonstrated that:

$$\frac{sin\lambda_J}{sin\lambda_L} = \epsilon \tag{3.24}$$

Thus, for ϵ being small means that for simple precession motion the condition $sin\lambda_J << sin\lambda_L$ holds.

3.3 Detector response to Gravitational Waves from a Precessing Binary

After writing down the post-Newtonian equations that describe the precession of the orbital plane, we derive the equations that describe the corresponding modulations in the GW signature [46]. The equations are simply obtained using the same formulas 2.13 and 2.18 of the non-precessing case for the wave fields $h_+(t)$ and $h_\times(t)$ and for the amplitude $A(t)$ and polarization phase φ respectively, but replacing in those expressions the time varying $\hat{\mathbf{L}}(\mathbf{t})$ derived by solving the precession equations 3.3. Thus, the precession-modulated GW can be written as:

$$h_+^p(t) = -\frac{2\mu M}{rD}\left[1+(\hat{\mathbf{L}}(t)\cdot\hat{\mathbf{N}})^2\right]\cos 2\phi(t) \tag{3.25}$$

$$h_\times^p(t) = -\frac{2\mu M}{rD}\left[-2\hat{\mathbf{L}}(t)\cdot\hat{\mathbf{N}}\right]\sin 2\phi(t)$$

And the detector strain as well:

$$h^p(t) = -A(t)\cos[2\phi(t)+\varphi(t)] \tag{3.26}$$

where the amplitude and the phase assume the following expressions:

$$A(t) = \frac{2\mu M}{rD} \left([1 + (\hat{\mathbf{L}}(t) \cdot \hat{\mathbf{N}})]^2 F_+^2(\theta, \phi, \psi(t)) + 4[\hat{\mathbf{L}}(t) \cdot \hat{\mathbf{N}}]^2 F_\times^2(\theta, \phi, \psi(t)) \right)^{1/2}$$
(3.27)

$$\varphi(t) = \arctan^{-1} \left(\frac{2\hat{\mathbf{L}}(t) \cdot \hat{\mathbf{N}} F_\times(\theta, \phi, \psi(t))}{[1 + (\hat{\mathbf{L}}(t) \cdot \hat{\mathbf{N}})]^2 F_+(\theta, \phi, \psi(t))} \right)$$
(3.28)

The precession causes also the polarization angle to vary in time, and it's given by:

$$\psi(t) = \arctan \left(\frac{\hat{\mathbf{L}}(t) \cdot \hat{\mathbf{z}} - (\hat{\mathbf{L}}(t) \cdot \hat{\mathbf{N}})(\hat{\mathbf{z}} \cdot \hat{\mathbf{N}})}{\hat{\mathbf{N}} \cdot (\hat{\mathbf{L}}(t) \times \hat{\mathbf{z}})} \right)$$
(3.29)

Recall that in section 2.1.2 we introduced a distinction between the *carrier phase* $\phi_C(t)$, defined as the integral of the bodies's angular velocity in the orbital plane, and $\phi(t)$, defined as the angle between the orbital separation $\hat{r}$ and the principal $+$ direction $\pm\hat{\mathbf{L}} \times \hat{\mathbf{N}}$. We define now the precessional correction to $\phi(t)$ which arises from the changing orientation of the orbital plane as $\phi(t) \simeq \phi_C(t) + \delta\phi(t)$, where:

$$\delta\phi(t) = - \int_{t_c}^{t} \left(\frac{\hat{\mathbf{L}} \cdot \hat{\mathbf{N}}}{1 - (\hat{\mathbf{L}} \cdot \hat{\mathbf{N}})^2} \right) (\hat{\mathbf{L}} \times \hat{\mathbf{N}}) \cdot \hat{\mathbf{L}} \, dt$$
(3.30)

It depends on the full time history of $\hat{\mathbf{L}}$ between times t and t_c and by the uncertainity in the position of the binary in the sky. The precession modulated waveform with the phase correction due to the precession assumes then the following expression:

$$h(t) = -A(t)\cos[2\phi_C(t) + 2\delta\phi(t) + \varphi(t)]$$
(3.31)

the term $2\delta\phi$ can change the total number of the cycles in the wave fields and the observed waveform by roughly twice the total number of precessions. For the computation of $A(t)$ and $\varphi(t)$ one need to solve the equations 3.3 for $\hat{\mathbf{L}}(t)$ and plugs the result into equations 3.27.
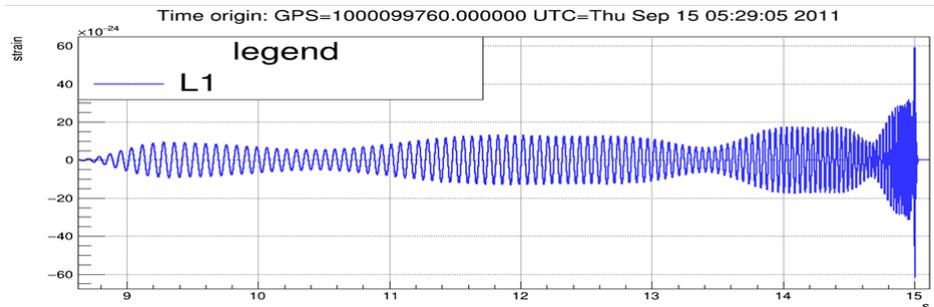
Figure 3.5: Example of a precessing GW signals with modulations in phase and amplitudes.

3.4 Observability of precession in GW signals

The first basic picture of the precession effects comes from the opening angle defined in eq. 3.12. In simple precession cases $\cos \lambda_L$ slowly increases during the inspiral, so that $\mu, M, S_{||}$ and $S_\perp$ can be considered approximately constant. If we consider the case where the spin is entirely in the orbital plane, i.e. $S_{||} = 0$, then, $\cos \lambda$ will be zero if $S_\perp = 0$ and increase linearly for small $S_\perp$ and as μ decreases. If we consider $S_{||} \neq 0$, the strenght of precession will be reduced for systems with a positive aligned-spin component and increased for those ones with negative aligned-spin component [47]. A negative $S_{||}$ is necessary to achieve large opening angles ($> 90°$) but such systems are considerate to be rare [48]. The measurability of precession also depends on the orientation of the binary with respect to the detector [49]. In particular, Precession effects will be minimal if the source is face-on oriented $\theta_{JN} \sim 0°$ or $180°$, i.e. the observer is along the direction of $\hat{J}$, and will be strongest for binaries edge-on oriented $\theta_{JN} \sim 90°$. The parameter χ_p or precessing-spin, defined as [50]:

$$\chi_p = \frac{1}{A_2 m_2^2} max(A_1 S_{1\perp}, A_2 S_{2\perp}) \tag{3.32}$$

with $A_1 = 2 + 3q/2$, $A_2 = 2 + 3/2q$ and $q = m_1/m_2(m_1 > m_2)$, estimates a time-average of the in-plane spin components that drive precession and takes values between zero (non-precessing systems) and $+1$ (maximally precessing systems). However, In most cases GW data analysis provide a well-constrained spin quantity called effective spin χ_{eff}, which is the mass weighted combination of the projection of the two spins along the orbital angular momentum [51]:

$$\chi_{eff} = \frac{m_1 S_{1||} + m_2 S_{2||}}{m_1 + m_2} \tag{3.33}$$

The impact of χ_p on GW signals is much lower than of χ_{eff} and therefore its measurement is less precise. However, the authors in [52] and in [53] show that if they do not include χ_p in their analysis, they would lost substantial information, despite the large uncertainties. To date, almost all detection searches of LIGO-Virgo ignored the effects of spins-precession and the evidences of spin-induced orbital precession were searched by either calculating Bayes factors or statistically comparing posterior distributions for parameters characterizing precession to their prior distributions. However, the authors in this study [54] suggest to use a new statistic (SKY-maxed SNR) to search for compact objects with generic spins. Applying this statistic for the construction of template banks and using them in a real pipeline analysis of simulated Gaussian noise, two important results have been found: i) despite that the generic spin banks have a roughly a factor of ten more templates than the aligned-spin banks and the increase of background rate, in certain regions of the parameter space, namely at high mass-ratios and large in-plane spins, there is an overall improvement of about 7% in signal recovery at a fixed false-alarm rate ii) this gain in sensitivity comes at small loss of sensitivity of about 4% for systems that are already well covered by aligned-spin templates. In recent years others studies explored the general phenomenology of precession effects, invastigating where in the parameter space will be possible to accurately identify precession and it's impact on GW searches. As expected, the evidence for precession increases with large in-plane

spins, more unequal components masses and edge-on oriented sources, as reported in [55]. We will use the methods and the considerations mentioned in this section for the data analysis proposed in this work.

"Salimmo sù, el primo e io secondo,
tanto ch'i' vidi de le cose belle
che porta 'l ciel, per un pertugio tondo.
E quindi uscimmo a riveder le stelle."
Dante Alighieri, Inferno

Chapter 4

Detecting Precessing Gravitational Waves signals

4.1   Introduction

In the next two chapter I will describe the results of my research work, which aimed to improve the sensitivity search of the data analysis pipeline MBTA to GW signals emitted by spin-precession binary black holes systems. The current detection searches for GW from compact object binaries employ only waveforms models with spin aligned (or anti-aligned) with the orbital angular momentum. However, parameter inference algorithms consider precessing waveforms and it's already demostrated that for systems with strong precessional features it's possible to break the degeneracies between physical parameters in the emitted GW signal and therfore better measure the component spins. The data analysis problem for the spinning case is complicated by the large number of parameters needed to characterize the system, including the initial directions of the spins, position and orientation of the binary with respect to the detectors. In addition, some complications arise when using the matched filtering technique. The latter is the detection strategy commonly used to extract GW signals from noise and is based on evaluating the correlation between the detector output data and a set of waveforms models that must reproduce the expected signal. It is an optimal filter method in Gaussian noise, however the output data of interferometers are often contaminated by non-gaussian transient noises called *glitches*, which can have instrumental and environmental origin. To reduce the effects of these non-stationarities signal-based vetos can be defined to rejects triggers.

The filter output can be maximized using waveforms models that describe as more accurately as possible the expected signal involving more parameters, for instance the spin of the single components.We will describe a phase, amplitude and sky location maximized SNR statistic, also called sky-maxed SNR, applicable to search for binary systems carrying generic (precessing) spins. This statistic is applied for the generation of template banks for both Aligned-Spin (AS) and Precessing-Spin (PS) BBH systems as well as for the computation of their effectiveness i.e. their ability to recover injected signals of simulated population of generic-spin systems). These banks are then analized in Gaussian noise and in realistic data by running Monte Carlo tests with the pipeline MBTA, with the purpose of i) check the ability of the pipeline MBTA to detect precess-

ing simulated GW signals (injections) and discriminate them from glitches in the data; ii) investigate the expected gain in signal power when using PS banks compared to AS banks, due to having templates which more accurately model the precession effects; iii) measure the increase of background false-alarms incurred by filtering the data with more templates.

In this chapter we focus on the generation and validation of the template banks, with a detailed description of the parameters-space, waveforms approximants and tools employed; the next chapter will be focused on the data analysis results with MBTA. For PyCBC tools references see [56],[57],[58], [59], [60], [61].

4.2   The matched filtering technique

The standard filter choice for GW from compact binaries coalescences (CBC) is the match-filtering technique, since the expected signal is well modeled. It consists in computing the correlation between the data and a bank of templates (also called filters) corresponding to the expected signal waveforms. The parameters of the source are in general not known a-priori, so the data must be correlated with many possible expected signal waveforms. A generic GW signal generated by the coalescence of compact binary system is described by 15 parameters (ignoring the eccentricity and the parameters of the internal structure of neutron stars for NS-BH systems): the component masses m_1, m_2; the component dimensionless spin vectors χ_1, χ_2; the sky location of the signal with respect to the frame of the observer (θ, ϕ); the distance D of the the source; the coalescence time t_c; the inclination of the binary with respect to the line-of-sight to the system ι; a polarization angle Ψ; and an orbital phase at coalescence ϕ_c. The approximation of the waveform model should be chosed such that it mimics as most accurate as possible the expected signal, to make the matched filter output effective. Theoretical signal templates can be calculated by employing perturbative-or numerical simulations to solve the Einstein's equations of GR. During the early stage of the coalescences, called Inspiral, the dynamics of the binary as well as the expected GW weveform can be calculated using PN approximation to GR. the templates that have to model the complete inspiral-merger-ringdown stages requires imputs from Numerical relativity simulation and perturbative General Relativity. Proper calculation of the GW from the merger of the binaries involving NSs also requires considering the effect of nuclear matter, in addition to GR.

The templates bank can be considered the collection of points that span the parameter space. Consider the data output $s(t)$ of a GW detector which consist of noise $n(t)$, that we assume both stationary and Gaussian, and eventually of GW signal of known shape $h(t)$: under the Gaussian assumption, it's possible to express the probabilities of noise hypothesis $s(t) = n(t)$ and signal hypothesis $s(t) = n(t) + h(t)$ of the observed data respectively as:

$$P(s|n) \propto e^{-\Re[\langle s|s \rangle]/2} \tag{4.1}$$

$$P(s|h) \propto e^{-\Re[\langle s-h|s-h \rangle]/2} \tag{4.2}$$

where $\Re$ indicate the real part. The inner product between the detector strain and the GW signal define the filter output and is given by:

$$\langle s|h \rangle = 4\Re \int_0^\infty \frac{\tilde{s}(f)[\tilde{h}(f)]^*}{S_n(f)} df \tag{4.3}$$

where the tilde indicates the Fourier transform, the asterisk is the conjugate complex and $S_n(f)$ is the one sided ($f > 0$) spectral power density which describe the statistical properties of the noise. The log-likelihood ratio $\Lambda \equiv P(s|h)/P(s|n)$ between the signal and noise hypothesis define the general prescription for searching for a GW signal of known form in stationary and Gaussian noise:

$$log\Lambda \equiv \lambda = \Re[\langle s|h \rangle] - \frac{1}{2}\Re[\langle h|h \rangle] \tag{4.4}$$

The output of the matched filter, the signal-to-noise ratio (SNR), is directly related to the probability that a GW signal is buried in the data, thus we define the matched-filter SNR, ρ, by maximizing λ over an overall amplitude:

$$\rho^2/2 = max(\lambda)|_{amp} = \frac{(\Re[\langle s|h \rangle])^2}{\langle h|h \rangle} = (\Re[\langle s|\hat{h} \rangle])^2 \tag{4.5}$$

and we recall here the phase-maximized filter SNR for non-precessing templates:

$$max(\lambda)|_{D,\phi_c,\theta,\phi,\psi} = \frac{1}{2}max(\rho^2)|_{\phi_c} = \frac{1}{2}|\langle s|h_+ \rangle|^2 \tag{4.6}$$

The observed signal $h(t)$ at the detector is the sum of the two gravitational polarization h_+ and $h_\times$ multiplied by the response function of the detector F_+ and $F_\times$ to each polarization, shown in the formula (2.16). The exact form of the signal is not known and it's necessary to maximize over a priori unknown template parameters which determine the expected signal. For some parameters the maximization step can be performed analytically, or in a computationally efficient way using fast Fourier transform (FFT) algorithms, whereas for the remaining ones, one has to repeat the matched-filter operation a large number of times. In making the connection between the two waveforms polarizations and the template waveform $h(t)$, aligned-spin searches rely on the assumption that only the quadrupole $(l, |m|) = (2, 2)$ modes of the waveform are dominant, neglecting the subdminant modes. Additionally, for AS searches the stationary phase approximation holds and the two polarizations are identical up to an amplitude scaling that only depends on ι and a constant phase shift $h_+ = \pm ih_\times$. As a results, it is possible to quickly maximize over all parameters describing the system except for the two masses and the projections of the spins in the direction of the orbital angular momentum $\epsilon = (m_1, m_2, \chi_{1z}, \chi_{2z})$. When we consider waveforms with generically oriented spins, we have to take into account that there are six dimensionless spin components and that the orientation of the source with respect to the detector varies as the orbit precesses. Furthemore, detectors have different orientations and locations so they will not observe the same combination of the source sky angles and the approximization $h_+ = \pm ih_\times$ no longer holds. In the next section we will derive the mathematical formalism of the sky maxed SNR statistic applicable to precessing spin systems, which maximizes the matched-filter SNR over the detector sky-location of the source in addition of the phase and amplitude of the observed signal.

4.2.1 The Sky-Maxed SNR statistic

For the precessing spin template, the signal $h(t)$ is rewrited expressing the detector related angles (θ, ϕ, ψ) and the distance of the source D in terms of an overall amplitude and phase between the GW polarizations:

$$h = K(\theta, \phi, \psi, D)[h_+(t; t_c, \epsilon, \iota, \phi_c) \cos k(\theta, \phi, \psi) + h_\times(t; t_c, \epsilon, \iota, \phi_c) \sin k(\theta, \phi, \psi)] \tag{4.7}$$

where $\epsilon = (m_1, m_2, \hat{\chi}_1, \hat{\chi}_2)$ and we factorize the amplitude and the phase as:

$$e^{ik} = \frac{F_+ + iF_\times}{\sqrt{F_+^2 + F_\times^2}} \tag{4.8}$$

$$K = \frac{1}{D}\sqrt{F_+^2 + F_\times^2}$$

In a similar manner for the aligned-spin case, it's possible to perform the maximization over the amplitude and the phase, but this would leave the additional parameters ι and the sky angles plus the four new spin components to be covered using a discrete bank. The sky maxed SNR statistic consider a scheme that maximize not only over the overall amplitude and phase, but also over the sky-location dependent antenna factors, removing all the detector-dependent quantities from the parameters used when constructing the template bank, allowing to use the coincidence method for a multi-detector analysis. In practice, maximizing the log-likelihood defined in equation (4.6) over K and ϕ_c leads to:

$$max(\lambda)|_{K,\phi_c} = \frac{1}{2} \frac{u^2|\rho_+|^2 + 2u\gamma + |\rho_\times|^2}{u^2 + 2I_{+\times} + 1} \tag{4.9}$$

where we define:

$$\rho_{+,\times} = \langle s|h_{+,\times}\rangle \tag{4.10}$$

$$\gamma = \Re[\rho_+ \rho_\times^*]$$

$$\langle h_+|h_\times\rangle = I_{+,\times} + iJ_{+,\times} \qquad\qquad I_{+,\times}, J_{+,\times} \in \Re$$

and the sky angles dependence is factorized in terms of:

$$u \equiv \frac{1}{\tan k}\sqrt{\frac{\langle h_+|h_+\rangle}{\langle h_\times|h_\times\rangle}} \tag{4.11}$$

but we need to further reduce the dimension of the parameter space, to do so we derive the equation (4.9) with respect u and solving for the roots leads to a quadratic equation in u:

$$(I_{+\times}|\rho_+|^2 - \gamma)u^2 + (|\rho_+|^2 - |\rho_\times|^2)u + (\gamma - I_{+\times}|\rho_\times|^2) = 0 \tag{4.12}$$

substituting the roots of this equation back in the equation (4.9) one obtain two extremal values for λ. We are interested in the maximum value of the log-likelihood (i.e. when

the square-root term is positive), then we take the positive extremal value to obtain:

$$max(\lambda)|_{K,\phi_c,u} =$$

(4.13)

$$\frac{1}{4}\Big(\frac{|\rho_+|^2 - 2\gamma I_{+,\times} + |\rho_\times|^2 + \sqrt{(|\rho_+|^2 - |\rho_\times|^2)^2 + 4(I_{+\times}|\rho_+|^2 - \gamma)(I_{+\times}|\rho_\times|^2 - \gamma)}}{1 - I_{+,\times}^2}\Big)$$

this equation is the log-likelihood maximized over an overall amplitude, phase and sky location of the binary. The terms within the square root will always take positive values and therfore produce real and positive values for λ. Additionally, for precessing waveforms it's not possible for h_+ and $h_\times$ to be identical, so the ill defined case for $I_{+,\times} = \pm 1$ can never occur. Notice that the likelihood can be maximized over the colascence time t_c by computing $\rho_{+,\times}$ for a discrete set of values of t_c using FFT algorithm and piking the largest value of λ, however this case requires the computation of two inverse FFT which increase the computational cost of the search. In analogy to the non-precessing case, we define the sky-maxed SNR for the matched-filter threshold, ρ_{SM}, as:

$$max(\lambda)|_{K,\phi_c,u} = \frac{1}{2}max(\rho^2)|_{\phi_c,u} = \frac{1}{2}\rho_{SM}^2 \qquad (4.14)$$

In the non-precessing limit the sky maxed SNR formula collaps in the equation usually used for AS searches. Infact, if $h_+ = \pm i h_\times$ then:

$$\rho_+ = \pm i\rho_\times \qquad (4.15)$$
$$I_{+,\times} \equiv \Re[\langle h_+ | h_\times \rangle] = 0 \qquad (4.16)$$

and inserting these conditions in equation (4.9), the latter collapse to the form (4.6).

4.3 A stochastic placement algorithm for spinning Template Banks

The PyCBC's tool **Sbank**[1] is an algorithm used for the generation of matched-filter template banks in an arbitrary parameter space, developed for minimize the computational cost without reducing the detactibility of signals. The framework use a positive-definite metric to measure the fractional loss in (squared) SNR of a putative signal filtered through the optimal filter. The metric gives the geometric structure of a Riemannian manifold (or signal manifold) but we refer to it as parameter space. Sbank can also compute template banks using direct matches instead of a metric. In the absence of a metric the distances between points in the parameter space are computed by generating both waveforms and calculating an explicit overlap between them. The latter is optimal for the generation of generic-spin oriented waveforms, such as the IMRPhenomX metric, but one should take into account that when using the direct match method the computational cost is much higher. Since the number of templates have to be finite, the

---

[1]In 2021 Sbank has been split-off from the larger LALsuite package as a standalone module.

parameter space will be covered with a discrete lattice and to evaluate the maximum SNR that is lost due to the discretization of the parameter space , the minumum match (or maximum mismatch) among templates has to be computed, defining the match berween two templates as:

$$\mathcal{M}(h_i, h_j) = max \frac{(h_i, h_j)}{\sqrt{(h_i, h_i)(h_j, h_j)}} \qquad (4.17)$$

The algorithm works as follow:

- begin with a seed bank $\mathcal{B}$ which may be empty;

- randomly choose the parameters $\vec{\lambda}$ of a target signal g and compute the corresponding waveform h;

- a match $M(g, h)$ is computed between g and all the templates included in the bank $h \in \mathcal{B}$, where $M(g, h)$ defines the fraction of the signal power of g that would be recovered if using the template h as the optimal filter;

- the Fitting Factor (FF) for a template is defined as the match maximized over all the templates in the bank $FF(\vec{\lambda}, \mathcal{B}) \equiv maxM(h_i|g)$. The correspondent template mismatch will be 1-FF;

- if the FF falls below a given threshold ("minimal match") then the proposed template is added to the bank, otherwise is discarded;

- continue this process until no new points are added, because they are too close to the previously retained points or some others stopping criterion are met.

When constructing the template banks the discretization of the parameter space is governed by three requirements[61]: cover the full parameter space as densely as possible; the templates have to be placed over the parameter space such that the loss of SNR due to the mismatch of two close templates with arbitrary values of the parameters is minimal; the computational cost of the search using the full template bank need to be manageable. For the aligned-spin placement the match is calculated using the phase-maximized matched-filter SNR:

$$M(g, h) \equiv max|_{\phi_c, t_c} \Re[\langle g|h(\phi_c, t_c)\rangle] = max|_{t_c} \langle g|h(0, t_c)\rangle| \qquad (4.18)$$

The maximization over time and phase shift is performed only on the template h and not on the proposed waveform g because the match doesn't depend on the sky position or orientation of the source. A minimal match of 0.97 is chosed which imply a maximum loss of 3% in SNR power. For the precessing waveform placement the match is calculated with the sky-maxed SNR:

$$M(g, h) \equiv max|_{(\phi_c, t_c, u)} \Re[\langle g|h(\phi_c, t_c, u)\rangle]] \qquad (4.19)$$

In the precessing case the maximization over ϕ_c and u is made only in the template waveform and not on the proposed waveform g. A putative signal $h(t)$ is conputed chosing a specific sky location and orientation and compared versus the h_+ and $h_\times$

components of all the templates in the banks using the equation (4.17). If the putative signal is accepted in the bank, the sky location and $h(t)$ are discarded and only the h_+ and $h_\times$ components of that point are retained. This choise will result in an increase of the number of proposed points, for this reason a lower MM = 0.90 is chosen, increasing the maximum loss of SNR power to 10%. The bank generation output is a file with the list of parameters of the templates. The stochastic template bank should not over-populate the parameter space, however if it properly populates all regions depends by the properties of the signal manifold, infact the distribution of the resulting points strongly depends upon the choise of the coordinate system. The most obvious coordinates on the signal manifold are the masses m_1 and m_2 of the two components compact objects, but using the masses the determinant of the metric may vary significantly over the parameter space and as a consequence a much higher density of templates may be needed in the low mass region with respect to the high mass region. A better coordinate system is rapresented by the *chirp times*, defined bas:

$$\theta_1 = \frac{5}{128\nu}(\pi f_L)^{-5/3}, \qquad\qquad \theta_2 = \frac{-\pi}{4\nu}(\pi M f_L)^{-2/3} \qquad (4.20)$$

$$\tau_0 = \frac{\theta_1}{2\pi f_L}, \qquad\qquad \tau_3 = \frac{\theta_2}{2\pi f_L} \qquad (4.21)$$

Using this coordinate system the determinant of the metric does not vary much ove the parameter space and can be considered approximately a flat space metric. Sbank is widly used for the generation of templates banks in frequency domain. It can run also in time-domain but many of the optimizations used to speed up the computation do not work for time-domain waveforms, which are often much slower to generate than the frequency-domain ones.

4.3.1 Parameters space and waveforms models

To measure the binary's properties the detector data are cross correlated with a set of theoretical waveform models. The accuracy of the measured parameters depends not only on the strenght of the signal but also on the accuracy of the waveforms. Since the first two observing runs (O1-O2) of LIGO and Virgo two families of waveform models are used to search for BBH coalescences, IMRPhenom (Ref. [62], [63], [64]) and SEOBNR (Ref. [65], [66]). Both rely on several physical approximations, although in these models the effect of varying spin directions on the full waveform remains unmodelled. Based on the BH spin configurations, coalescing BBH systems with spins can be considered to be:

- Aligned-Spin: the BH spins are paraller or anti-parallel to $\mathbf{L}$, so $\mathbf{L} \times \mathbf{S_i} = 0$ ($i = 1, 2$) for each BH. From the symmetries of the system, the BHs orbit in a fixed plane, that is the direction of the orbital angular momentum $\hat{\mathbf{L}}$ remains fixed. In the frame where $\hat{\mathbf{L}}||\hat{\mathbf{z}}$ the symmetry also implies that any linear momentum emission is perpendicular to $\hat{\mathbf{L}}$;

- Precessing-Spin: One or both BHs have non-zero spin components perpendicular to $\hat{\mathbf{L}}$. The precence of the perpendicular compontents of the spins $S_i^\perp$ causes the orbital plane to precess over the course of the coalescence. This leads to

modulations of the amplitude and phase of the waveform. Emission of the linear momentum is now also possible perpendicular to the orbital plane, which breaks the symmetry between the $\pm m$ multipoles.

In this section the parameters of the simulated sources are described. We consider GWs emitted by low masses BBH and high masses BBH. For each type two categories of GW signals are generated, one corresponding to aligned-spin (AS) and the other to precessing-spin (PS). For the former the SEOBNR family approximants [67] are used, for the latter IMRPhenom approximants [68]. We thus generate component masses uniformly in the range $M_{tot} \in [20, \ 100] \ M_\odot$ for low masses BBH, and in the range $M_{tot} \in [100, \ 500] \ M_\odot$ for high masses BBH. The dimensionless spins $a_i \simeq c|S_i|/Gm_i^2$ are uniformly generated in the range $[0, \ 0.99]$ compatibly with the range of validity of the waveform approximants. We will always refer to the masses of the signal observed by the observatory, referred to as detector frame masses. Sources at cosmological distances will be redshifted with respect to the observer, causing the signal to appear to have higher masses than the actual ones measured in the source frame. The choise of the mass ranges addresses the considerations proposed in previous studies, specifically the paper arXiv:160302444v2 for the low mass range and the paper Phys. Rev. D 102, 2020 for the high mass range respectively. To be able to characterize the full range of potential systems, waveforms models of the gravitational radiation emitted by BBHs are continuously being improved. In particular, physical effects associated with unequal masses and misaligned spins have recently been extended in phenomenological models covering the inspiral, merger and ringdown of BBHs [68]. For the generation of our template banks, the following approximants will be employed:

- IMRPhenomTPHM (TM) and IMRPhenomXPHM (FD) approximants which include precession and higher multipoles beyond the dominat quadrupole $(2, \pm 2)$, optimized for high mass systems;

- IMRPhenomTP (TD) and IMRPhenomPv2 (FD) approximants which include precession and the dominant modes $(2, \pm 2)$, suitable for low mass systems;

- SEOBNRv4opt (TD) and SEOBNRv4ROM (FD) approximants are used in both low and high masses ranges and they are the most commonly wavefoms used for aligned-spin searches in MBTA.

The parameter space ranges and the signal starting frequency are chosen identically for the template banks and the simulated signals (injections) used to test the coverage of the banks. All the approximants used are implemented in LSC Algorithm Library Simulation (LALSimulation) repository. However, the models IMRphenomXPHM, IMRPhenomTPHM and IMRPhenomTP are not implemented in Sbank. For adding them in the code I needed to download a copy of the software and modify the executables waveforms.py and tau0tau3.py accordingly. In tables below are listed the number of templates for each template bank obtained in the two mass ranges respectively. Notice that in a first approach of the research, for the low mass template banks in frequency domain, it was chosen to explore a larger mass range with a total mass in the range $[20, \ 200] M_\odot$ and a frequency cut-off of $23 \ Hz$. Subsequently, with new results available in literature regarding the improvement of the detectors's sensitivity and data analysis techniques,

the frequency cut-off was lowered to $15\ Hz$ for the generation of the low mass template banks in time domain.

Time Domain Templates Banks	Low mass range
$q = m_1/m_2$	≤ 9
$M_{tot} = m_1 + m_2$	$[20, 100]\ M_{\odot}$
$|\chi_1|,\ |\chi_2|$	$\leq |0.99|$
$f_{cut-off}$	$15\ Hz$
SEOBNRv4opt (MM=0.97)	3798 templates
IMRPhenomTP (MM=0.90)	4492 templates
IMRPhenomTP (MM=0.93)	14332 templates
IMRPhenomTP (MM=0.95)	35150 templates

Table 4.1: Characterization of low mass templates banks in time domain. Notice that the MM is the minimal match used as threshold for the templates placement.

Time domain Templates Banks	High mass range
$q = m_1/m_2$	≤ 9
$M_{tot} = m_1 + m_2$	$[100, 500]\ M_{\odot}$
$|\chi_1|,\ |\chi_2|$	$\leq |0.99|$
$f_{cut-off}$	$15\ Hz$
IMRPhenomTPHM (MM=0.90)	4423 templates
IMRPhenomTP (MM=0.90)	118 templates
SEOBNRv4opt (MM=0.97)	146 templates

Table 4.2: Characterization of high mass templates banks in time domain. Notice that the MM is the minimal match used as threshold for the templates placement.

Frequency Domain Templates Banks	Low mass range
$m_1,\ m_2$	$[10, 100]\ M_{\odot}$
$M_{tot} = m_1 + m_2$	$[20, 200]\ M_{\odot}$
$|\chi_1|,\ |\chi_2|$	$\leq |0.99|$
$f_{cut-off}$	$23\ Hz$
IMRPhenomPv2 (MM=0.90)	63860 templates
IMRPhenomD (MM=0.97)	3672 templates
IMRPhenomPv2 + seed IMRPhenomD (MM=0.90)	66829 templates
SEOBNRv4ROM (MM=0.97)	3984 templates

Table 4.3: Characterization of low mass templates banks in frequency domain. Notice that the MM is the minimal match used as threshold for the templates placement.

Frequency domain Templates Banks	High mass range
$m_1,\ m_2$	$[50, 250]\ M_\odot$
$M_{tot} = m_1 + m_2$	$[100, 500]\ M_\odot$
$|\chi_1|,\ |\chi_2|$	$\leq |0.99|$
$f_{cut-off}$	$15\ Hz$
IMRPhenomXPHM (MM=0.90)	10338 templates
SEOBNRv4ROM (MM=0.97)	132 templates

Table 4.4: Characterization of high mass templates banks in frequency domain. Notice that the MM is the minimal match used as threshold for the templates placement.

The choise of using waveforms models including HOM in the high mass ranges reflects the results of several studies which have shown that the omission of HOM in searches can reduce the detection of systems with large mass ratio $q = m1/m2 \geq 4$ and large total mass $M = m_1 + m_2 > 100\ M_\odot$ [69]. Infact, for edge-on systems, especially ones with high mass ratio the HOM are an important contribution to the full GW emission. In addition, HOM have a stronger effect in signals emitted by large total mass sources, the amplitude of the HOM grows as the mass ratio q of the system and at high values of total mass M the dominant modes $(2, \pm2)$ can fall below the sensitive band of GW detectors while higher m modes at high frequrncy are still observable. Their presence was also crucial in reducing uncertainties in the mass ratio and component spins of the recently reported unequal-mass binary mergers GW190412 (Abbott et al. 2020a) and GW190814 (Abbott et al. 2020b), the higher-order multipoles enable better constraints of the binary inclination angle which is coupled to the source-frame mass estimates through the luminosity distance D_L, and therefore the redshift. Our purpose is not to compare these different models but rather to understand the effect of adding precession in a search and to quantify the expected gain in SNR recovery when using precessing waveforms rather than aligned spin waveforms. Note that the precessing spin banks have a roughly larger number of templates than the aligned spin banks as expected, due to the increased degrees of freedom of the signal space. The level of agreement between two gravitational waveforms can be ascertained by computing the match $\mathcal{M}$. A value of $\mathcal{M} = 1$ implies the waveforms are in perfect agreement. The smaller the value of $\mathcal{M}$, the larger the disagreement between the two waveforms. In the next section we will compute the effectualness of the banks using the fitting factors distribution as figures of merit.

4.4   Template Banks Effectualness

In order to check if a template bank is able to recover an expected simulated signal, the effectualnsess (or Fitting Factor distribution) of the bank can be computed. The PyCBC's tool Banksim compute the overlaps (fitting factors) $\mathcal{M}(h|g) \in [0, 1]$ for each waveform g_i in the parameter space we consider with the filter waveforms h_i in the template bank. The distribution of fitting factors allows us to understand what fraction of the SNR we will recover for each waveform using that filter. The minimum FF is basically a measure of the sparsity of the template coverage. The maximum mismatch,

relative to the minimum FF, represents the maximum relative loss of SNR due to the parameter space discretization. For every approximant model considered for the template banks, sets of twenty thousands injections have been generated. The masses are drawn uniformly in component masses, spins are drawn uniformly in component spin magnitude and all the angular parameters are drawn isotropically.

Let's start with the banksim tests for the time domain banks. In the low mass region (table 4.1) there are four template banks, one with the AS approximant SEOBNRv4 (MM=0.97) and three with the PS approximant IMRPhenomTP, generated with three different minimal match thresholds (0.90, 0.93 and 0.95 respectivly). The FF distributions for each bank are plotted in figure 4.1. The simulated signals are $20k$ injections of the type IMRPhenomTPHM in plot a), IMRPhenomTP (in plot b) and SEOBNRv4 in plot c). The FF distributions of the PS banks (blue, green and red curves) in the plots a) and b) show that the PS banks perform better with respect to the AS bank (pink curve) in detecting precessing singnals, as expected. The pink curve shows a long tail of precessing signals detected with FF smaller than 0.97, i.e. smaller than the minimum FF used to produce the bank. This means that is lost more than 3% of SNR for those signals. Notice that in the case of AS injections in plot c) the PS banks are able to recover nearly signals with FF values near the threshold, which imply that the PS search performs as good as the AS search.

In the high mass region (table 4.2) there are three template banks, one with AS approximants SEOBNRv4 (MM=0.97), one with the PS approximant IMRPhenomTP (MM=0.90) and one with the PS approximant IMRPhenomTPHM (MM=0.90). Three banksim tests are performed, with $20k$ injections of the type IMRPhenomTPHM in plot a), IMRphenomTP in plot b), and SEOBNRv4 in plot c), showed in figure 4.2. In this case the performances of the banks are midly worst. However, the plots show that the FF distributions of the AS bank SEOBNRv4 (the green curve) has long tails of precessing signals recovered with values of the match much more lower than the PS banks (pink and blue curves), implying an higher loss in SNR with the AS search.

The banksim tests for the template banks in frequency domain show a similar trend. In the low masses region (table 4.3) there are four banks, two AS with the approximants SEOBNRv4ROM and IMRPhenomD (MM = 0.97 and MM = 0.90 respectively), and two PS with the approximant IMRPhenomPv2 (MM=0.90), one generated with an AS bank seed generated with the approximant IMRPhenomD, and the other one generated withoud the seed. The banksim tests are performed with $20k$ injections of the type IMRphenomPv2 shown in the plot a), and SEOBNRv4 shown in the plot c) , in figure 4.3. The AS bank recover most of the precessing injections with $FF < 0.90$, reducing the search sensitivity. Note that the seed is used for a more uniform coverage of the parameter space, and that's why the PS bank IMRPhenomPv2 generated with the AS seed has an higher number of templates with respect to the one without the seed. However, the performance of the bank (the blue curve) is as good as the one without the seed (the pink curve) and doesn't significantly improve the signal recovery fraction, for this reason it will be not used for further examinations.

In the high mass region (table 4.4) there are two banks, one AS with approximant SEOBNRv4ROM (MM=0.97) and one PS generated with the approximant IMRPhenomXPHM (MM=0.90). The banksim test with injection IMRPhenomXPHM (plot b) and SEOBNRv4ROM (plot d) in figure 4.3 show that the precessing bank recover a
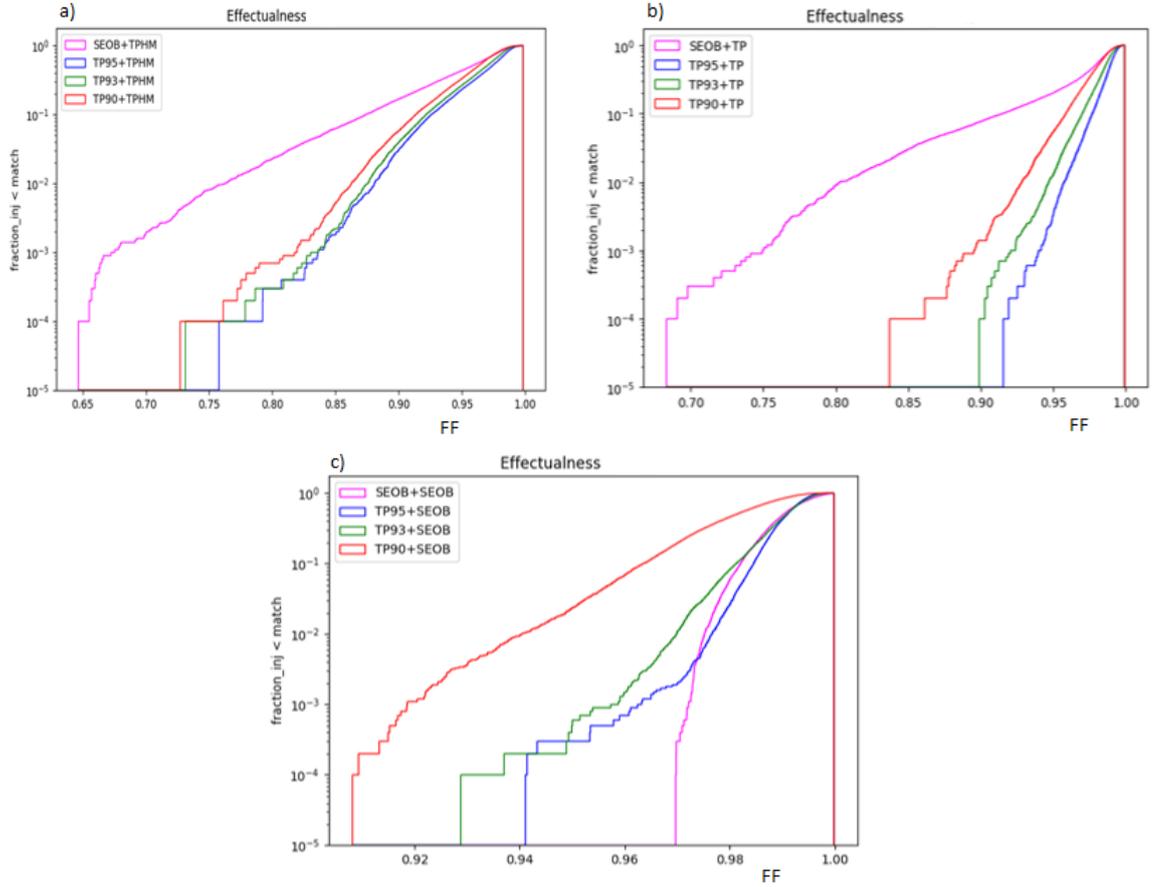
Figure 4.1: Cumulative distribution of fitting factors of the low mass template banks in time domain.

larger number of precessing injections with $FF > 0.90$ wrt the AS bank. In addition, in the case of AS injections the AS bank performs better, but the PS bank is able to recover injections with high values of the match which imply that there insn't a loss in the search.

Reasuming, we obtained that the majority of precessing injections are recovered with $FF < 0.90$, and then with a loss of SNR larger than 10% , if precession effects (and HOM) are neglected in the waveforms filters. When precessing template banks are used the tails of the fitting factors distributions are significantly reduced, which imply a gain in SNR recovery in the search. Plotting the signal recovery fraction (the detected injections with values of the match higher than the threshold) as function of the mass ratio and the precessing spin parameter χ_p we can see that for both time domain banks (in figure 4.4) and frequency domain banks (in figure 4.5) as the mass ratios of the systems become larger the signal recovery fraction can become as small as 0.65 when omitting precession and HOM, implying that ignoring these effects in a search would reduce the detection rate, especially for high mass systems.

Note that modelling the orbital angular momentum is relevant for the computation of the opening angle β. For the waveform models IMRPhenomXPHM/TPHM is used
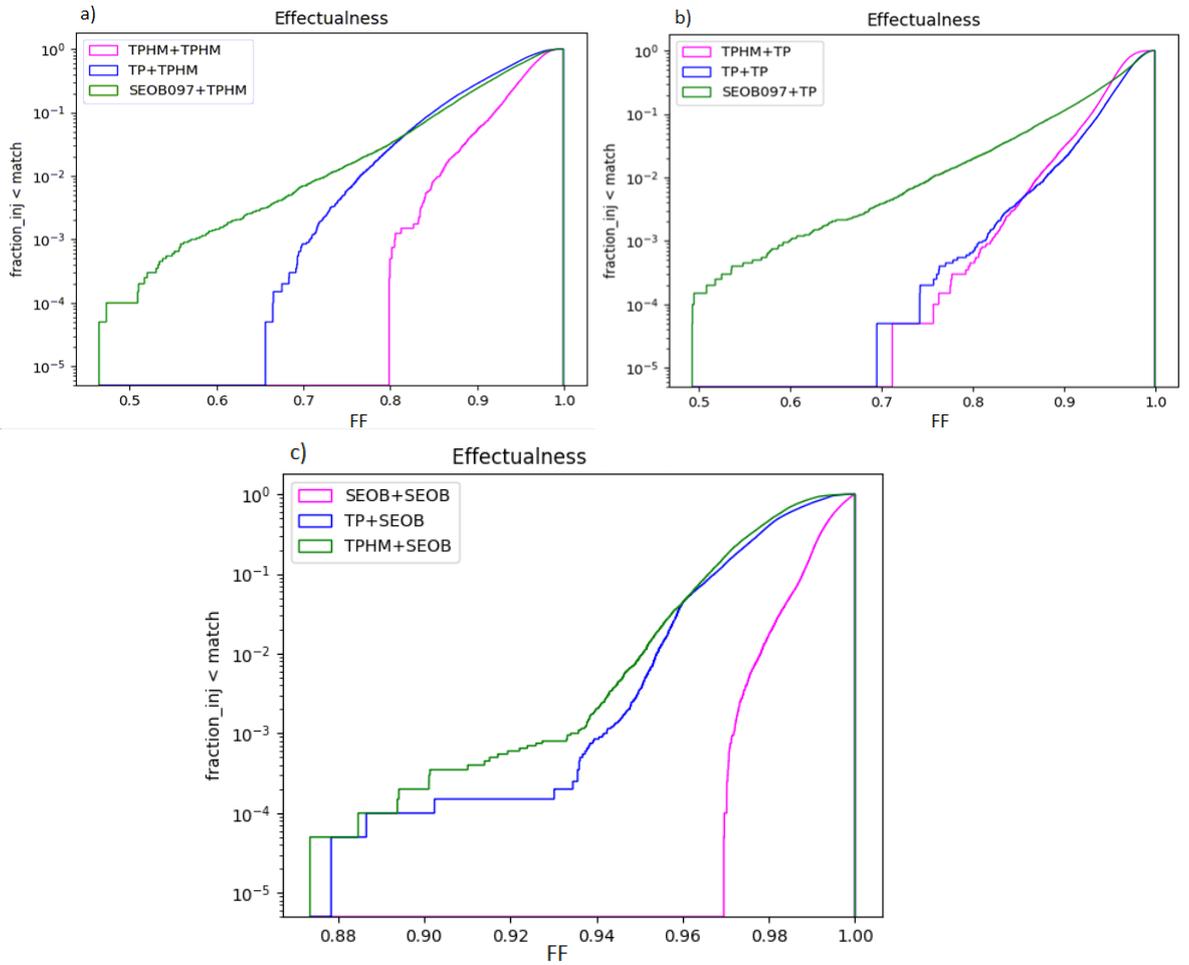
Figure 4.2: Cumulative distribution of fitting factors of the high mass template banks in time domain.
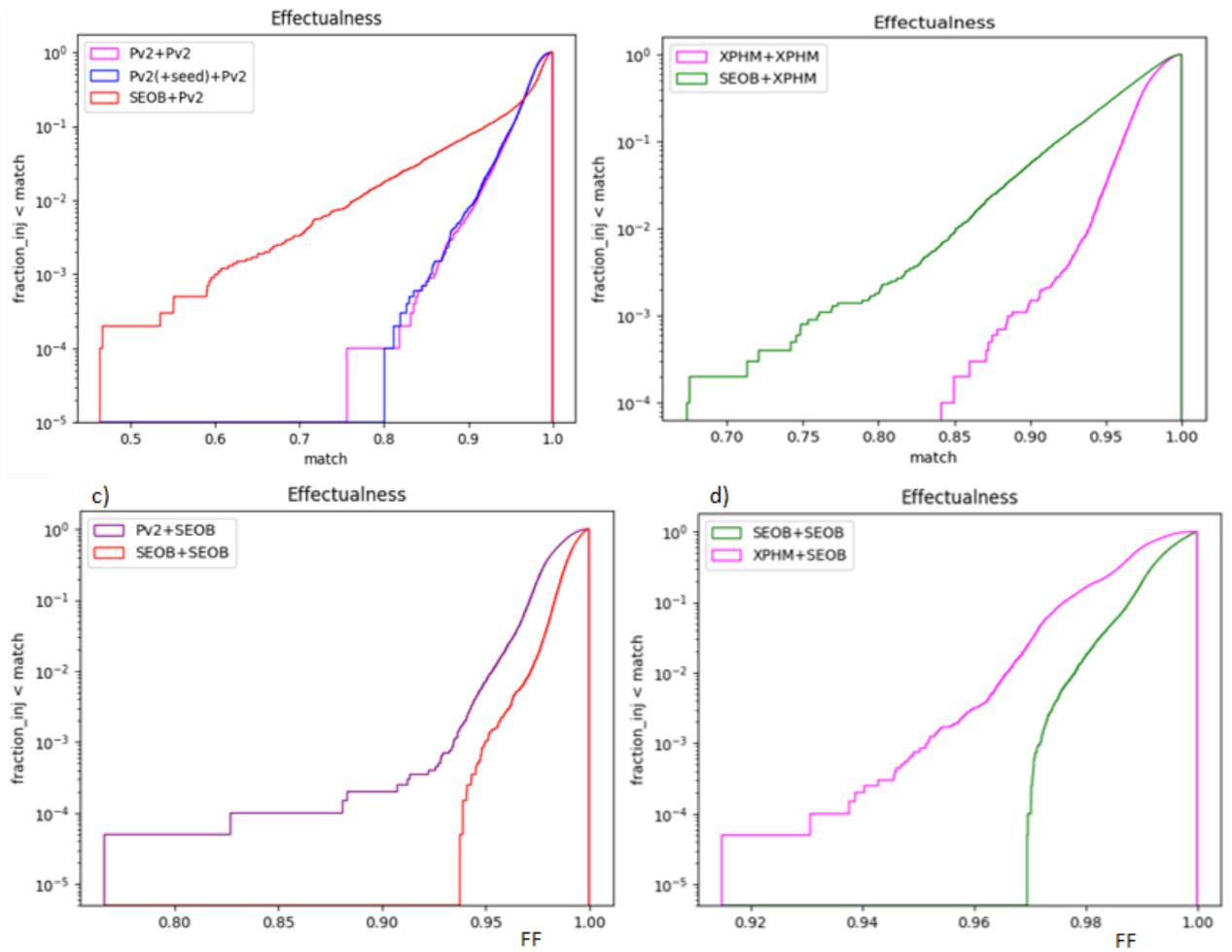
Figure 4.3: Cumulative distribution of fitting factors of the low mass (plots on the left) and high mass (plots on the right) template banks in frequency domain.
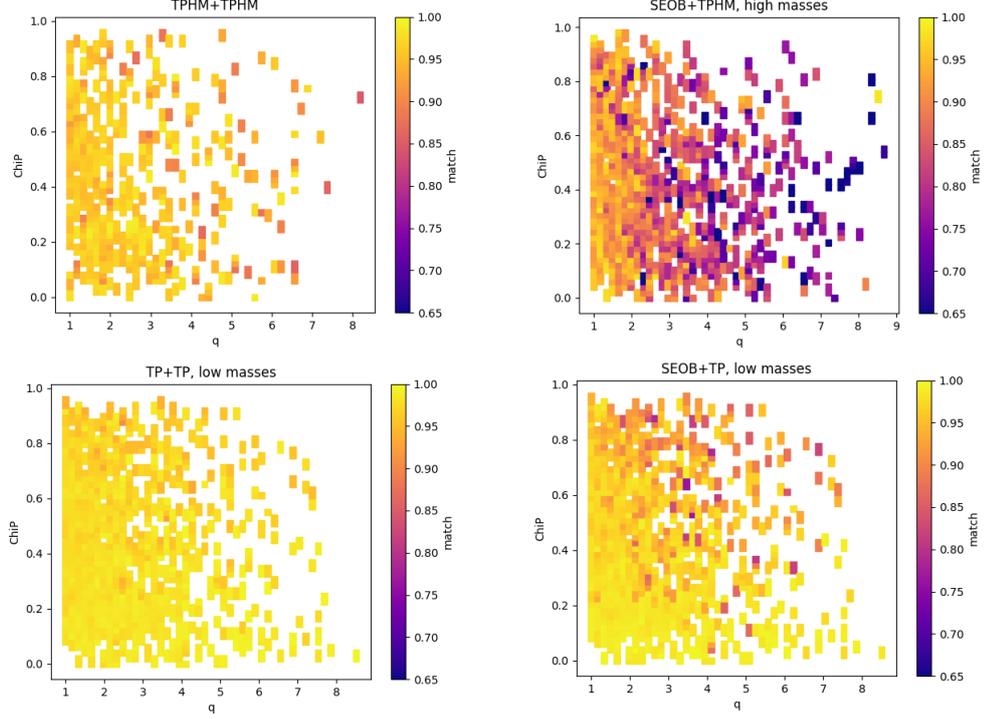
Figure 4.4: The signal recovery fraction plotted as function of mass ratio and precessing spin for Time Domain Template Banks.

the 4PN approximation (Ref. [70], [71]):

$$L_{4PN} = \frac{\eta}{\sqrt{x}} \left[L_0 + L_1\, x + L_2\, x^2 + L_3\, x^3 + L_4\, x^4 + L_{1.5}^{SO}\, x^{3/2} + L_{2.5}^{SO}\, x^{5/2} + L_{3.5}^{SO}\, x^{7/2} \right]$$

(4.22)

where $x = \left(\frac{G\, M_{tot}\, \pi\, f_{GW}}{c^3} \right)^{2/3}$, $\eta = m_1 \cdot m_2 / M_{tot}^2$ is the symmetric mass ratio, L_a are the orbital coefficient at a-PN order, L^{SO} are the spin-orbit contributions and we neglect spin-spin terms (the coefficients can be found in ref. [72],[73]). While for the waveform models IMRPhenomPv2 the 2PN approximation is used:

$$L_{2PN} = \frac{\eta}{\sqrt{x}} \left[1 + \left(\frac{2}{3} + \frac{\eta}{6} \right) x + \left(\frac{27}{8} - \frac{19\eta}{8} + \frac{\eta^2}{24} \right) x^2 \right]$$

(4.23)

4.5 Preliminary results and considerations

The results in the previous section demonstrate that when including precession effects in the waveform templates the search efficiency will increase. However, in a real search, the SNR threshold is a function of the number of templates which depends on the size of the parameter space. The precessing banks are roughly an order of magnitude larger than the corresponding aligned spin banks. This increase in the number of templates will increase the false alarm rate (background triggers generated by noise) of the search, and therfore a signal would require an higher SNR to be detected with the same confidence. In the next chapter we will assess the sensitivity of a precessing search with
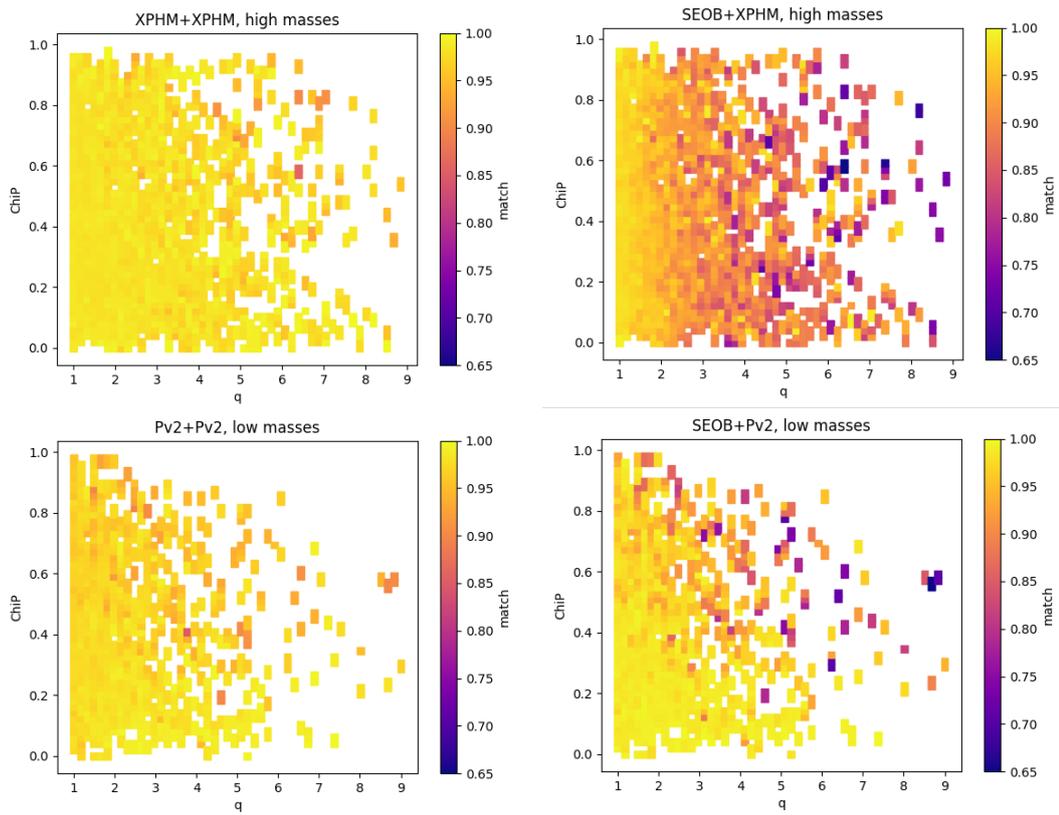
Figure 4.5: The signal recovery fraction plotted as function of the mass ratio and precessing spin for Frequency Domain Template Banks.
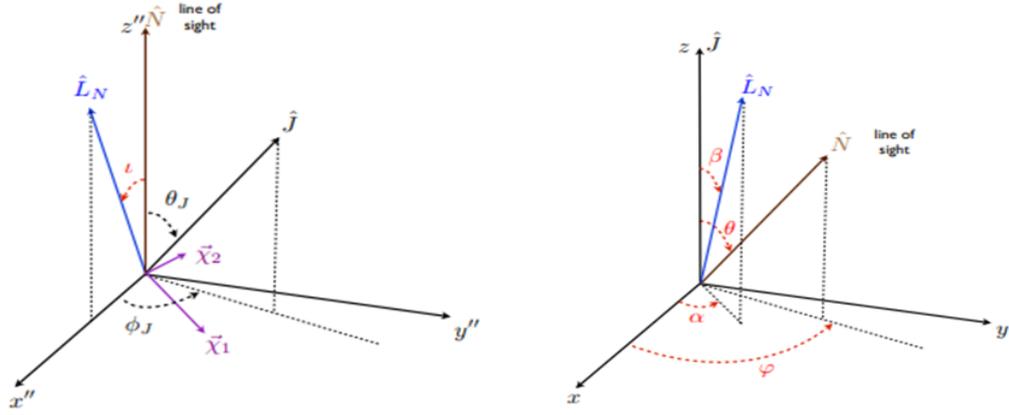
Figure 4.6: Illustration of N-frame on the left and J-frame on the right.

our precessing banks in Gaussian and real noise at a constant FAR. To identify, if any, "highly precessing" regions in the parameter space, two variables can be used: i) the opening angle $\vec{J} \cdot \vec{L} = L^2 + S_1 \cdot L + S_2 \cdot L = JL \cos \theta_{JL}$ which characterizes the intrinsic amount of precession in the system and ii) the inclination angle $\cos \theta_{JN}$ between J and the line of sight N which modulates how much precession an observer would see. Larger mass ratio implies more precessional cycles in the detector frequency bandwith, therby the increase in sensitivity of the precessing search as the mass ratio increase is an expected consequence of the fact that the magnitude of L decreases as the mass ratio increases, allowing larger opening angles of the precessing cone $\cos \theta_{JL}$. For the computation of the angles $\cos \theta_{JN}$ and $\cos \theta_{JL}$ it's necessary to apply a rotation of the spins from the co-coprecessing frame ($\vec{N}$-frame, plot on the left in figure 4.6) to the detector frame ($\vec{J}$-frame, plot on the right in figure 4.6) [74]. Then we plot $\cos \theta_{JN}$ and $\cos \theta_{JL}$ as function of the main match and show the plots for the frequency domain template banks in figure 4.7 and for time domain template banks in figure 4.8. If we compare the two searches, we can observe a lower number of injections but with higher values of the match in the left sides of the plots for the PS search wrt the AS search as expected.

In general the region where $(\cos \theta_{JL} \approx -1)$ is less populated because sources with $(\theta_{JL} \approx 180°)$ are considerate rare. Another reason is that for the simulatate signals used the mass ratio is always $q \leq 9$, accordingly θ_{JL} assume only a restricted number of values and the precessing cone is narrow.

4.6   IMRPhenomTPHM vs IMRPhenomXPHM

For the generation of the template banks in high mass region we used two approximants of the phenomenological models which include multipoles beyond the dominant quadrupole in the precessing frame: IMRPhenomTPHM [75] in time domain and IMRPhenomXPHM [72] in frequency domain. They are not the same waveform, for istance they do not include the same higher order modes: IMRPhenomTPHM includes (l, |m|) = (2,2)(2,1)(3,3)(4,4)(5,5), while IMRPhenomXPHM includes (l, |m|) =

Figure 4.7: Match plotted as a function of the orientation of the source and the precessing cone for frequency domain templates banks.
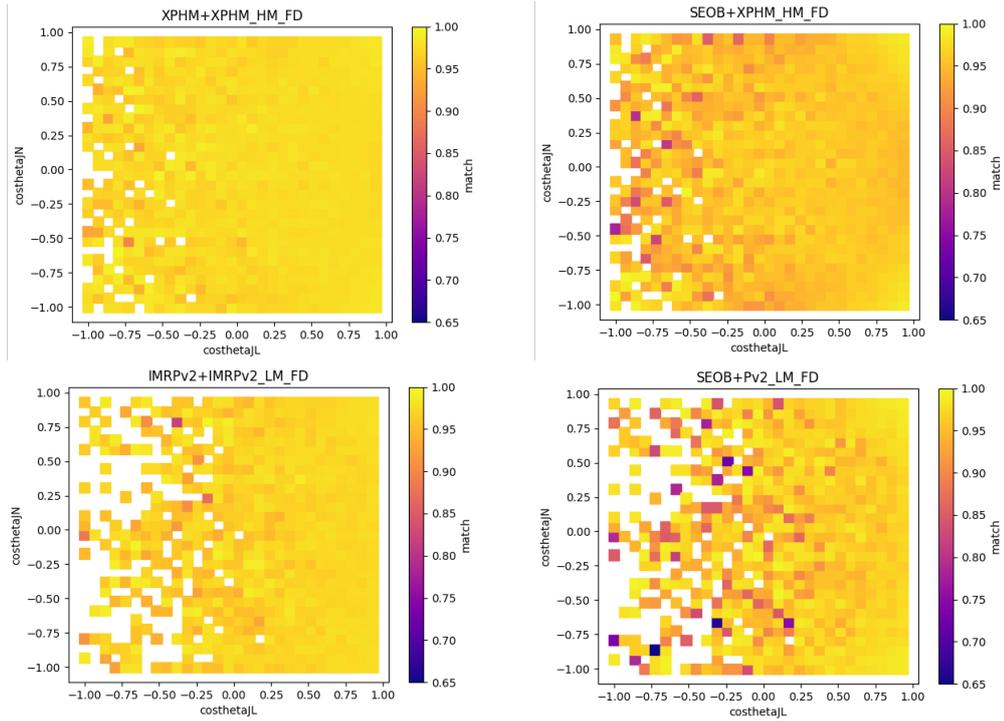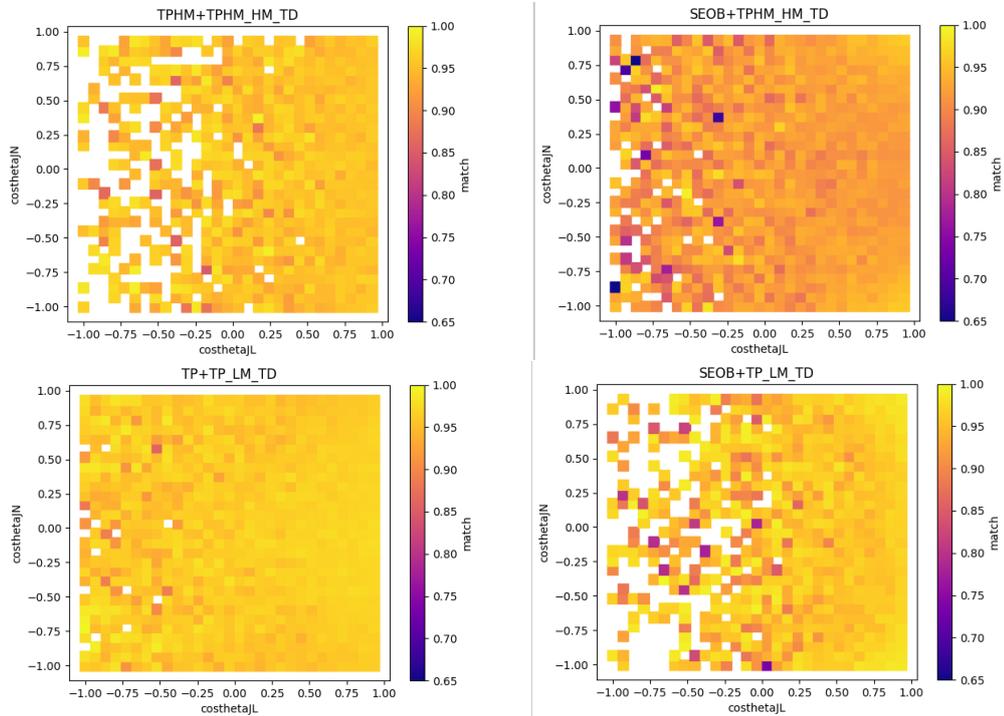

Figure 4.8: Match plotted as a function of the orientation of the source and the precessing cone for time domain templates banks.

(2,2)(2,1)(3,3)(3,2)(4,4). The templates banks obtained with them have a huge difference in the number of templates and in this section we want to point out similarities and differences between the two waveforms, althought the description of the technical details is beyond the purpose of this section. As shown in previous studies, a precessing waveform can be decomposed into the waveform as observed in a co-precessing frame and a time or frequency- dependent rotation that describes the precessional dynamics [76]. The rotation can be expressend in terms of three Euler angles (α, β, γ) between the two frames, then the relation between the modes can be expressed as:

$$h_{lm}^{P}(t) = D_{m,m'}^{l}(\alpha, \beta, \gamma) \, h_{lm'}^{CP}(t) \tag{4.24}$$

where $D_{m,m'}^{l}$ are the Wigner D-matrices. Both models are based on the so called twisting-up approximation [77], which maps non precessing signals to precessing ones in terms of a time dependent rotation described by three Eeuler angles, and both models inherit the implementation of the next-to-next-to leading order (NNLO) effective single-spin approximation and the double-spin multiscale analysis (MSA) approximation. The MSA system of equations is known to result in numerical instabilities when **S** and **L** are nearly misaligned. Such instabilities results in a failure of the waveform generation. In order to help alleviate these situations, for our template banks we opted to use the NNLO approximation implemented by default in LALSuite. For data analysis methods based on matched filtering it's particular convenient to use waveform model in frequency domain, because the noise in characterized in frequency domain and allow computationally efficient Bayesian inference analysis. However, the model constructed in the time domain allow several improvements: the inspiral description is more accurate thanks to the numerical integration of the post-Newtonian spin evolution; it's not used the stationary phase approximation, which is not suited for the merger and ringdown evolution of the GW signal. The merger is improved by employing a smoother approximation for the precessing Euler angles substituting in the uncertain plunge dynamic a simpler description from the MECO (minimum energy circular orbit) time to the coalescence time; finally in the ringdown a more consistent behaviour is ensured with BH perturbation theory by determining the Euler angles from the quasi-normal modes frequencies. For high mass systems like GW190521 ($\equiv 150 M_{\odot}$) with short-lived signal these shortcomings are not negligible, indeed the authors in [75] [78] show that the re-analysis of two high mass events GW190521 and GW170729 with IMRPhenomTPHM not only provide a better fit to the data than IMRPhenomXPHM, but also shows a much more consistent behaviour when varying the options for precession approximation and final spin, renforcing the idea that a time domain treatement in GW data analysis for high mass systems guarantees a cleaner separation between the ringdown and the inspiral-merger regimes (this is is not possible in the frequency domain due to the "smearing effect" of the Fourier transform).

For the further analysis proposed in this dissertation, we will use the template banks in time domain. The choise is motivated not only for the considerations aforementioned, but also by the necessity of the pipeline MBTA to have in input a time domain waveform model for the template banks.

"It has been said that astronomy
is a humbling and character-building experience.
There is perhaps no better demonstration
of the folly of human conceits
than this distant image of our tiny world.
To me, it underscores our responsibility
to deal more kindly with one another,
and to preserve and cherish the pale blue dot,
the only home we've ever known."
Carl Sagan, Pale blue dot: a vision of the human future in space

Chapter 5

Searching for Precessing Binary Black Holes Systems with MBTA

The multi-Band Template Analysis pipeline (MBTA) is a coincident, matched-filtering based analysis pipeline that can run in a low-latency online mode and, since recent years, in offline mode. It uses several banks of waveforms filters to cover the detectors bandwidth, i.e., the templates are split across multiple frequency bands to reduce the computational cost. It then constructs its background by making every possible coincidence from single detector triggers over a few hours of data. The pipeline also implements signal-based vetoes to reject instrumental transients. During O3 the MBTAOnline analysis contributed to trigger 42 low latency alerts with a median latency of 36 seconds. Among the latters, 34 had a False Alarm Rate below the alert threshold and 5 were retracted because of data quality analysis indicating a likely non-astrophysical origin. The non-retracted MBTA's GW candidates were confirmed by off-line searches. MBTA search did not assign a significance to single detector triggers, therefore during O3 submitted only coincidences to GraceDB (**Gra**vitational **C**andidate **E**vent **D**atab**a**se).

5.1 The Multi-Band Template Analysis pipeline

In order to perform a precessing search we need to understand the impact of signal-based vetoes that real GW searches employ. The goal of these vetoes is to discriminate between triggers produced by real GW signals and spurious triggers, which have instrumental and enviromental origin, known as glitches. The latters, commonly generate high SNR for matched filtering output, and it is possible to confuse them with GW triggers, primarily for very short signals of high mass systems. Correctly estimating the increase in sensitivity with a precessing search require to analyze the precessing banks in gaussian and in real noise and measure the efficiency in background at a constant False alarm rate (FAR). MBTA is one of the numerous search pipelines of the LIGO-Virgo Collaboration developed for GW data analysis. In particular, MBTA has been designed to run in low-latency, online mode, to search for signals involving neutron stars and black holes with the aim of rapidly identify GW candidate events suitable for electromagnetic follow-up observations with a latency of few seconds during the detectors data acquisition. However, in recent years MBTA has been optimized to run also in off-line mode, improving the noise rejection tools and consequently the detection

efficiency. The pipeline performs a coincident analysis, each detector in the network is analyzed separately before the results are combined (passing phase-amplitude and time coincidence tests) to identify coincident events, and it is able to do triggers clustering, false alarm rate estimation and trigger submission to GraceDB. It uses the IO feature of the Frame format and Virgo DAQ tools. For the description of the pipeline's archtecture the following references [Mbta User's guide] [79] [80] [81] [82] will be mainly used. The pipeline includes four main functions:

- **MbtaRT**: search for triggers in the data stream provided by a single interferometer. A threshold equal to 5 is commonly used. It's also able to do triggers clustering and work in combination with MbClustering;

- **MbCoinc**: search for the coincidence between triggers from different interferometers and estimate the significance of the candidates computing the FAR;

- **MbClustering**: the triggers provided by the previous coincidence steps are passed to this script to cluster in time the triggers;

- **MbAlert**: select potential triggers for EM follow-up. The candidate events must have passed some automated data quality checks, but they may later be retracted.

Both the on-line and off-line implementations of the pipeline run combining these applications together. In the offline version the main difference concern the adaptation to run on data with the addition of simulated signals and several optimizations for the detection efficiency. The update of the PSD is done on a longer period with respect to the online version, and the filtering step is run in two times, one in parallel on the full preeprocessed data and one with injections for data quality prescriptions. The FAR is estimated by using the full data taking period of interest and the relation between the FAR and the SNR is determined by the run without the injections. The latter is then used to associate a FAR to coincident triggers. In the next sections the main functions used by MBTA will be described in more detail.

5.1.1 Data pre-processing

Before processing the data through matched filtering, two pre-pocessing steps are applied: decimation and gating. The former re-samples the data at 4096 Hz after a suitable low-pass filtering in the frequency domain, the goal of the latter is to remove short stretches of bad data whatever a veto-flag is active (CAT1 for unknown issues, CAT2 for known instrumental or enviromental noises). The istantaneous sensitivity is assessed from the binary neutron stars range mentioned in section 2.1.3, computed from an estimate of a current PSD; the gating procedure is activated whenever the range value gets below a threshold. This method is potentially unsafe since it is based on a local estimate of the BNS range and gating could be triggered by loud astrophysical signals. The parameter space is split in 4 specific template bank regions, matching the BNS, NSBH, BBH and high mass BBH systems. To avoid to miss strong and short signals from high mass nearby BBH, the high mass part of the parameter space is analysed without applying the gating.

5.1.2   MBTA Run Time: Filtering the data

MBTA Run Time (MbtaRT) is the code that searches for GW candidate events in the detector data. It relies on the matched filter technique, as such the data are cross correlated with template banks describing a predicted signal for a certain parameter space. To generate the template waveforms MBTA uses the LSC Algorithm Library (LAL). The parameters (mass-spin) are organized in banks (template banks) and are generated in advance with the PyCBC's stochastic method Sbank, then the waveforms are loated in MBTA. The template bank is constructed using a reference noise power spectrum taken at a time when the detectors are performing well. The main characteristic of MBTA is that it splits the matched filter across two frequency bands, one called high frequency (HF), the other one called low frequency band (LF) used for low mass systems. This results in two benefits: i) the phase of the signal is tracked over fewer cycles, which means less templates are needed to cover the same parameter space and ii) a reduced sampling rate can be used for the lower frequency band, reducing the computational cost of the fast Fourier transforms involved in the filtering. The full band signal to-noise ratio (SNR) is then computed by coherently combining the matched filtering outputs from the two frequency bands:

$$S(t, M) = \int_{f_{min}}^{f_{max}} h(f)T(M, f)df = \int_{f_{min}}^{f_c} h(f)T_{LF}(M, f)df + \int_{f_c}^{f_{max}} h(f)T_{HF}(M, f)df$$

(5.1)

Where $h(f)$ is the detector signal in frequency domain, $T(M, f)$ is the filter generated in frequency domain with set of parameters M, f_{min} and f_{max} are the minimum and maximum frequency of the full band; f_c is the separation frequency which divides the two bands and is chosen with the criterion to obtain an SNR roughly equally shared between the two bands, depending on the detector and on the mass ratio of the estimated sources. As the MBTA analysis is divided over two frequency bands, it needs both a bank of templates covering the full frequency band called virtual templates (VT), and banks of templates used for matched filtering in the HF and LF bands respectively, called real templates (RT). VT are not used to filter the data but their parameters are associated to the triggers on the MbtaRT analysis output. The algorithm performs a coherent combination of the separated filter signals. Both the phase and quadrature matched filtering time series are computed for each band:

$$(h, T)_P(t) = 4 \int \frac{h(t)T^*(f)}{S_n(f)} e^{2i\pi ft} df$$

(5.2)

$$(h, T)_Q(t) = 4 \int \frac{h(t)T^*(f)}{S_n(f)} e^{2i\pi ft - \pi/2} df$$

These time series are translated and rotated to be aligned in time and phase, and coherently summed as follow:

$$(h, VT)_P(t) = (h, RT_{LF})_P(t) + (h, RT_{HF})_P(t + \delta t) \cos(\delta\phi) - (h, RT_{HF})_Q(t + \delta t) \sin(\delta\phi)$$

(5.3)

$$(h, VT)_Q(t) = (h, RT_{LF})_Q(t) + (h, RT_{HF})_P(t + \delta t) \sin(\delta\phi) + (h, RT_{HF})_Q(t + \delta t) \cos(\delta\phi)$$

The time and phase offsets δt and $\delta \phi$ correspond to the time it takes for the signal to chirp from the low frequency cut-off of the low frequency band to the low frequency cut-off of the high frequency band and its phase at that point, but in practice depend on the relationship between the virtual template and its associated real templates. Each VT is built in the time domain and matched filtered with its associated RT in each frequency band. This association is done by searching for the best match among real templates with parameters close to the corrsponding virtual template:

$$M(VT, RT) = max_{(t_c, \phi_0)} = \frac{(VT, RT)}{\sqrt{(VT, VT)(RT, RT)}} \tag{5.4}$$

and as usual $M = 1$ for the match of two identical signals. In figures 5.1 qnd 5.2 the signal recombination over the frequency bands and the output of the matched filtering are shown respectively. The matched filtering in LF band is performed at a down-sample rate shortening the FFT, to recombine the signal an up-sampling is done in time domain using a quadratic interpolation. The association among each VT and all the RT in each band is performed during the inizialitation phase and the RT with the highest match is chosen to be associated to the VT.
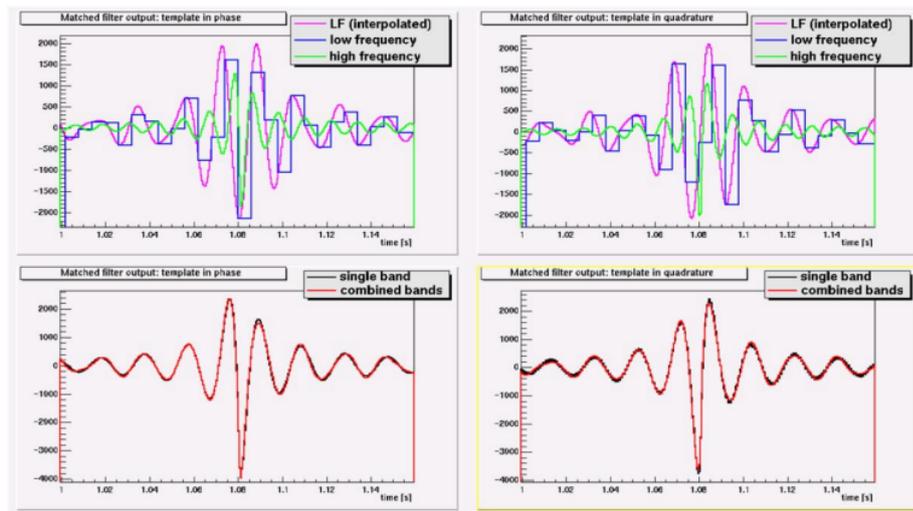
Figure 5.1: Example of matched filtering outputs of a pure signal without noise. Top plots: the raw low frequency band output (blue), the interpolated low frequency band output (purple) and the high frequency band output (green). Bottom plot: the usual single band matched filtered output compared to the recombined MBTA matched filter output. The left plots are for the template in phase, right for in quadrature.
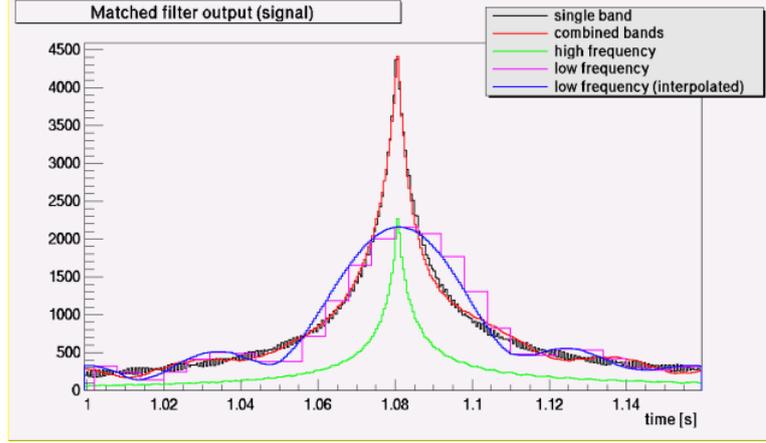
Figure 5.2: Signal output (quadratic some of the in-phase and quadrature outputs) for each band, the recombined signal (red) and the usual single band analysis (black).

5.1.3 SNR computation

In each frequency band the matched filter output is examined. The SNR time series $(\rho_i(t))$ for each frequency band is computed as follow:

$$SNR_i(t) = \frac{\sqrt{(h, RT_i)_P^2(t) + (h, RT_i)_Q^2(t)}}{(RT_i, RT_i)} \qquad i = 1, N_{bands} \qquad (5.5)$$

where RT_i is the real template associated with the VT on the band i. The total SNR of the full band will be:

$$SNR(t) = \frac{\sqrt{(h, VT)_P^2(t) + (h, VT)_Q^2(t)}}{(VT, VT)} \qquad (5.6)$$

For each VT the average fraction α_i of the SNR^2 expected in a band i is estimated as $\alpha_i = (RT_i, RT_i)/(VT, VT)$. The individual threshold for the frequency band i is computed as the global threshold multiplied by the square root of the fraction α_i. In figure 5.3. the sharing of SNR among the band is shown for a two bands analysis. The total SNR threshold is set to 5, in this case the SNR^2 is equally divided over the two band then $\alpha_1 = \alpha_2 = 1/2$ and the band threshold is $5/\sqrt{2}$. In figure is also shown that the SNR between the two bands is much more asymmetric if the triggers are produced by background noises than the one produced by simulated signals.
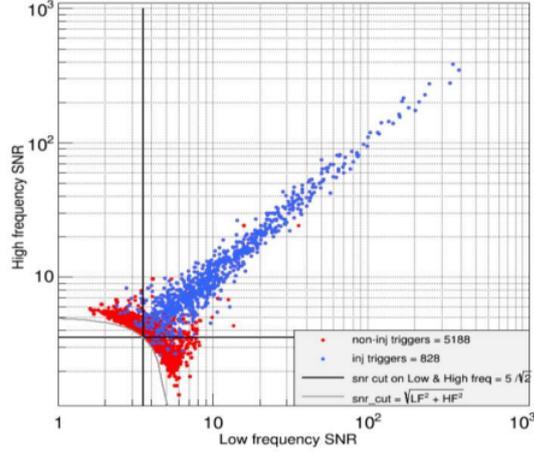
Figure 5.3: Example of SNR sharing between the low frequency and high frequency band for single detector triggers. The combined SNR cut was 5. The blue dots are for injections which usually have roughly the same SNR in each band, while for noise triggers (red dots), the SNR sharing between bands could be much more asymmetric.

5.1.4 The χ^2 test

For each unit stretch of processed data the single detector ranking statistic threshold ρ_{min} is selected, and a trigger is recorded if $\rho \geq \rho_{min}$. However, high energy matched filtering output can be driven by powerful glitches. To mitigate this problem a basic acceptance criterion is applied. For two frequency bands a 2-degree of freedom χ^2 observable is designed to compare the distribution of SNR between the two bands:

$$\chi^2 = \sum_{N_{bands}}^{i=1} [(h, RT_i)_P - (h, VT)_P \alpha_i \cos(\phi_0 + \delta\phi_{i-1})]^2 + \tag{5.7}$$
$$\sum_{N_{bands}}^{i=1} [(h, RT_i)_Q - (h, VT)_Q \alpha_i \sin(\phi_0 + \delta\phi_{i-1})]^2$$

where $\delta\phi_{i..(N_{bands}-1)}$ are the phase shifts of the signal at the frequency separation between the bands with $\delta\phi_0$. If we consider the signal as a sum of a waveform plus Gaussian noise, it can be shown that the equation 5.7 follows a χ^2-probability distribution with an expected value equal to $2(N_{bands} - 1)$. Due to the discretness of the parameter space (and approximations of post-Newtonian expansion), the match between the templates and the expected signal is not perfect and this make the 5.7 a non-central distribution with a non centrality parameter $B \cdot SNR^2$, where B depends on the mismatch and on the number of degree of freedom. In MBTA the cut on χ^2 is chosen such that:

$$\chi^2 < A(2 + B \cdot SNR^2) \tag{5.8}$$

A and B have been computed in an empirical way and set to 3 and 0.025 respectively. For more details on the SNR computation and consistency test see references [83] [84] [85] [86]. The output of the matched filter if the input signal matches perfectly a template is a narrow peak. However, the simulated signals are only an approximation of the

expected GW signature, then the filter output will be broader but still gathered around the peak. In case of triggers produced by glitches the outpus is expected to present a much wider distribution and multiple maximums. This trend can be used to better discriminate signals from glitches.

During the observing run O3 another approach was adopted which is a variant of the autocorrelation-based least-squares test described in [87], a reweighted SNR ρ_{rw} is defined:

$$\rho_{rw} = \begin{cases} \rho_{rw} = \rho & \xi_{PQ}^2 \leq 1 \\ \rho_{rw} = \rho \left(\frac{A + (\xi_{PQ}^2)^\alpha}{A+1} \right)^{-1/\beta} & \xi_{PQ}^2 > 1 \end{cases} \qquad (5.9)$$

with ξ_{PQ}^2 a discretized version of:

$$\xi_{PQ}^2 = \frac{1}{2\Delta t} \int_{t_0 - \Delta t/2}^{t_0 + \Delta t/2} | \begin{pmatrix} \rho_P(\text{t}) \\ \rho_Q(\text{t}) \end{pmatrix} - \rho R(\phi) \begin{pmatrix} A_P(\text{t-t}_0) \\ A_Q(\text{t-t}_0) \end{pmatrix} |^2 dt \qquad (5.10)$$

where ρ and ϕ are the modulus and phase of the complex SNR of the trigger recorded at time t_0, $\mathcal{R}$ is the rotation matrix associated to ϕ, ρ_P and ρ_Q are the matched filter outputs with the in-phase and in-quadrature templates respectively, A_P and A_Q are the autocorrelations of the templates with its in-phase and in-quadrature avatars, with normalized maximum at $t = t_0$. Parameters are empirically chosen $A = 10$, $\alpha = 5$, $\beta = 8$. The glitches can still produce loud triggers which survive to all the applied cuts and vetoes, however when detectors show evidence for poor data quality another quantity E_R is computed, sensitive to an excess in the rate of triggers survived once the χ^2 cut is applied and the ρ_{rw} is considered. In order to penalize those noise triggers a new ranking statistic is defined that takes into account E_R:

$$\rho_{rw,E_R} = \begin{cases} \rho_{rw,E_R} = \rho_{rw} & E_R \leq 0.3 \\ \rho_{rw,E_R} = \rho_{rw}[1 - A(E_R - 0.3)^\alpha] & E_R > 0.3 \end{cases} \qquad (5.11)$$

where $A = 1$ and $\alpha = 2$. Note that the statistic ρ_{rw,E_R} is not applied in Gaussian noise analysis.

5.1.5 Coincidences

Single detector triggers that pass the χ^2 test are checked for coincidences across detectors by the MbCoinc process. Candidate events are defined as time coincidences between single detectors triggers found with the same template, if exact match is asked, or triggers from two detectors if their time and mass parameters match within expected uncertainties. The time coincidence criterion applied is to allow the maximum time delays (since GWs travels at speed of light) $\Delta t_{HL} = 15\ ms$ and $\Delta t_{H1V1} = \Delta t_{L1V1} = 40\ ms$, accounting for both the time of flight of the signal from one detector to another and for the experimental uncertainty in the arrival time measurement. MBTA can also find triple detector coincidences, identified as a pair of H1L1 and H1V1 coincidences sharing the same H1 trigger. Searching for triggers from multiple detectors not only significantly reduces the background noise, but also provides information to improve the accuracy of the sky localization reconstruction of the GW sources. Triggers generated by astrophysical events are expected to show correlations across detectors not only between the

arrival times but also the phase and amplitude of the signal. With the time differences, phase differences, and relative amplitudes of the detectors (labeled as i,j,k) are built the probabilities $P_{\Delta t_{ij}}, P_{\Delta \phi_{ij}}, P_{RA_{ij}}$ which quantify how likely the measured parameters are for a population of sources and are added into the quadratic sum of the individual ranking statistics when computing the combined ranking statistic for double or triple coincidences:

$$\rho^2_{RS,ij} = \rho^2_{rw,E_R,i} + \rho^2_{rw,E_R,j} + 2\ln(P_{\Delta t_{ij}} P_{\Delta \phi_{ij}} P_{RA_{ij}}) \tag{5.12}$$
$$\rho^2_{RS,ijk} = \rho^2_{RS,ij} + \rho^2_{RS,ik} - \rho^2_{rw,E_R i}$$

5.1.6 Clustering the triggers

Finally, a clustering across the template banks is performed to group coincidences that are close in time and therefore likely to originate from the same event. A single event (a noise trigger or a real GW signal) can be strong enough to involve more than one template, hence most of the triggers produced by the matched filtering separated in time less than a minimum gap are gathered in time clusters by the algorithm MbClustering, applied after the coincidence search step. The clustering algorithm is based only on the trigger timing, running all over the parameters space, independently of the masses or spin values of the triggers. The clustering procedure reduces the number of candidates, making each of them more significant. For each cluster of triggers only the event with the highest ranking statistic is chosen and significant triggers can be submitted to GraceDB by the MbAlert process.

5.1.7 False alarms rate estimation

Coincidences are assesed by determining their false alarm rate (FAR), i.e. the rate of coincidences from noise triggers with ranking statistics as high or higher than that of the considered concidence. The FAR computation is done by assuming that the detectors are independent, producing uncorrelated triggers with stationary trigger rates. A sample of single detectors triggers is built using the last 24 hours of data for the online search and about 6 days for the offline runs. It's computation require two main steps: the first one is to determine an initial FAR for each single search (a given region and a given type of double or triple coincidence) by building a background model using random coincidences of single detectors triggers; the second step is to account for these multiple searches running in parallel, to provide the final FAR relative to the overall coincidence time by adding to the previously computed FAR trial factors. Starting with single detectors triggers, which are largely dominated by noise, fake coincidences are built by making all possible combinations with identical template from different detectors. To get the cRS for a fake coincidence the parameter consistency checks are applied using the single trigger parameters for the phase and amplitude and a random value, within the allowed range, for the time of flight. Then, the FAR for double coincidences with a given cRS is computed by multiplying the single detector trigger rates by the probability to have random fake coincidences with that cRS. If we define the single detector trigger rate R_i, measured as the ratio of the number of triggers above a chosen threshold over the time period of the search $R = \frac{N_i}{T_i}$, then the probabilities of random coincidences

between two (double coincidence rate) and three detectors (triple coincidence rate) are $R_{ij} = R_i R_j dt_{ij}$ and $R_{ijk} = R_i R_j dt_{ij} R_k dt_{ik}$ respectively, where dt_{ij} is the time window allowed for the coincidences. These probabilities must be multiplied with the factors $\frac{M_{ij}}{N_i \cdot N_j}$ for double coincidences and $\frac{M_{ij}}{N_i \cdot N_j \cdot N_k}$ for triples coincidences, where M_{ij} is the number of pairs having at least the given cRS, and $N_i N_j$ is the combinations of triggers independently of their arrival time but coming from the same template. The FAR can be computed as:

$$FAR_{double} = R_{ij} \frac{M_{ij}}{N_i N_j} = \frac{M_{ij} dt_{ij}}{T_i T_j} \qquad (5.13)$$

$$FAR_{triples} = R_{ijk} \frac{M_{ij}}{N_i N_j N_k} = \frac{M_{ij} dt_{ij} dt_{ik}}{T_i T_j T_k}$$

The larger are the time intervals the lower will be the minimum estimable FAR. This FAR estimation is local and enlarging the time intervals the computation start to be less local but more accurate. Within a region HL, HV, LV and HLV events are not always possible, due to insensitive orientation of the antenna patterns of the detectors. To account for this effect the value of the FAR is divided by trial factors κ_{coinc} that capture the relative searched volume of each type of coincidence. They are estimated using an astrophysical source population simulation and counting the number of sources expected to be detected as different coincidence types. The typical values used for κ_{coinc} are 0.909 , 0.002 , 0.007 for HL, HV, LV, and 0.083 for HLV respectively. For the searches running on the three regions BNS, BBH and NSBH a trial factor $\kappa_{region} = 1/3$ is applied. The fourth region that looks for high mass BBH events is ignored since it produces only very significant events, given its higher threshold. The inverse false alarm rate (IFAR) of a cluster is computed from the FAR for the particular type of coincidence in a specific region, according to:

$$IFAR = \frac{\kappa_{region} \, \kappa_{coinc}}{\kappa_{cluster} \, FAR(\rho_{RS})} \qquad (5.14)$$

where the FAR obtained before clustering is scaled by the factor $\kappa_{cluster}$ equal to the average number of clustered events divided by the number of events before clustering. This factor was estimated to be 0.59 for BNS and 0.44 for BBH and NSBH for the online configuration. True astrophysical events are expected to have high values of the IFAR.

5.2 A search for BBH with precessing-spins

In this chapter we will study the effect of introducing templates banks with waveforms including precession (and higher order modes) in a real GW search, simulating a search running Monte Carlo tests with the MBTA pipeline. The performances comparison between a search for detecting BBH simulated signals with aligned-spin (AS) and precessing-spin (PS) tempate banks is the content of this chapter. The target sources are divided in two parameters space as discussed in the last chapter. In particular, the high mass region with $M_{tot} = [100 - 500] M_\odot$ will be analized with the PS bank IMRPhenomTPHM including 4423 templates and the AS bank SEOBNRv4 including 146
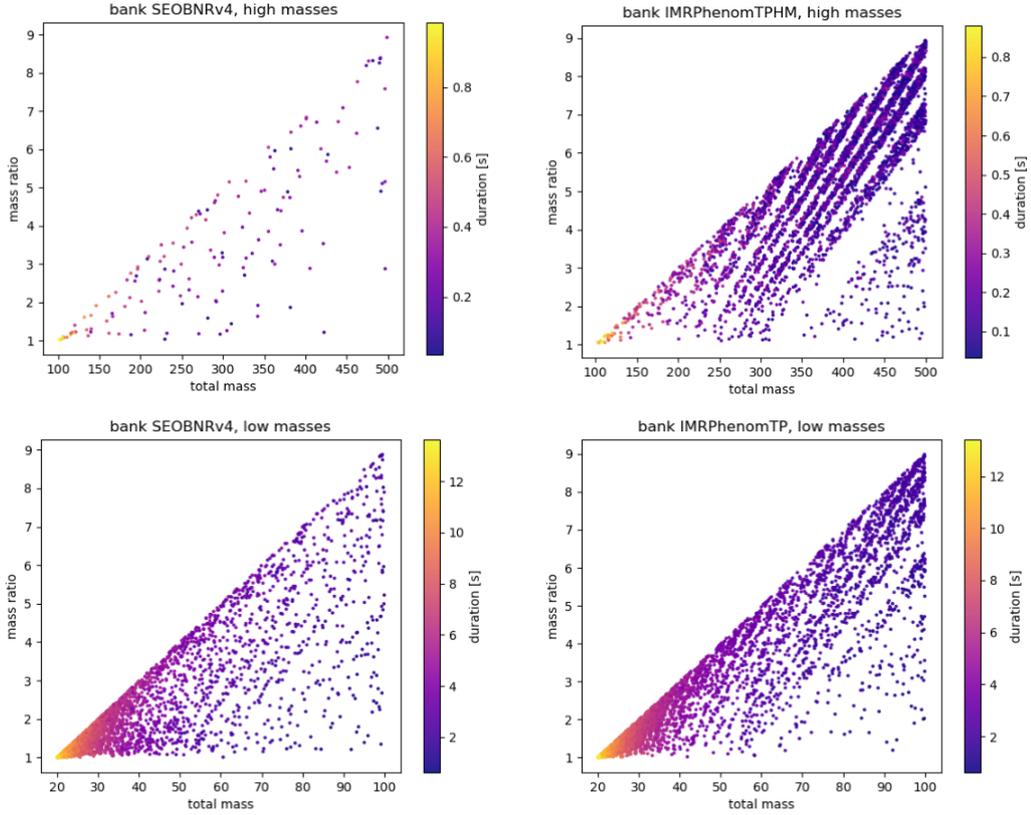
Figure 5.4: Template banks with the total mass versus mass ratio as function of the duration in seconds of the waveforms. Top panel high mass templates banks in time domain, bottom panel low mass template banks in time domain.

templates. It can be noticed that the PS bank contains more templates than the AS bank, this means that the growth in efficiency expected using a PS bank has to deal with a larger number of false alarms. The low mass region with $M_{tot} = [20 - 100]M_\odot$ will be analized with the PS bank IMRPhenomTP with 4492 templates and the AS bank SEOB-NRv4 with 3798 templates. In figure 5.4 are shown the template banks plots with the total mass versus mass ratio as function of the duration in seconds of the waveforms. The injection sets parameters used for the simulations are listed in the table below. Each set contains $10k$ waveforms generated with the approximant IMRPhenomTPHM with a low frequency cut-off of $15\ Hz$, uniform distributions in masses and distance $(200\ Mpc - 2\ Gpc)$ and spin magnitude up to $|0.99|$. In figure 5.5 are shown the chirp mass and the total mass distributions versus the mass ratio plots for the low mass and high mass injections. To obtain statistically significant results analyzing short period of data, the injections are separated at an interval of about $15\ s$.
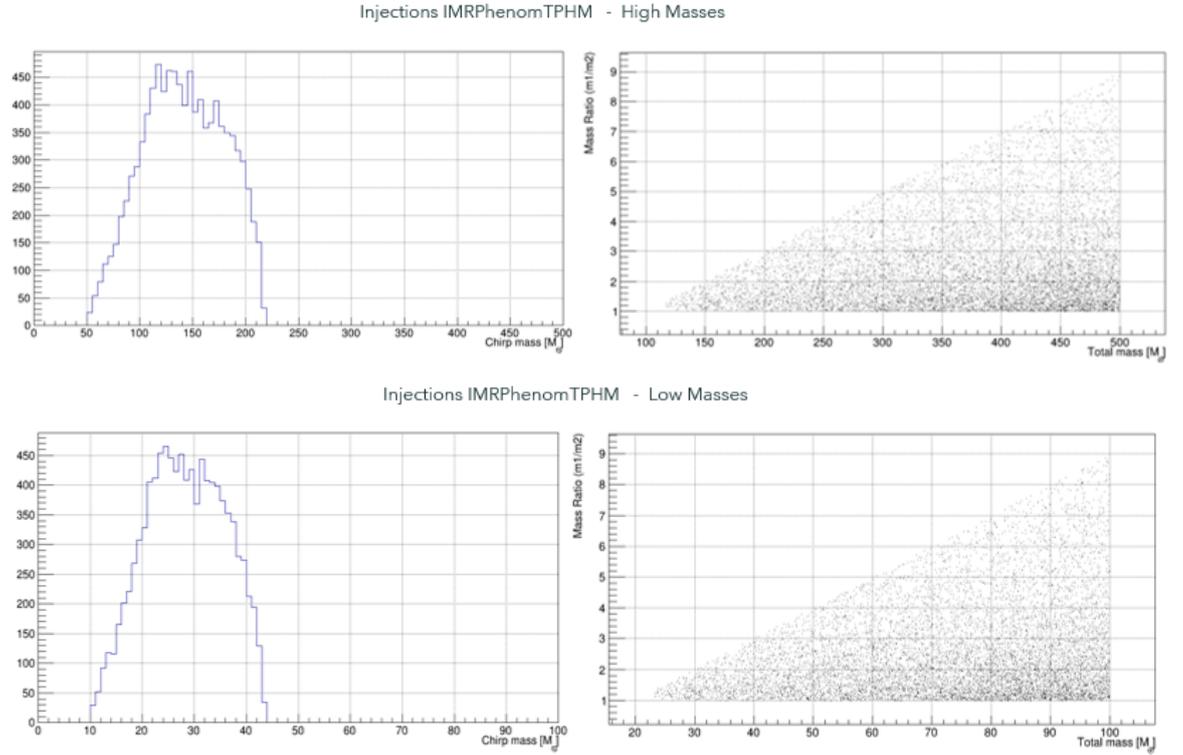
Figure 5.5: Chirp mass and total mass distributions versus the mass ratio plots for the high mass (top panel) and low mass injections (bottom panel).

Simulated population parameters	distributions
Spin magnitude $\lvert \chi_i \rvert$	$(0, 0.99)$
Cosine of sky location (polar) $cos\theta$	$(-1, 1)$
Cosine of inclination $cos\iota$	$(0, 1)$
Polarization angle Ψ	$(0, 2\pi)$
Sky location (azimuth) ϕ	$(0, 2\pi)$
Distance D	$200\ Mpc - 2\ Gpc$

Table 5.1: Injections properties.

In the next sections we will analyze the results for searching single detectors triggers in Gaussian noise, double detectors coincidences in Gaussian noise and double detectors coincidences in a chunk of O3 data. This analysis considers only LIGO Hanford (H) and Livingstone (L) detectors and only one-band MBTA search have been performed. The pipeline's version used for the simulations is v5r27.

5.2.1 Monte Carlo test running MBTA

When a run is submitted, the configuration file contains all the components needed for the analysis:

- the input data chunk with the dector noise that have to be analyzed (gaussian noise or real data);

- the injections data file;

- the templates bank data file;

When the run is finished all the output files with filtered data which refers to the same time chunk and the same injection set are merged into one file containing the triggers found in time coincidence for H1 and L1 detectors. In the next sections, for comparing the results of the two analysis (aligned-spin and precessing-spin) three main aspects will be taken into account: the efficiency of the search, that is the number of injections found with a proposed cut in FAR; the gain in the combined ranking statistic of the recovered injections; and the performance in terms of the Inverse FAR (IFAR), i.e. the significance associated to the coincident events found by MBTA.

5.2.2 Single detector triggers in Gaussian Noise

A preliminary Monte Carlo test has been performed searching for single detector (L) triggers. The first step is to run the template banks in Gaussian noise without injections for the computation of the FAR associated to the noise triggers events. The period of time analyzed is $T = 210.000\ s$ and the minimum FAR reached is $2.5 \cdot 10^{-6}\ Hz$ (therby the maximum IFAR is $10^6\ s$). The trigger rates, i.e. the number of events over the time analized $TR = \frac{N_{ev}}{T}$ for high mass banks and low mass template banks are reported in tables 5.1 and 5.2 respectively. From the plots of the FAR in figure 5.6 we can observe that the trigger rates are higher for the PS banks as expected, since an higher number of templates pick-up extra noise. After the FAR compitation step, the templates banks are analized in Gaussian noise adding the set of ten thousands injections. Events in the data file are searched in a time window of 1 s around the gps time of an injection. Plotting the IFAR of the detected injections in figure 5.7 it is possible to observe that the performances of the two search PS and AS are comparable, i.e. the PS and AS banks recover the same number of precessing injections for various cut in FAR and censequently there is no gain in the efficiency in both high mass and low mass regions of the parameters space. Investigating on the sets of low mass and high injections used for the tests, it was found that most of them have low values of the precessing parameter χ_p and therfore with weak precession, for this reason new injections have been generated with higher values of the χ_p (see figure 5.8) which will be used in the coincidence tests described in the next sections.
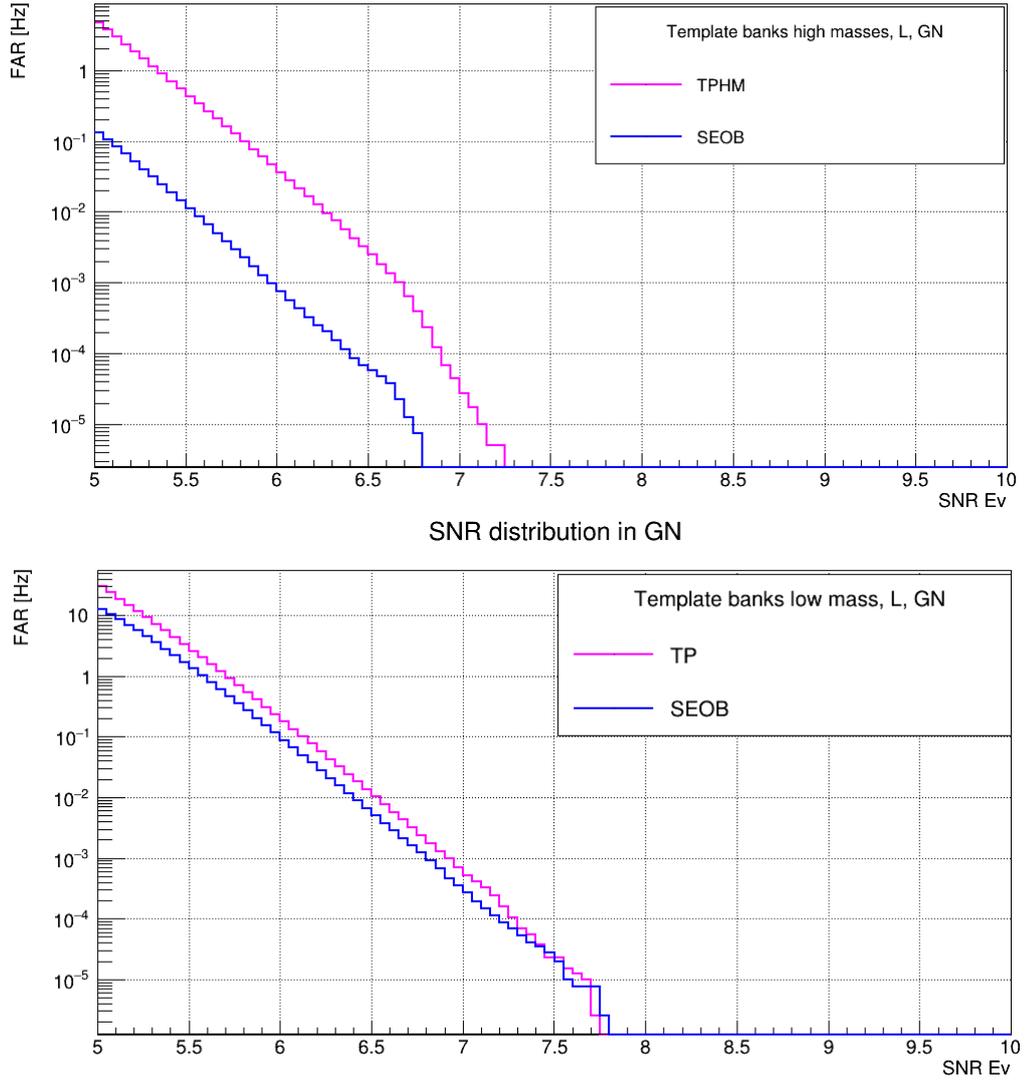
Figure 5.6: FAR of the single noise-triggers for high mass (top panel) and low mass (bottom panel) template banks in Gaussian noise.

High mass banks	FAR [Hz]	Trigger rate
IMRPhenomTPHM (4423)	$5\ Hz$	1 Ev $\sim 0.2\ s$
SEOBNRv4 (146)	$1,5 \cdot 10^{-1}\ Hz$	1 Ev $\sim 6.6\ s$

Table 5.2: Single detector (L) trigger rates for high mass templates banks in Gaussian noise.

Low mass banks	FAR [Hz]	Trigger rate
IMRPhenomTP (4882)	$30\ Hz$	1 Ev $\sim 0.03\ s$
SEOBNRv4 (3798)	$15\ Hz$	1 Ev $\sim 0.07\ s$

Table 5.3: Single detector (L) trigger rates for low mass templates banks in Gaussian noise.
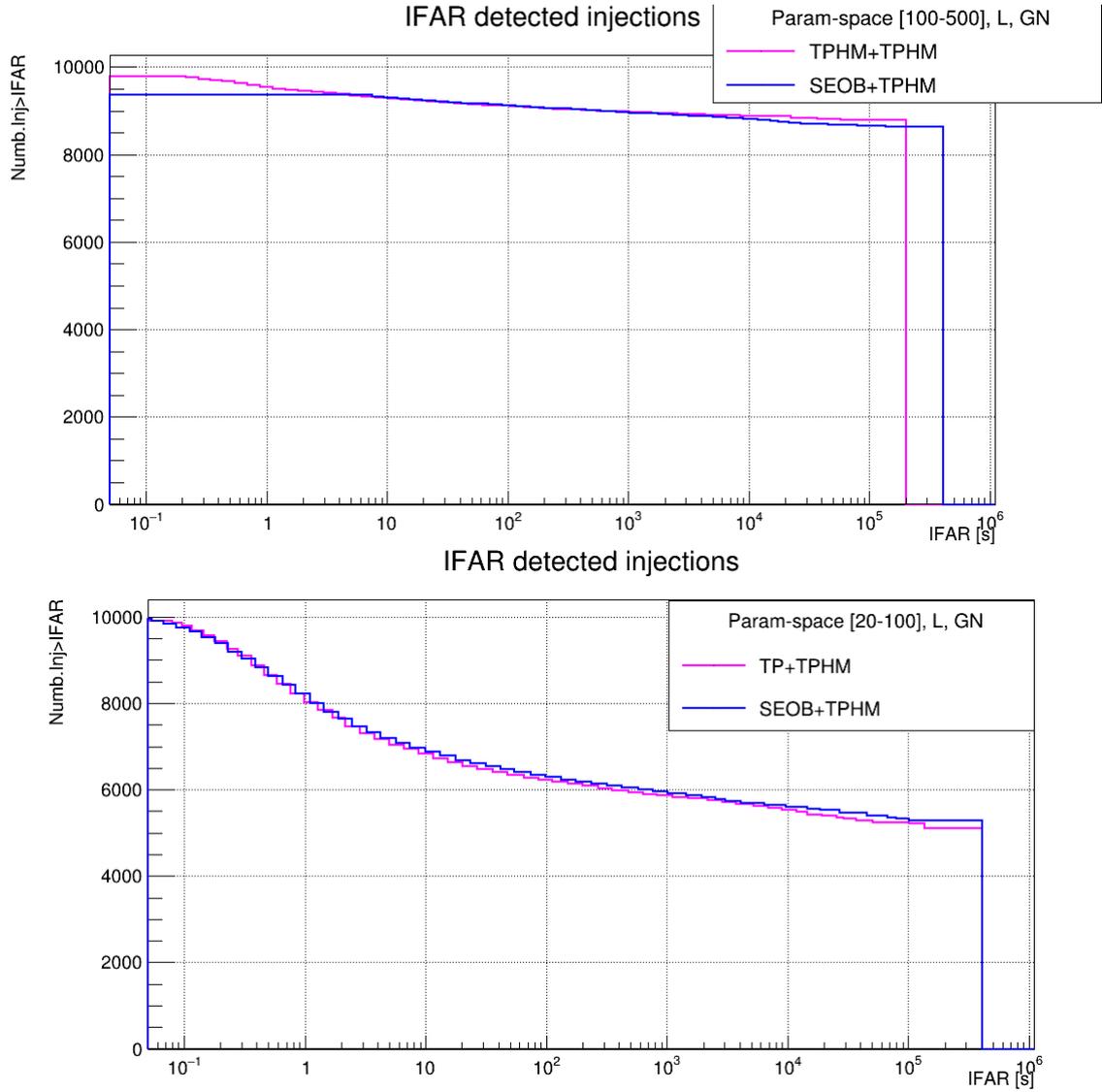
Figure 5.7: IFAR of the detected injections for high mass (top panel) and low mass (bottom panel) template banks in Gaussian noise.
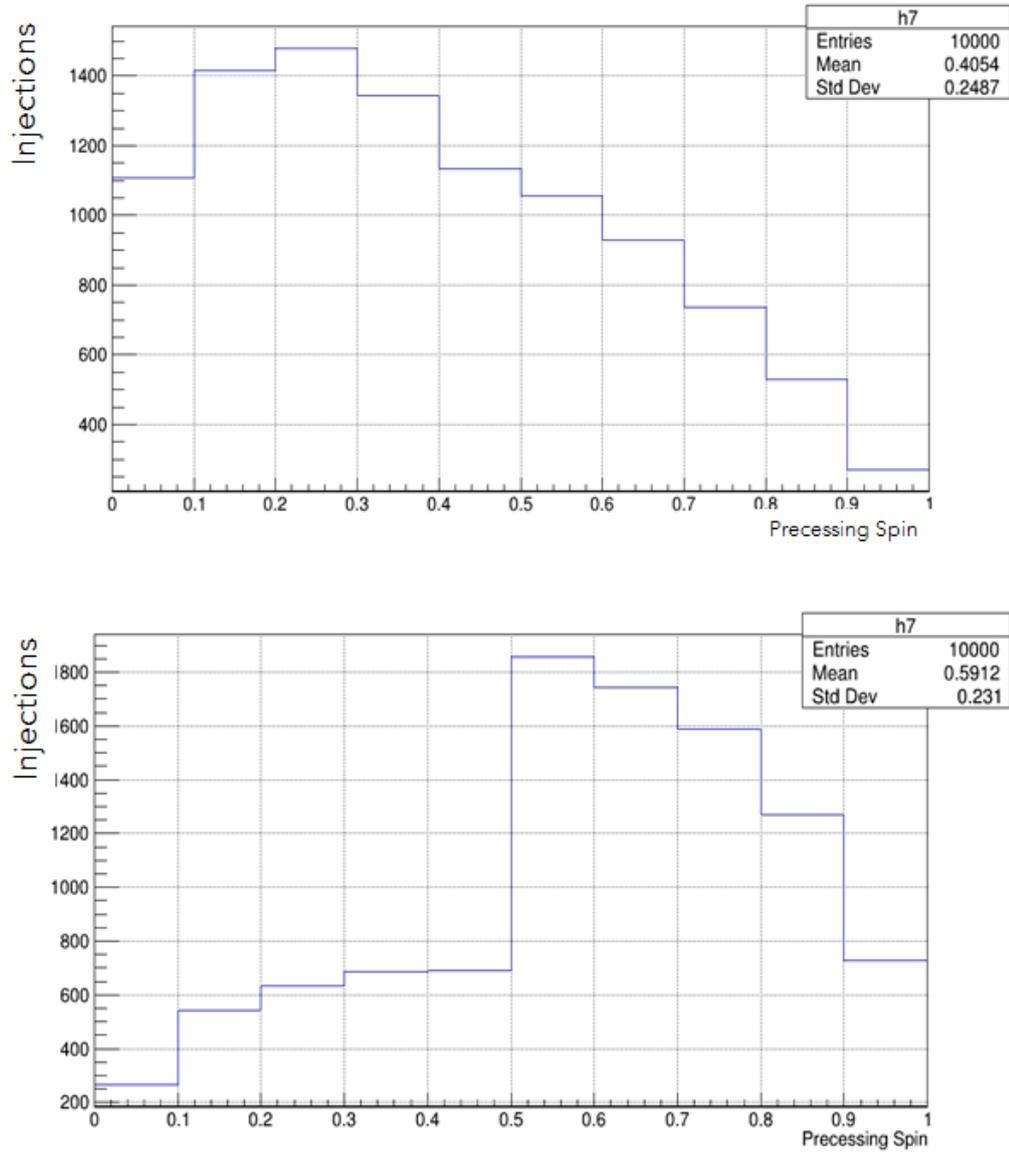
Figure 5.8: Distributions of the precessing spin parameter ($0 < \chi_p < 1$) of the low precessing injections (top panel) and high precessing injections (bottom panel) respectively.

5.2.3 Coincident detectors triggers in Gaussian Noise

The first step is to run MBTA with template banks in Gaussian noise without injections for the computation of the FAR for the noise events. For two detectors (HL) coincidences the period of time analyzed is again $T = 210.000 \ s$ and the minimum FAR reached is about $10^{-13} \ Hz$ (computed with the formula for FAR_{double} in eq. 5.13). A cut in $FAR < 10^{-7} \ Hz$ for the comparison of the detected injections from the two analysis is chosen, which is a common threshold used to send out significant GW alerts for CBC sources. The plots of the FAR in figures 5.9 and 5.10 show again that the precessing banks trigger more noise events because they have more templates, however

the SNR of the events are not higher than 10 (a different trend will be shown for noise events in real data in the next section). In tables 5.3 and 5.4 are reported the trigger rates.
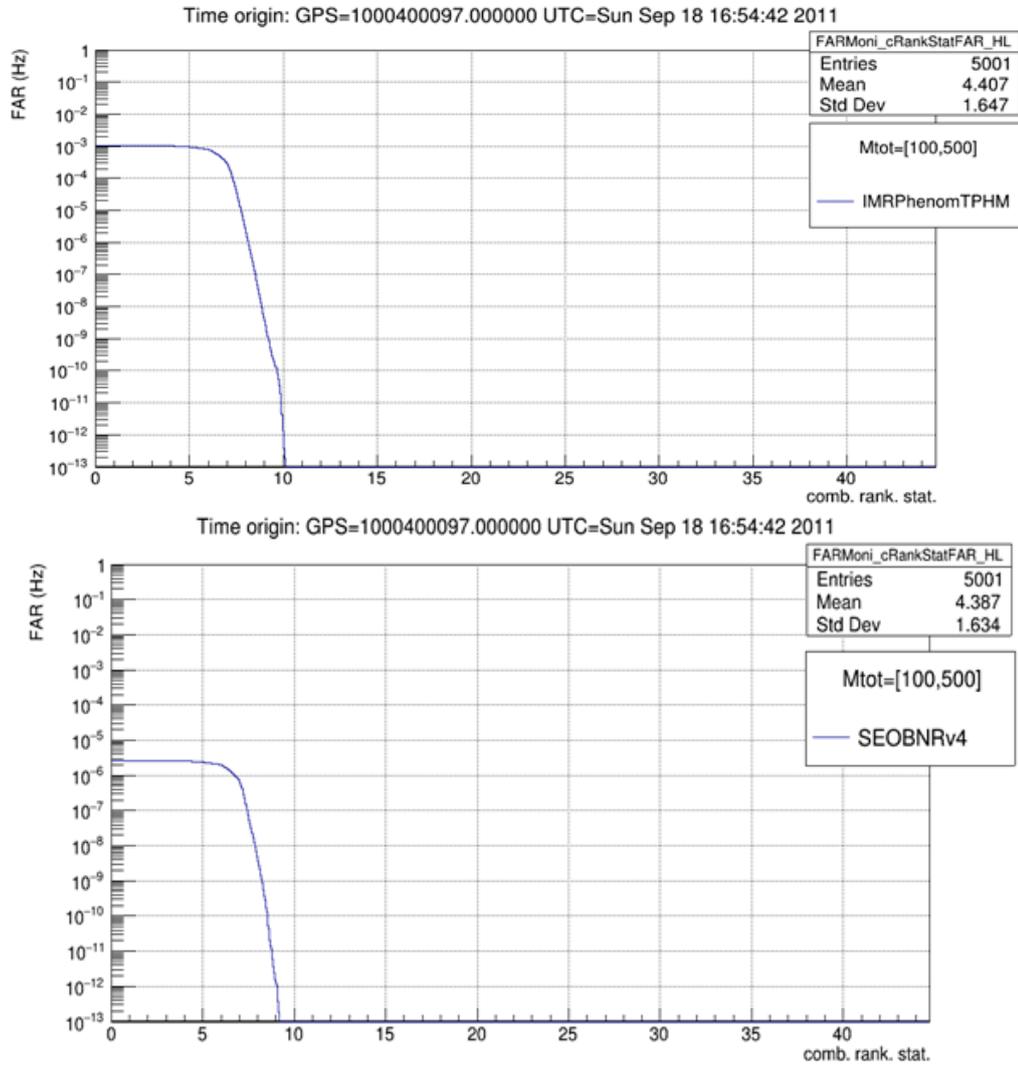
Figure 5.9: FAR of the coincidence (HL) noise-triggers for high mass template banks in Gaussian noise.
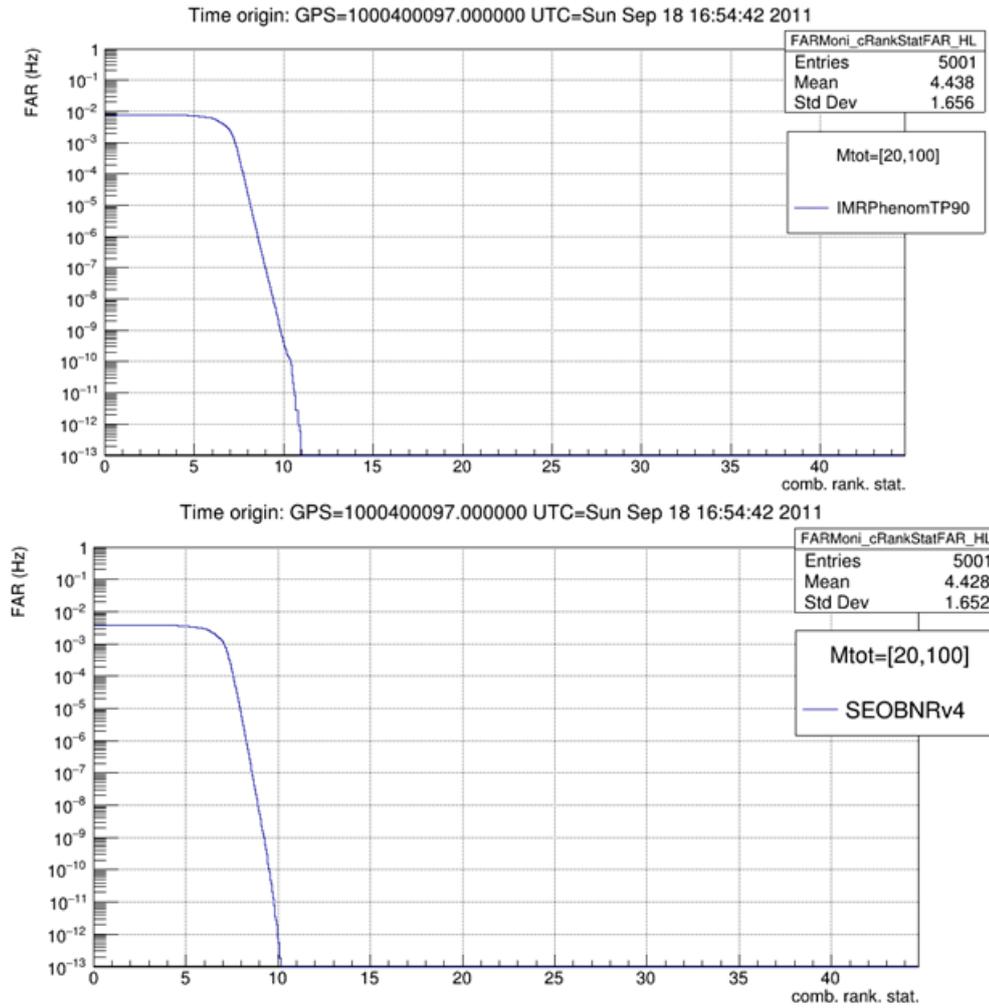
Figure 5.10: FAR of the coincidence (HL) noise-triggers for low mass template banks in Gaussian noise.

High mass banks	FAR [Hz]	Trigger rate
IMRPhenomTPHM (4423)	$0,7 \cdot 10^{-3}\ Hz$	1 Ev $\sim 1,4 \cdot 10^3\ s$
SEOBNRv4 (146)	$2,5 \cdot 10^{-6}\ Hz$	1 Ev $\sim 0.4 \cdot 10^6\ s$

Table 5.4: Coincidence detectors (HL) trigger rates for high mass templates banks in Gaussian noise.

Low mass banks	FAR [Hz]	Trigger rate
IMRPhenomTP (4882)	$5,7 \cdot 10^{-3}\ Hz$	1 Ev$\sim 0,2 \cdot 10^3\ s$
SEOBNRv4 (3798)	$2,6 \cdot 10^{-3}\ Hz$	1 Ev $\sim 0.3 \cdot 10^3\ s$

Table 5.5: Coincidence detectors (HL) trigger rates for low mass templates banks in Gaussian noise.

In the high mass region from the plot of the IFAR in figure 5.11 we can observe that the total number of the found weak precessing injections (strong precessing) with

the cut in $FAR < 10^{-7}\ Hz$ proposed is 8515 (8821) for IMRPhenomTPHM bank and 8091 (8474) for SEOBNRv4 bank, over a total of 10k precessing injections. An injection is considered found if a coincidence event is present within $\pm 1\ s$ the injection's GPS time. The PS bank is more efficient for $IFAR \leq 10^{10}\ s$ values, after which the AS bank starts to recover more weak precessing injections (figure 5.11 top panel). The switch is not present in the plot of IFAR for the detected injections with strong precession, where the PS bank in high mass region performs better (figure 5.11 bottom panel).

Figure 5.11: IFAR of the "weak" precessing detected injections (top panel) and of the "strong" precessing detected injection (bottom panel) for high mass template banks in Gaussian noise.

If we plot the relative difference of the combined ranking statistics for the two

searches $\frac{cRS_{prec}-cRS_{non-prec}}{cRS_{non-prec}}$ we expect that this difference is positive if a precessing-spin search recovers higher SNR (we will refer as common injections the simulated signals found by both PS and AS banks). In figure 5.12 are plotted the relative difference cRS as function of the the precessing spin ($0 < \chi_p < 1$) and effective spin parameter ($-1 < \chi_{eff} < 1$) for weak and strong precessing injections respectively, and we can observe that the precessing-spin bank gains in SNR power of about 10% with respect to the aligned-spin bank with the cut in FAR proposed.

Figure 5.12: Relative difference of the cRS as function of the precessing spin parameter (left panel) and the effective spin parameter (right panel) for the common injections detected by the high mass template banks in Gaussian noise. Top panel "weak" precessing injections, bottom panel "strong" precessing injections. The color bar represent the number of injections in a pixel.

In low mass region from the plots of IFAR in figure 5.13 we observe that the total number of the found injections (stronger precessing) with the same cut in FAR is 5638

(5788) for IMRPhenomTP bank and 5564 (5729) for SEOBNRv4 bank. The PS bank recover more precessing injections but this time the switch in efficiency starts for lower values of the $IFAR > 10^8$ s and in this case is present also in the plot for stronger precessing injections. The PS bank is less efficient and endeed in the plot of the relative difference cRS in figure 5.14 the gain in SNR power is only about of 2% with the same cut in FAR used in the high mass region.
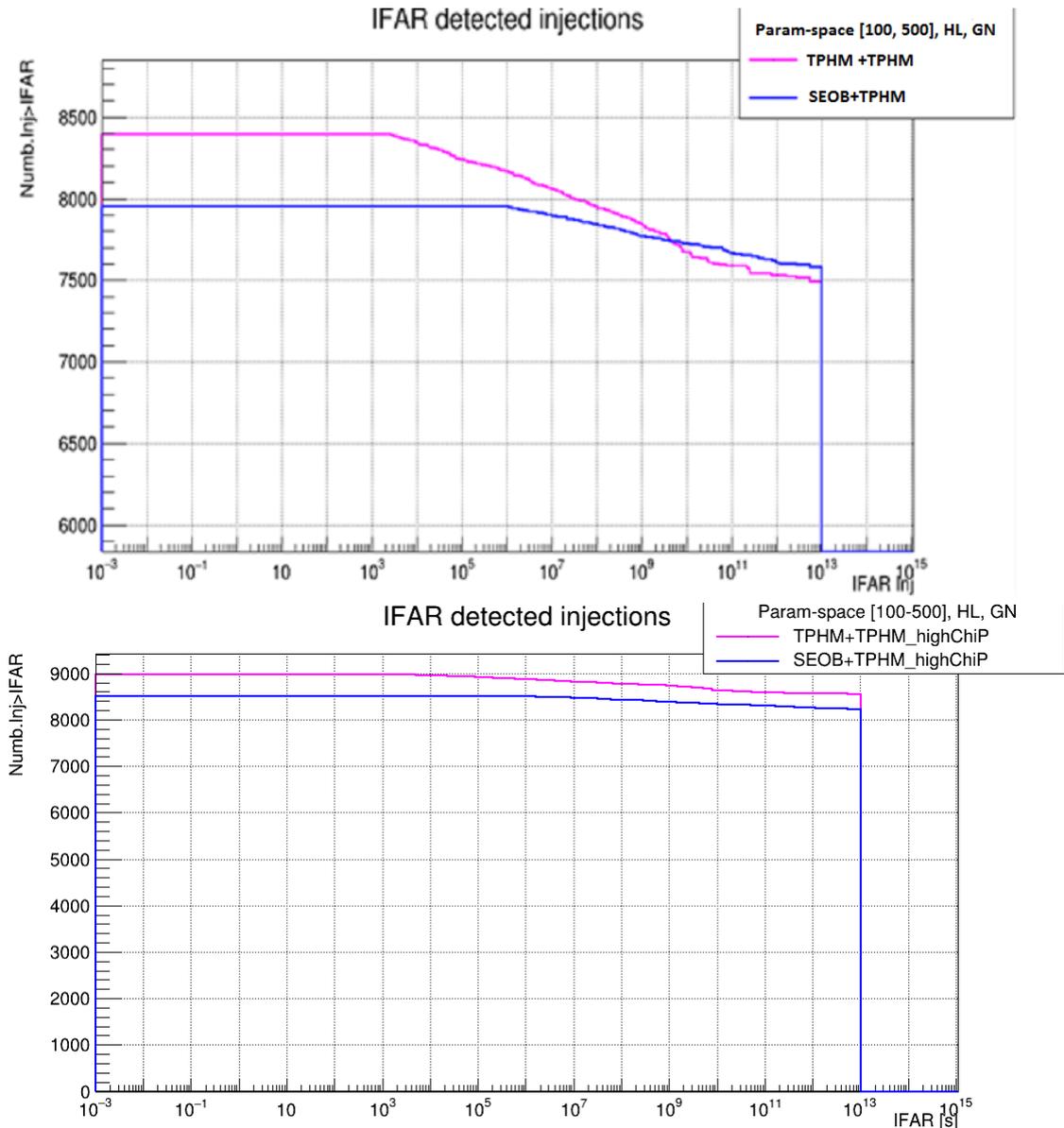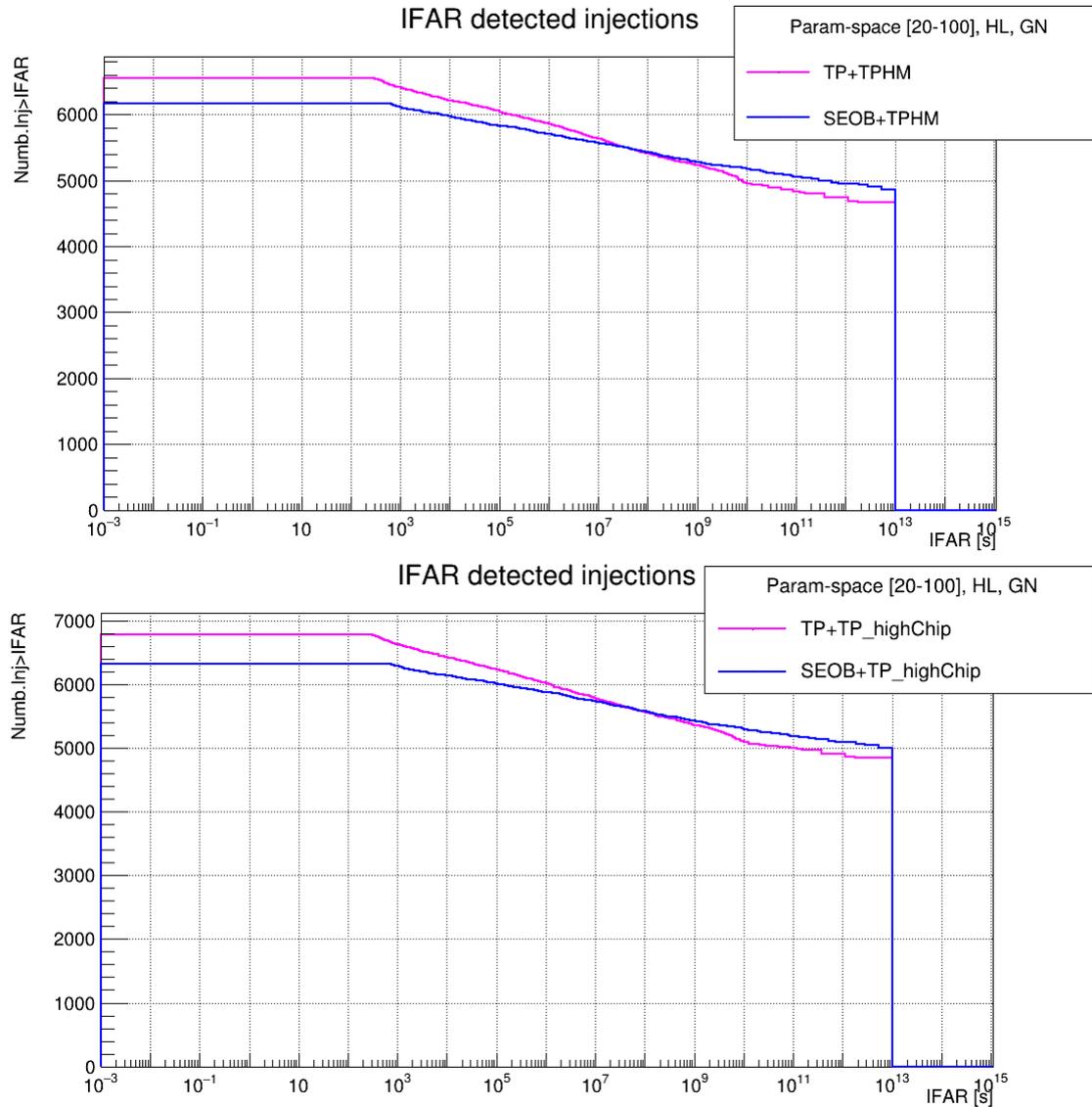

Figure 5.13: IFAR of the "weak" precessing detected injections (top panel) and of the "strong" precessing detected injection (bottom panel) for low mass template banks in Gaussian noise.
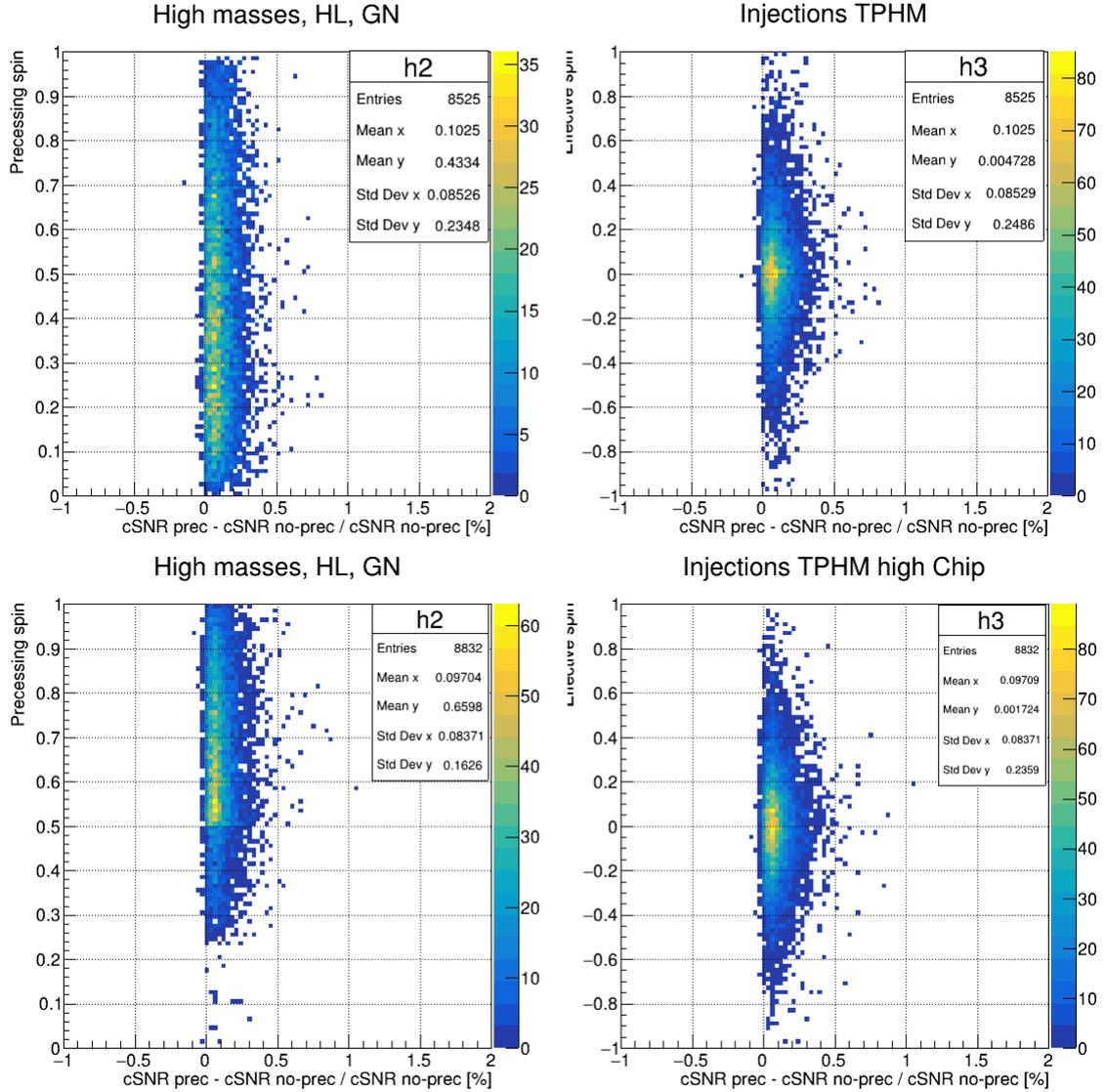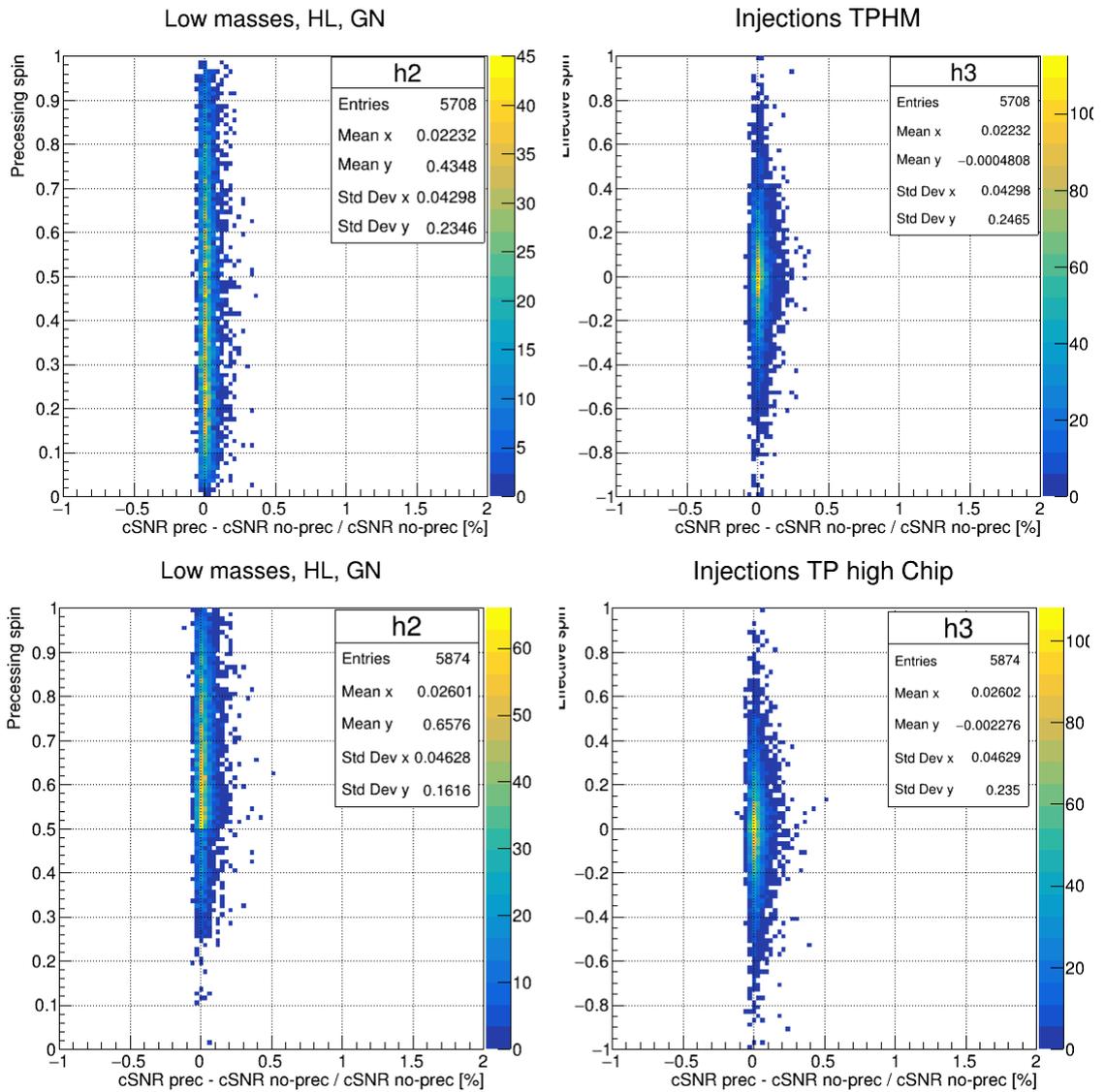
Figure 5.14: Relative difference of the cRS as function of the precessing spin parameter (left panel) and the effective spin parameter (right panel) for the common injections detected by the low mass template banks in Gaussian noise. Top panel "weak" precessing injections, bottom panel "strong" precessing injections. The color bar represent the number of injections in a pixel.

These results are expected because precessing spin template banks shows higher fitting factors with respect to the aligned-spin banks in the banksim tests described in the last chapter, however should be considered as an average effect, because it is possible that some specific injections may have an higher match with a non-precessing template. The adaptive process to compute PSD used to perform the matched filter can make some differences between the two analysis low masses and high masses, because the FFT lenght involved are related to the templates duration and can affects the computed SNR, producing fluctuation on found/missed injections close to the SNR threshold.

5.2.4 Coincident detectors triggers in O3 data

As done previously, the first step is to check how noisy are the banks running MBTA with templates banks and a chunk of O3 data (GPS start time 1361995000) without injections. The minimum FAR reached and the cut in FAR chosen are the same of the ones for the search of coincidences in Gaussian noise. In figures 5.15 and 5.16 are plotted the FAR distributions of coincident noise-triggers in O3 data. Notice that in this case the SNR of the events reach higher values with respect to the gaussian triggers. After this check, the template banks are analyzed in real data adding the injections set.

From the plot of the IFAR of the detected injections for high mass banks in figure 5.17, we can observe that with the cut $FAR < 10^{-7} \ Hz$ the total number of weak precessing injections (strong precessing) found by the PS bank is 3224 (3481) while the ones found by the AS bank is 3958 (4430), that is the performance of SEOBNRv4 bank is better and in addition is more efficient in recovering strong precessing injections with respect to the IMRPhenomTPHM bank. The common injections recovered is reduced of about 30% and this effect is reflected in the plot of the relative difference of the combined ranking statistics in figure 5.19, the precessing bank gains about 20% in SNR power.
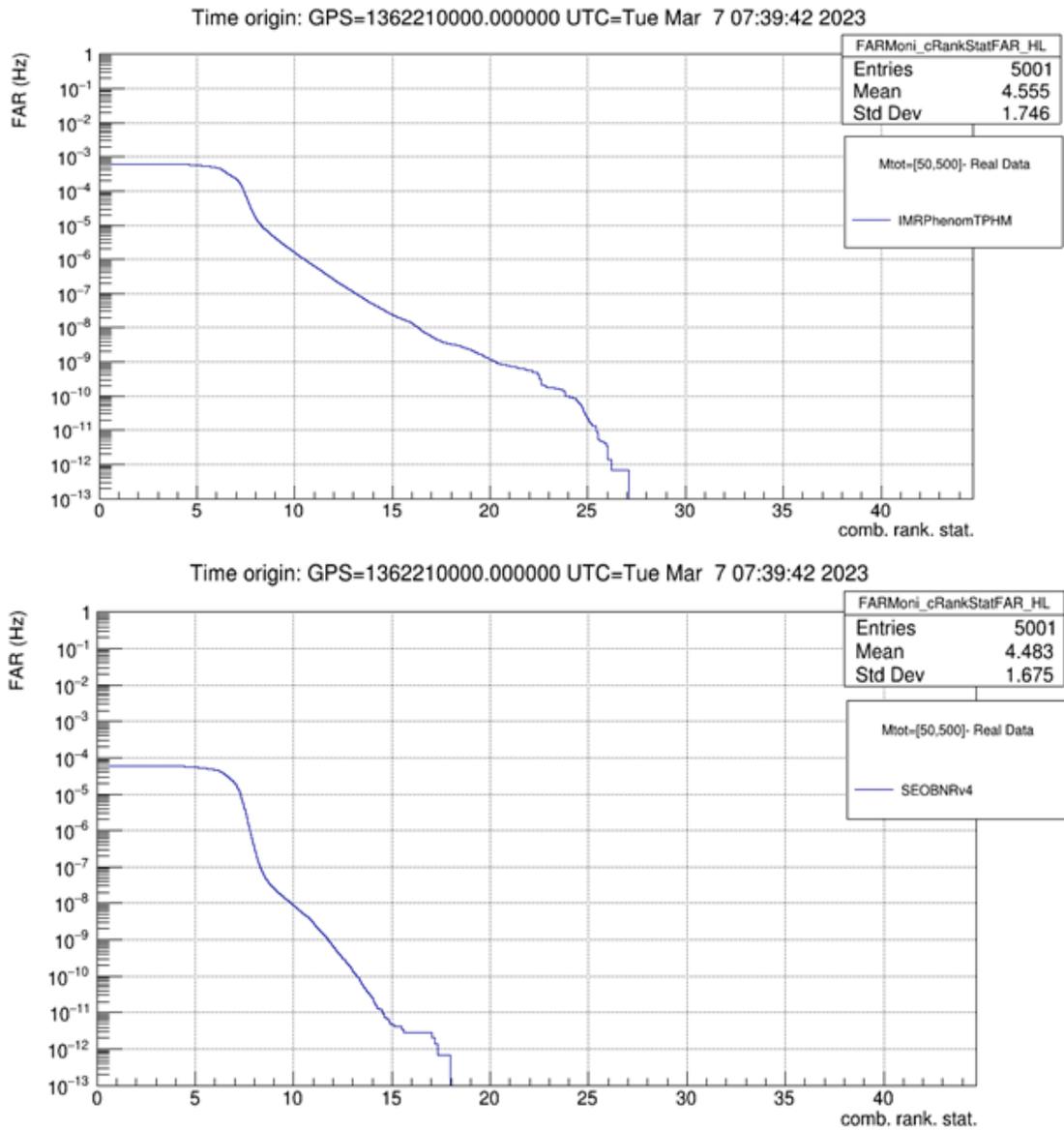
Figure 5.15: FAR of the coincidence (HL) noise-triggers for high mass template banks in O3 data.
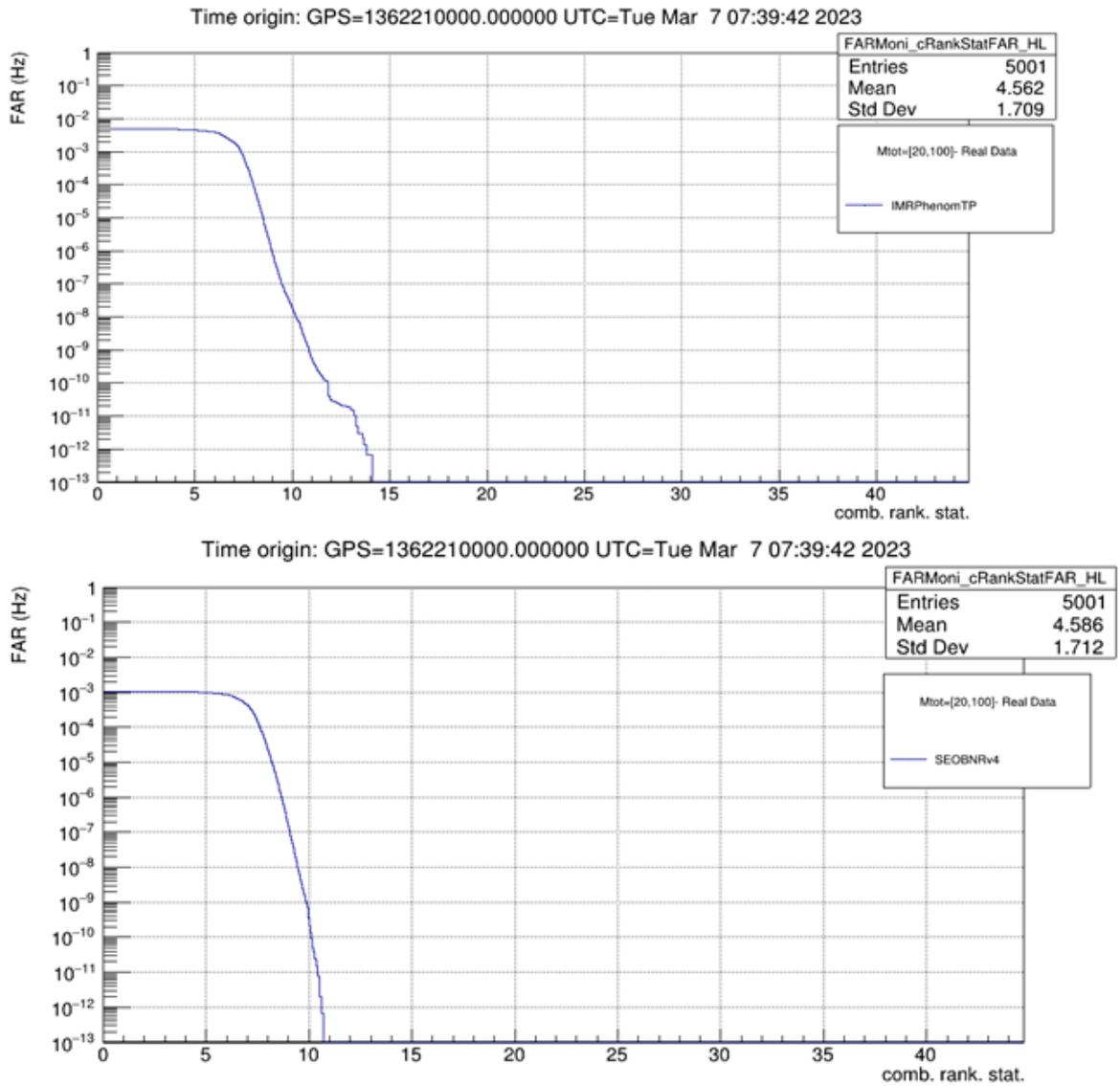
Figure 5.16: FAR of the coincidence (HL) noise-triggers for low mass template banks in O3 data.
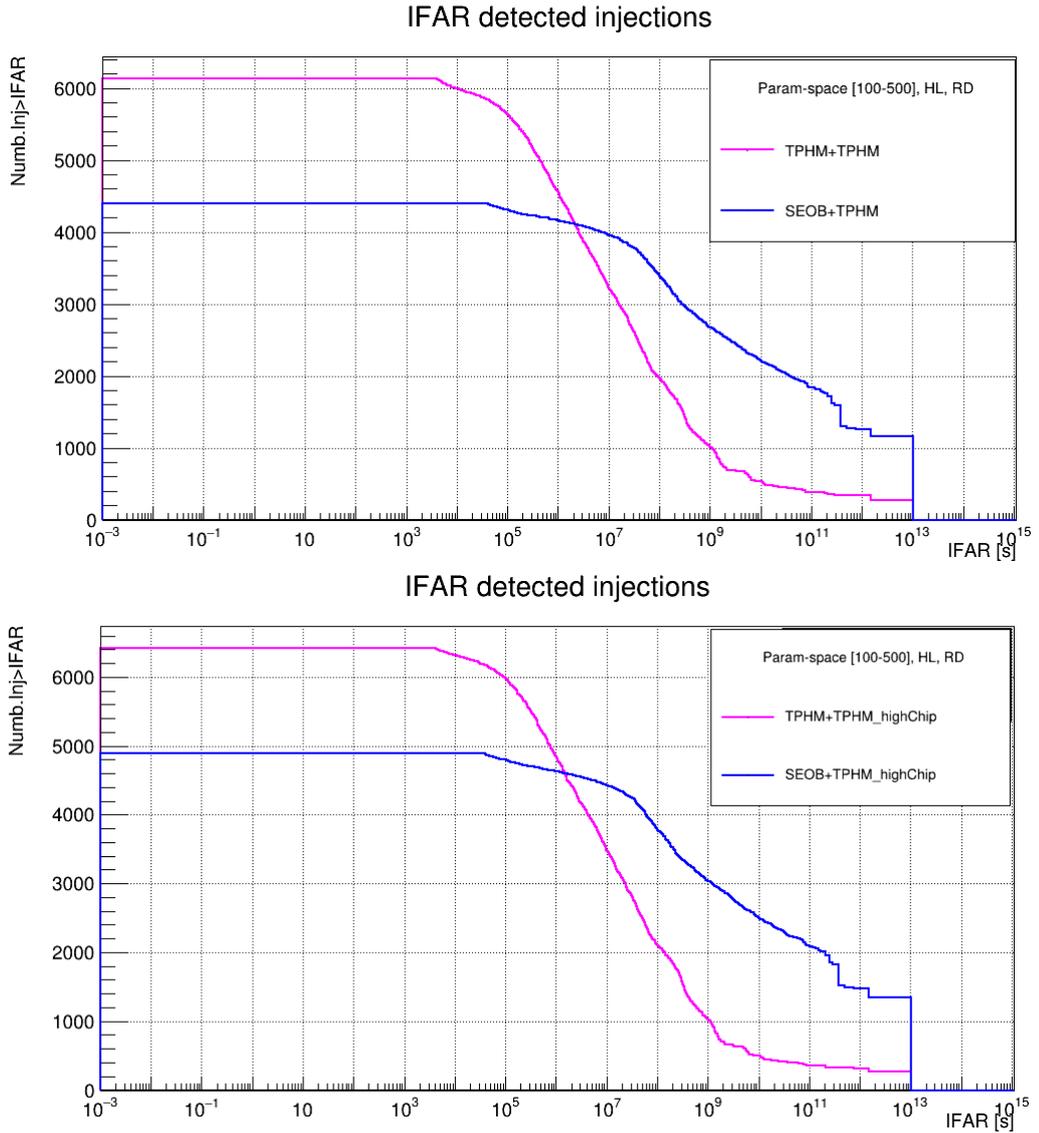
Figure 5.17: IFAR of the detected injections for high mass template banks in O3 data. Top panel weak precessing injections, bottom panel strong precessing injections.

In low mass region the situation change and from the plots of the IFAR of the detected injections by the low mass banks in figure 5.18, we can obserbe that with the same cut in FAR the total number of found weak precessing injections (strong precessing) by the PS bank is 3850 (3986) while the ones found by the AS bank is 3643 (3677), that is the bank IMRPhenomTP is more efficient. In the plots of the cRS in figure 5.20 we can observe that there is a gain of about 5% in SNR power when recovering weak precessing injections and a gain of about 7% when recovering strong precessing injections.
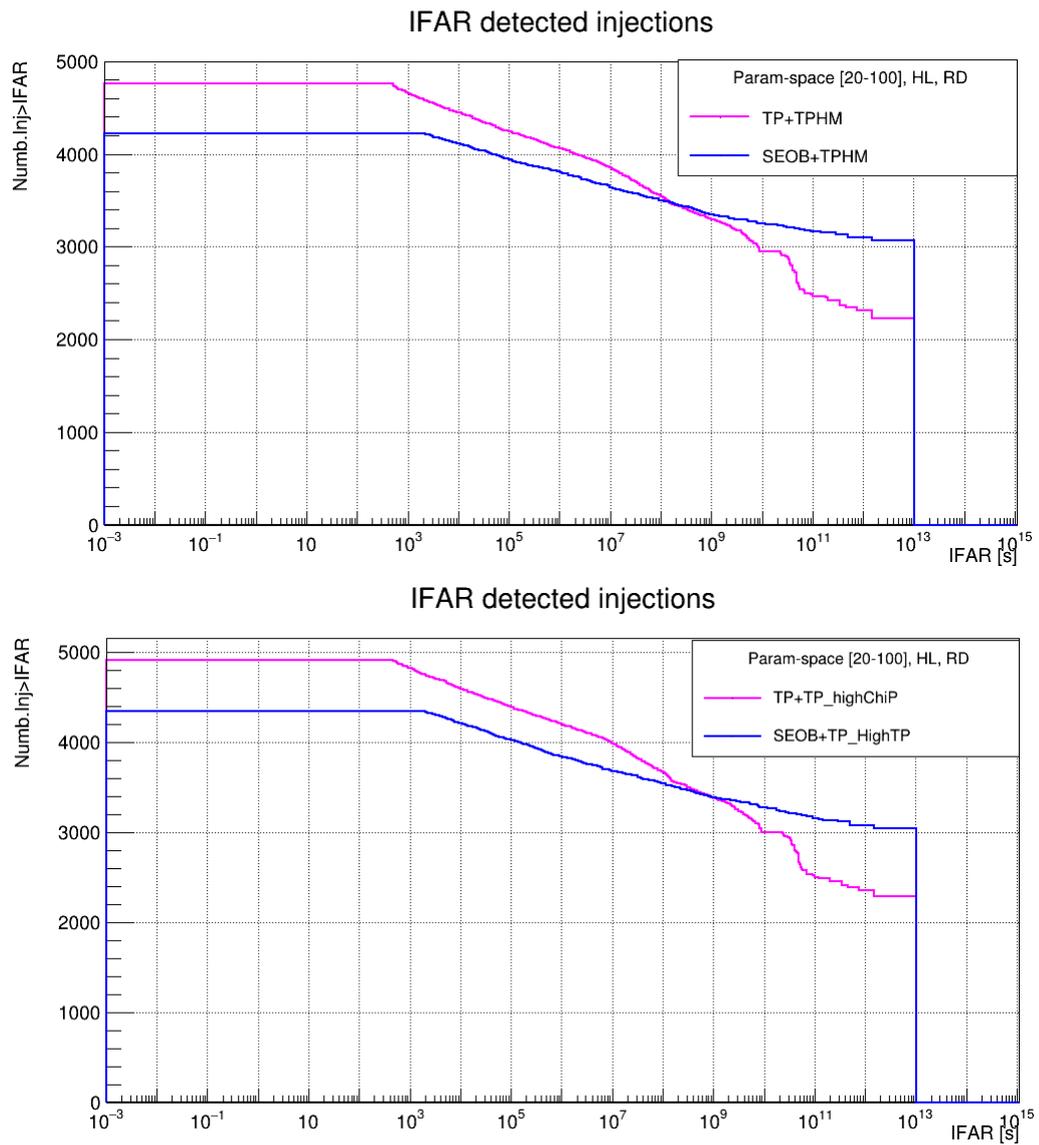
Figure 5.18: IFAR of the detected injections for low mass template banks in O3 data. Top panel weak precessing injections, bottom panel strong precessing injections.
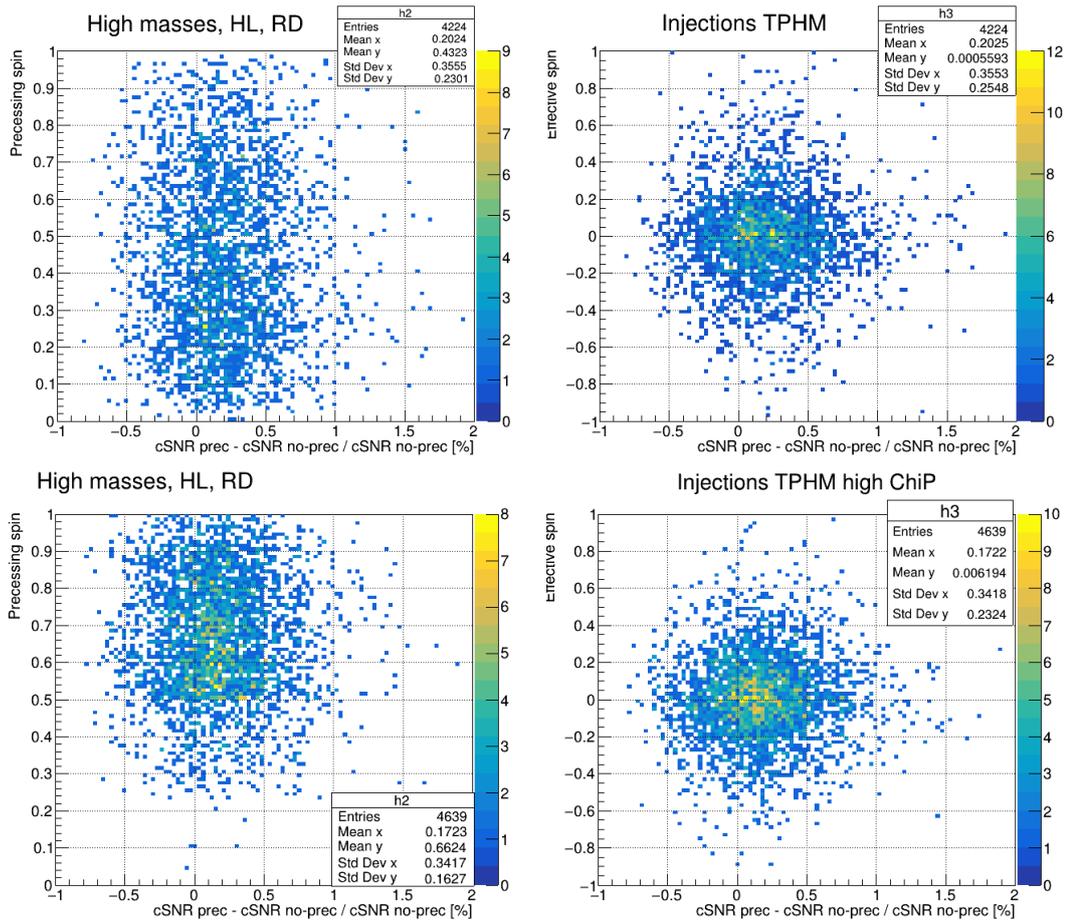
Figure 5.19: Relative difference of the cRS as function of the precessing spin parameter (left panel) and the effective spin parameter (right panel) for the common injections detected by the high mass template banks in O3 data. Top panel "weak" precessing injections, bottom panel "strong" precessing injections. The color bar represent the number of injections in a pixel.
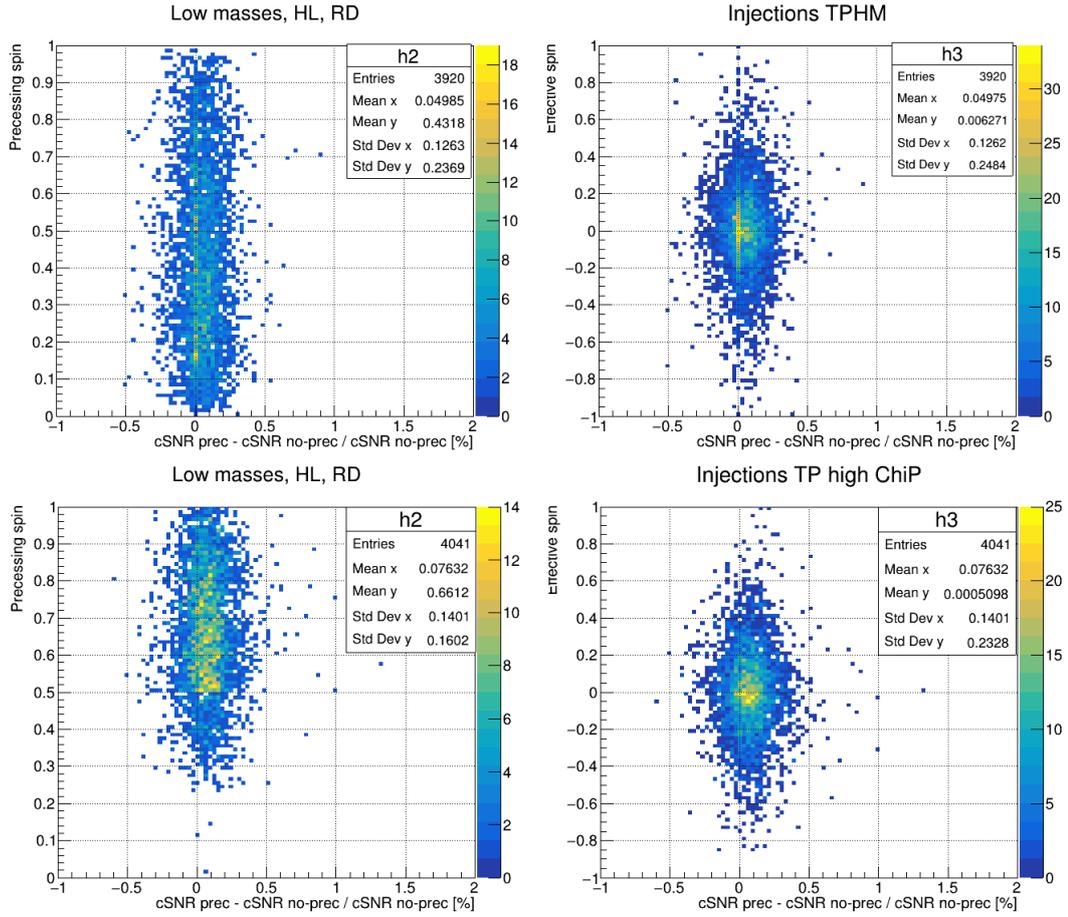
Figure 5.20: Relative difference of the cRS as function of the precessing spin parameter (left panel) and the effective spin parameter (right panel) for the common injections detected by the low mass template banks in O3 data. Top panel weak precessing injections, bottom panel strong precessing injections. The color bar represent the number of the injections in a pixel.

We investigate on the missed injections by the two searches and made the plots of the chirp mass and of the precessing parameter χ_p versus the effective distance, being the effective distance in a double concidence search the minimum distance between the injections recovered in the two detectors data (HL). The injections distribution is uniform in distance in the range $[200 \ Mpc, 2 \ Gpc]$. The plots for the missed weak (strong) precessing injections by the high mass template banks in figure 5.21 (5.22) show that most of the lost injections by both banks overlap all over the space, but in general the IMRPhenomTPHM bank looses more injections also for high values of χ_p. Fluctuations in missed injections can be associated to random association of noise triggers occurred at the injection gps time.While the plots for the missed weak (strong) precessing injections by the low mass template banks in figure 5.23 (5.24) show that in this case the performance of the two searches is comparable.
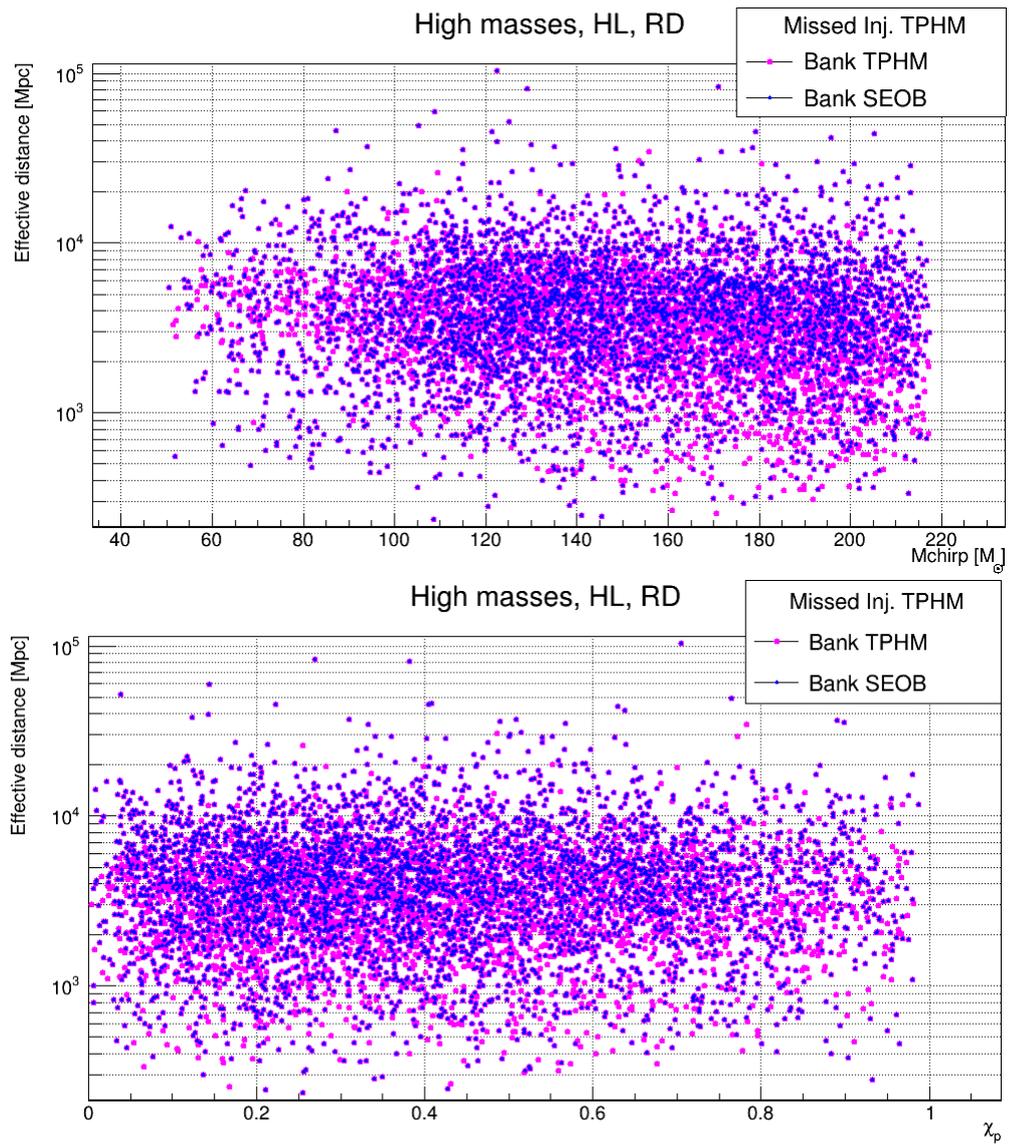
Figure 5.21: Chirp mass (top panel) and precessing parameter χ_p (bottom panel) versus the effective distance of the weak precessing injections missed by the high mass template banks in O3 data.
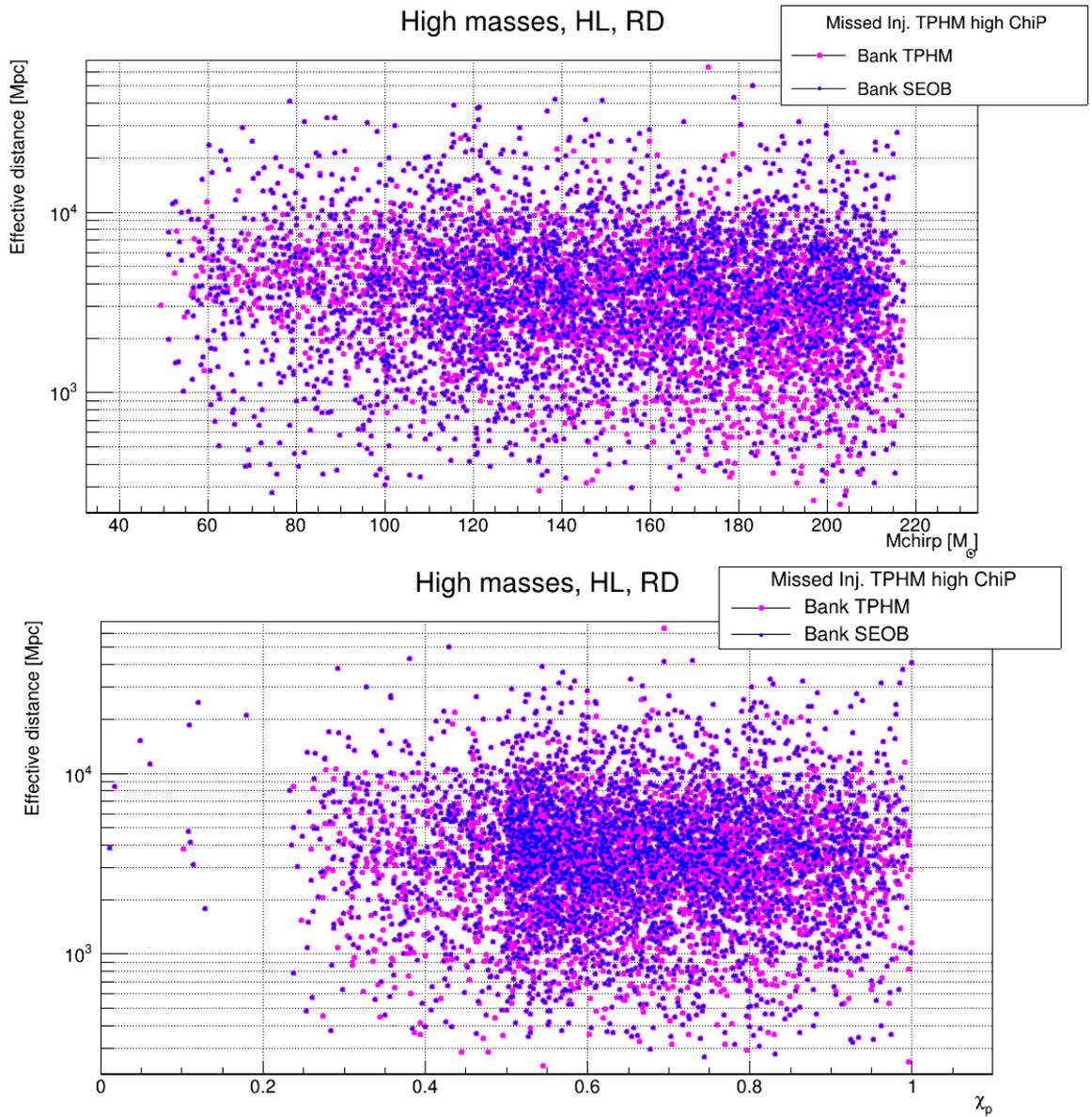
Figure 5.22: Chirp mass (top panel) and precessing parameter χ_p (bottom panel) versus the effective distance of the strong precessing injections missed by the high mass template banks in O3 data.
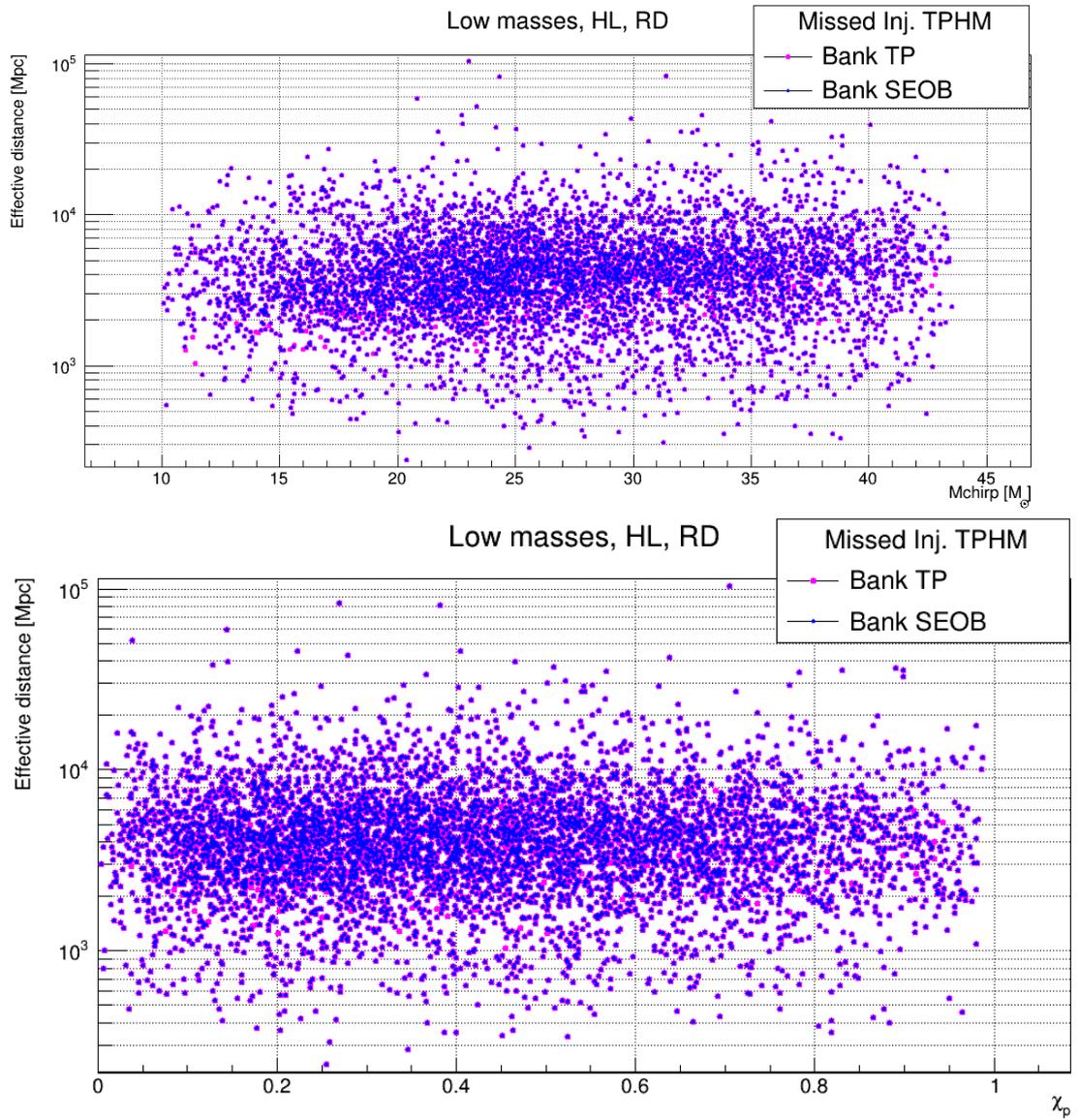
Figure 5.23: Chirp mass (top panel) and precessing parameter χ_p (bottom panel) versus the effective distance of the weak precessing injections missed by the low mass template banks in O3 data.
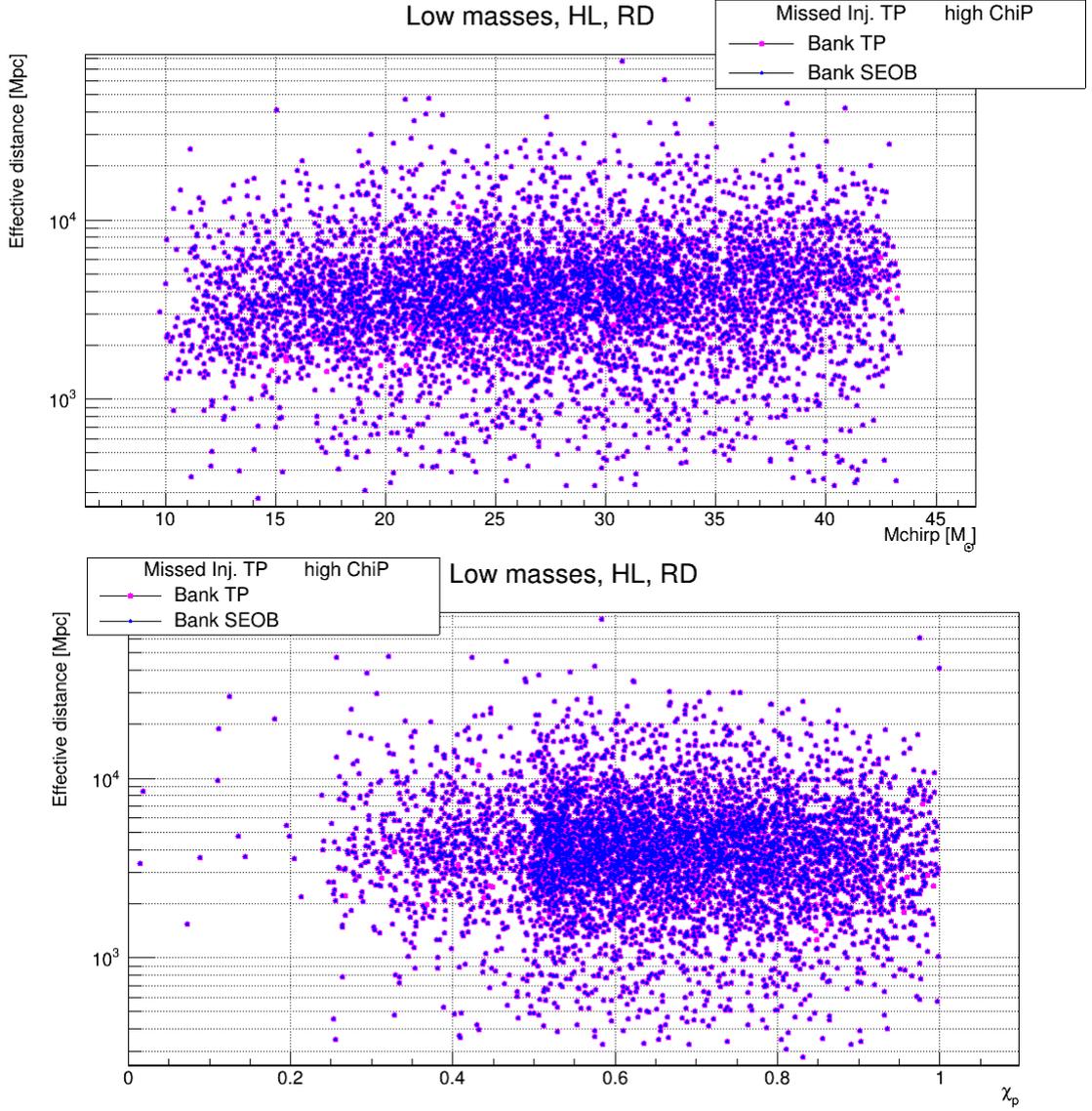
Figure 5.24: Chirp mass (top panel) and precessing parameter χ_p (bottom panel) versus the effective distance of the strong precessing injections missed by the low mass template banks in O3 data.

5.2.5 Search Sensitivity estimations with fixed false-alarm rates

As we have discussed in the previous section, the precessing spin search presents a tiny gain in the recovered SNR than the aligned-spin one for the common detected injections. However, in high mass region the higher number of noise triggers of the IMRPhenomTPHM bank (due to the larger number of templates) with respect to the SEOBNRv4 bank, is not compensated by the gain on the recovered SNR. In low mass region the two analysis performances appear to be similar but there is an advantage in using precessing templates for values of the IFAR limits $< 10^7$ with a gain on the recovered SNR of about 5% (7% in case of strong precessing injections), while for higher values of the IFAR limits the aligned-spin bank is more efficient. For the comparison of

the relative search sensitivity of the two analysis, we plot the mass ratio (q) versus χ_p of the detected injections by the precessing-spin bank divided by the ones detected by the aligned spin bank; we expect values larger than the unity when the precessing-spin search is more efficient. In figure 5.25 we show the plots of the relative search sensitivy for high mass templates banks, in figure 5.26 the ones for low mass template banks. The goodness of the precessing-spin search is more evident in low mass region, where there are values > 1 almost all over the parameter space. We can conclude that a search with precessing-spin template banks can slighlty improve the sensitivity search of the pipeline MBTA for the detection of gravitational wave signals emitted by precessing-spin binary black holes systems with masses in the range $[20, \ 100] \ M_\odot$.

Figure 5.25: Relative search sensitivity of the high mass templates banks in fuction of the mass ratio versus the precessing-spin parameter of the found injections by the two analysis. Top panel weak precessing injections, bottom panel strong precessing injections. The numbers are the relative efficiencies.

Figure 5.26: Relative search sensitivity of the low mass templates banks in fuction of the mass ratio versus the precessing-spin parameter of the found injections by the two analysis. Top panel weak precessing injections, bottom panel strong precessing injections. The numbers are the relative efficiencies.

5.3 Conclusions and future prospects

In this dissertation a search for gravitational wave signals emitted by Binary Black Holes with precessing-spin have been proposed, with the aim of improving the sensitivy search of the pipeline MBTA.

The first part of this work is dedicated to the generation of the templates banks used as filters in the matched filter technique. The target sources have been explored in

two parameters space: a low mass region, where BBH have a total mass in the range $[20, 100]M_\odot$; and an high mass region where the BBH have a total mass in the range $[100, 500]M_\odot$. Both aligned-spin and precessing-spin templates have been generated, employing the effective-one-body models SEOBNRv4 for the aligned-spin waveforms and the phenomenological models IMRPhenom (in time domain and in frequency domain) for the precessing-spin waveforms. For the construction of the banks the PyCBC's tool Sbank has been used, being the latter a stochastic placement algorithm for generic spin-oriented template banks which uses the sky-maxed SNR statistic for the computation of the match. Then the effectualness of the template banks have been computed, i.e. their capability to recover injected signals. For the latter test the PyCBC's tool Banksim has been used. From these preliminary studies it is found, as expected, that the precessing-spin banks have a larger number of templates, since modelling the waveforms with precession effects requires additional parameters than the aligned-spin ones, and that the precessing-spin banks recover precessing signals with higher values of the fitting factors with respect to the aligned-spin ones. The fitting factors distributions plots show that employing precessing-spin wavefroms as filters in a GW search may generally improve the detection efficiency.

However, the banksim test doesn't includes noise transients (glitches) which affect the output data of GW detectors, for this reason the second part of this work focused on studying the implications of adding precessing template banks in a real GW search, analyzing the banks in Gaussian noise first and in a data file of O3 later, performing Monte Carlo tests with the pipeline MBTA. The purposes of the analysis were to check the capability of MBTA to detect precessing simulated GW signals and discriminate them from glitches in the data; to investigate the expected gain in SNR power when using precessing-spin filters compared to aligned-spin ones in a search; to measure the increase of the background false-alarms incurred by filtering the data with more templates.

For the comparison of the two searches (precessing and aligned) three figures of merit have been used: the efficiency of the search, that is the number of injections found with a cut in $FAR < 10^{-7}$ (currently used to asses the significance of GW candidate events for public alerts), the gain in the combined ranking statistic of the common recovered injections, and the performance in terms of the inverse FAR (IFAR), i.e. the significance associated to the coincident events found by MBTA, where coincident events refers to injections found by two detectors (HL) at the same GPS time. From the results of these studies comes out that a precessing-spin search presents a tiny gain in the recovered SNR of the common found injections with the respect to the aligned-spin search. In particular, for high mass template banks the higher number of noise triggers, due to the larger number of templates, does not compensate the gain of the recovered SNR. For low mass template banks there is a gain of about $5 - 7\%$. In addition, the relative search sensitivity which compare the efficiency of the two searches in terms of the mass ratio of the detected injections versus the precessing-spin parameter $0 < \chi_p < 1$ (which quantify the precession in the injected signal), shows that the precessing-spin search is more efficient than the non-precessing one in a big part of the parameter space analyzed, especially in the low mass region. The conclusion is that using precessing template banks as filters in a GW search for low mass BBH with precession of the spins can slightly improve the detection efficiency of the pipeline MBTA. A problem found

is that the gain in SNR is not compenseted by the increase of the false-alarms, then the search could be more efficient by improving the signal consistency tests (χ^2 tests) trying to reduce the noise. Another interesting possibility would be to analize a template bank with precessing waveforms generated with only high values of the mass ratio and of χ_p. The pipeline MBTA has been used to perform low-latency searches for compact binary coalescences signals ever since the science run S6 and VSR2/VSR3 of the first-generation gravitational wave detectors. Due to the diversity of the GW signals observed by the advanced detectors in recent years, which include BNS mergers enabling electromagnetic emission, heavy BBH mergers and candidate events of IMBH as well as NS-BH mergers, it's necessary to improve MBTA. It worth to mention the most recent development of the pipeline, like: the adaptation to perform off-line searches, high statistics injections runs, extension of the search to high mass systems, the inclusion of sub-threshold information to improve the sky location of the sources. In the prospective of the future third generation GW detectors, new challenges await all the pipelines used for on-line and/or off-line searches by the LIGO-Virgo Collaboration, and MBTA is well suited to expand its new features to a detection extended both at low frequencies and high frequencies through its multiband analysis.

Ringraziamenti

Ringrazio di cuore il mio supervisore di tesi Gianluca Guidi per tutto l'aiuto e il sostegno ricevuto durante i tre anni di dottorato. Un ringraziamento sincero anche a tutti gli altri membri del gruppo di Urbino e del gruppo di MBTA, per l'accoglienza e la disponibilità ad aiutarmi, tra i quali in particolare Florian e Francesco. Un ringraziamento speciale è rivolto a Michele Fabi, per gli aiuti tecnici in ufficio, i consigli, ma soprattutto per la sua amicizia.
Voglio ringraziare inoltre i miei più cari amici Pasquale, Maurizio e Tiziana, che nonostante il trascorrere degli anni e le vicissitudini della vita che ci hanno divisi, restano i miei più entusiasti sostenitori.
Ringrazio infine la mia famiglia, Carrie e Rocky compresi.

Bibliography

[1] M. Maggiore and Oxford University Press. *Gravitational Waves: Volume 1: Theory and Experiments*. Gravitational Waves. OUP Oxford, 2008.

[2] Theocharis A Apostolatos, Curt Cutler, Gerald J Sussman, and Kip S Thorne. Spin-induced orbital precession and its modulation of the gravitational waveforms from merging binaries. *Physical Review D*, 49(12):6274, 1994.

[3] R. Abbott et. al. GW190412: Observation of a binary-black-hole coalescence with asymmetric masses. *Physical Review D*, 102(4), aug 2020.

[4] Mark Hannam, Charlie Hoy, Jonathan E. Thompson, Stephen Fairhurst, Vivien Raymond, Marta Colleoni, Derek Davis, Hector Estelles, Carl-Johan Haster, Adrian Helmling-Cornell, Sascha Husa, David Keitel, T. J. Massinger, Alexis Menendez-Vazquez, Kentaro Mogushi, Serguei Ossokine, Ethan Payne, Geraint Pratten, Isobel Romero-Shaw, Jam Sadiq, Patricia Schmidt, Rodrigo Tenorio, Richard Udall, John Veitch, Daniel Williams, Anjali Balasaheb Yelikar, and Aaron Zimmerman. General-relativistic precession in a black-hole binary. *Nature*, 610(7933):652–655, oct 2022.

[5] Ben Farr, Daniel E Holz, and Will M Farr. Using spin to understand the formation of ligo and virgo's black holes. *The Astrophysical Journal Letters*, 854(1):L9, 2018.

[6] Salvatore Vitale, Ryan Lynch, Riccardo Sturani, and Philip Graff. Use of gravitational waves to probe the formation channels of compact binaries. *Classical and Quantum Gravity*, 34(3):03LT01, 2017.

[7] Takuya Tsutsui, Atsushi Nishizawa, and Soichiro Morisaki. Early warning of precessing compact binary merger with third-generation gravitational-wave detectors. *Physical Review D*, 104(6), sep 2021.

[8] E. Calloni and G. Vajente. *Lectures in Astrophysics*.

[9] S.L. Shapiro and S.A. Teukolsky. *Black Holes, White Dwarfs, and Neutron Stars: The Physics of Compact Objects*. Wiley, 2008.

[10] F.D. Seward and P.A. Charles. *Exploring the X-ray Universe*. Cambridge University Press, 2010.

[11] Marco Celoria, Roberto Oliveri, Alberto Sesana, and Michela Mapelli. Lecture notes on black hole binary astrophysics. *arXiv preprint arXiv:1807.11489*, 2018.

[12] Nelson Christensen. Stochastic gravitational wave backgrounds. *Reports on Progress in Physics*, 82(1):016903, Nov 2018.

[13] R. Abbott and T. D. et. al. Abbott. Population of merging compact binaries inferred using gravitational waves through gwtc-3. *Physical Review X*, 13(1), Mar 2023.

[14] Giampiero Esposito, Gaetano Lambiase, Giuseppe Marmo, Gaetano Scarpetta, and Gaetano Vilasi. *General relativity and gravitational physics. 16th SIGRAV conference on general relativity and gravitational physics, Vietri sul Mare, Italy, September 13–16, 2004*. 01 2005.

[15] H. Kogelnik and T. Li. Laser beams and resonators. *Appl. Opt.*, 5(10):1550–1567, Oct 1966.

[16] A. Kuzmich, L. Mandel, and N. P. Bigelow. Generation of spin squeezing via continuous quantum nondemolition measurement. *Phys. Rev. Lett.*, 85:1594–1597, Aug 2000.

[17] Rana Adhikari, Thomas J. Greytak, and Rana Adhikari. Gravitational wave antennae, 2004.

[18] Stephen Fairhurst. Localization of transient gravitational wave sources: beyond triangulation. *Classical and Quantum Gravity*, 35(10):105002, apr 2018.

[19] Ethan Payne, Sophie Hourihane, Jacob Golomb, Rhiannon Udall, Derek Davis, and Katerina Chatziioannou. Curious case of GW200129: Interplay between spin-precession inference and data-quality issues. *Physical Review D*, 106(10), nov 2022.

[20] R. Abbott et. al. *Physical Review Letters*, 125(10), sep 2020.

[21] AV Tutukov and AM Cherepashchuk. The evolution of close binary stars. *Astronomy Reports*, 60:461–476, 2016.

[22] SE Woosley and Alexander Heger. The pair-instability mass gap for black holes. *The Astrophysical Journal Letters*, 912(2):L31, 2021.

[23] Sebastien Clesse and Juan Garcia-Bellido. Gw190425, gw190521 and gw190814: Three candidate mergers of primordial black holes from the qcd epoch, 2021.

[24] S. E. Woosley and Alexander Heger. The pair-instability mass gap for black holes. *The Astrophysical Journal Letters*, 912(2):L31, may 2021.

[25] V. De Luca, V. Desjacques, G. Franciolini, P. Pani, and A. Riotto. GW190521 mass gap event and the primordial black hole scenario. *Physical Review Letters*, 126(5), feb 2021.

[26] Simone S. Bavera, Tassos Fragos, Ying Qin, Emmanouil Zapartas, Coenraad J. Neijssel, Ilya Mandel, Aldo Batta, Sebastian M. Gaebel, Chase Kimball, and Simon Stevenson. The origin of spin in binary black holes. *Astronomy &amp Astrophysics*, 635:A97, mar 2020.

[27] Ben Farr, Daniel E. Holz, and Will M. Farr. Using spin to understand the formation of LIGO and virgo's black holes. *The Astrophysical Journal*, 854(1):L9, feb 2018.

[28] Salvatore Vitale, Ryan Lynch, Riccardo Sturani, and Philip Graff. Use of gravitational waves to probe the formation channels of compact binaries. *Classical and Quantum Gravity*, 34(3):03LT01, Jan 2017.

[29] R. X. Adhikari, V. B. Adya, C. Affeldt, and et al. Gwtc-1: A gravitational-wave transient catalog of compact binary mergers observed by ligo and virgo during the first and second observing runs. *Physical Review X*, 9(3), Sep 2019.

[30] M. COLEMAN MILLER and E. J. M. COLBERT. INTERMEDIATE-MASS BLACK HOLES. *International Journal of Modern Physics D*, 13(01):1–64, jan 2004.

[31] Jenny E Greene and Luis C Ho. Active galactic nuclei with candidate intermediate-mass black holes. *The Astrophysical Journal*, 610(2):722, 2004.

[32] Jillian Bellovary, Alyson Brooks, Monica Colpi, Michael Eracleous, Kelly Holley-Bockelmann, Ann Hornschemeier, Lucio Mayer, Priya Natarajan, Jacob Slutsky, and Michael Tremmel. Where are the intermediate mass black holes? *arXiv preprint arXiv:1903.08144*, 2019.

[33] Jenny E Greene, Jay Strader, and Luis C Ho. Intermediate-mass black holes. *Annual Review of Astronomy and Astrophysics*, 58:257–312, 2020.

[34] Marco Dall'Amico, Michela Mapelli, Ugo N Di Carlo, Yann Bouffanais, Sara Rastello, Filippo Santoliquido, Alessandro Ballone, and Manuel Arca Sedda. GW190521 formation via three-body encounters in young massive star clusters. *Monthly Notices of the Royal Astronomical Society*, 508(2):3045–3054, oct 2021.

[35] Jorge Casares and Peter G Jonker. Mass measurements of stellar and intermediate-mass black holes. *Space Science Reviews*, 183:223–252, 2014.

[36] Carl L. Rodriguez, Sourav Chatterjee, and Frederic A. Rasio. Binary black hole mergers from globular clusters: Masses, merger rates, and the impact of stellar evolution. *Physical Review D*, 93(8), apr 2016.

[37] Michela Mapelli, Marco Dall'Amico, Yann Bouffanais, Nicola Giacobbo, Manuel Arca Sedda, M Celeste Artale, Alessandro Ballone, Ugo N Di Carlo, Giuliano Iorio, Filippo Santoliquido, and Stefano Torniamenti. Hierarchical black hole mergers in young, globular and nuclear star clusters: the effect of metallicity, spin and cluster properties. *Monthly Notices of the Royal Astronomical Society*, 505(1):339–358, may 2021.

[38] Elena Gonzalez, Kyle Kremer, Sourav Chatterjee, Giacomo Fragione, Carl L. Rodriguez, Newlin C. Weatherford, Claire S. Ye, and Frederic A. Rasio. Intermediate-mass black holes from high massive-star binary fractions in young star clusters. *The Astrophysical Journal*, 908(2):L29, feb 2021.

[39] Kyle Kremer, Mario Spera, Devin Becker, Sourav Chatterjee, Ugo N. Di Carlo, Giacomo Fragione, Carl L. Rodriguez, Claire S. Ye, and Frederic A. Rasio. Populating the upper black hole mass gap through stellar collisions in young star clusters. *The Astrophysical Journal*, 903(1):45, oct 2020.

[40] Manuel Arca Sedda, Francesco Paolo Rizzuto, Thorsten Naab, Jeremiah Ostriker, Mirek Giersz, and Rainer Spurzem. Breaching the limit: Formation of GW190521-like and IMBH mergers in young massive clusters. *The Astrophysical Journal*, 920(2):128, oct 2021.

[41] M. Gröbner, W. Ishibashi, S. Tiwari, M. Haney, and P. Jetzer. Binary black hole mergers in AGN accretion discs: gravitational wave rate density estimates. 638:A119, jun 2020.

[42] B McKernan, K E S Ford, R O'Shaugnessy, and D Wysocki. Monte carlo simulations of black hole mergers in AGN discs: Low eff mergers and predictions for LIGO. *Monthly Notices of the Royal Astronomical Society*, 494(1):1203–1216, apr 2020.

[43] Sebastian Khan, Katerina Chatziioannou, Mark Hannam, and Frank Ohme. Phenomenological model for the gravitational-wave signal from precessing binary black holes with two-spin effects. *Physical Review D*, 100(2):024059, 2019.

[44] Lawrence E. Kidder. Coalescing binary systems of compact objects to $(\mathrm{post})^{5/2}$-newtonian order. v. spin effects. *Phys. Rev. D*, 52:821–847, Jul 1995.

[45] Rhys Green, Charlie Hoy, Stephen Fairhurst, Mark Hannam, Francesco Pannarale, and Cory Thomas. Identifying when precession can be measured in gravitational waveforms. *Physical Review D*, 103(12), jun 2021.

[46] Alessandra Buonanno, Yanbei Chen, and Michele Vallisneri. Detecting gravitational waves from precessing binaries of spinning compact objects: Adiabatic limit. *Physical Review D*, 67(10):104025, 2003.

[47] P. Ajith, N. Fotopoulos, S. Privitera, A. Neunzert, N. Mazumder, and J. Weinstein. Effectual template bank for the detection of gravitational waves from inspiralling compact binaries with generic spins. *Physical Review D*, 89(8), apr 2014.

[48] Charlie Hoy, Cameron Mills, and Stephen Fairhurst. Evidence for subdominant multipole moments and precession in merging black-hole-binaries from gwtc-2.1. *Physical Review D*, 106(2):023019, 2022.

[49] Stephen Fairhurst, Rhys Green, Charlie Hoy, Mark Hannam, and Alistair Muir. Two-harmonic approximation for gravitational waveforms from precessing binaries. *Physical Review D*, 102(2), jul 2020.

[50] Patricia Schmidt, Frank Ohme, and Mark Hannam. Towards models of gravitational waveforms from generic binaries: II. modelling precession effects with a single effective precession parameter. *Physical Review D*, 91(2), jan 2015.

[51] B.P. et. al.. Abbott. Properties of the binary black hole merger gw150914. *Physical Review Letters*, 116(24), Jun 2016.

[52] Carole Périgois, Michela Mapelli, Filippo Santoliquido, Yann Bouffanais, and Roberta Rufolo. Binary black hole spins: model selection with gwtc-3, 2023.

[53] Juan Calderon Bustillo, Pablo Laguna, and Deirdre Shoemaker. Detectability of gravitational waves from binary black holes: Impact of precession and higher modes. *Physical Review D*, 95(10):104038, 2017.

[54] Ian Harry, Stephen Privitera, Alejandro Bohe, and Alessandra Buonanno. Searching for gravitational waves from compact binaries with precessing spins. *Physical Review D*, 94(2):024012, 2016.

[55] Rhys Green, Charlie Hoy, Stephen Fairhurst, Mark Hannam, Francesco Pannarale, and Cory Thomas. Identifying when precession can be measured in gravitational waveforms. *Physical Review D*, 103(12):124023, 2021.

[56] Bruce Allen. mml:math xmlns:mml="http://www.w3.org/1998/math/MathML" display="inline"mml:msupmml:mi/mml:mimml:mn2/mml:mn/mml:msup/mml:mathtime-frequency discriminator for gravitational wave detection. *Physical Review D*, 71(6), mar 2005.

[57] Bruce Allen, Warren G. Anderson, Patrick R. Brady, Duncan A. Brown, and Jolien D. E. Creighton. FINDCHIRP: An algorithm for detection of gravitational waves from inspiraling compact binaries. *Physical Review D*, 85(12), jun 2012.

[58] Tito Dal Canton, Alexander H. Nitz, Andrew P. Lundgren, Alex B. Nielsen, Duncan A. Brown, Thomas Dent, Ian W. Harry, Badri Krishnan, Andrew J. Miller, Karl Wette, Karsten Wiesner, and Joshua L. Willis. Implementing a search for aligned-spin neutron star-black hole systems with advanced ground based gravitational wave detectors. *Physical Review D*, 90(8), oct 2014.

[59] Samantha A Usman, Alexander H Nitz, Ian W Harry, Christopher M Biwer, Duncan A Brown, Miriam Cabero, Collin D Capano, Tito Dal Canton, Thomas Dent, Stephen Fairhurst, Marcel S Kehl, Drew Keppel, Badri Krishnan, Amber Lenon, Andrew Lundgren, Alex B Nielsen, Larne P Pekowsky, Harald P Pfeiffer, Peter R Saulson, Matthew West, and Joshua L Willis. The PyCBC search for gravitational waves from compact binary coalescence. *Classical and Quantum Gravity*, 33(21):215004, oct 2016.

[60] Alexander H. Nitz, Thomas Dent, Tito Dal Canton, Stephen Fairhurst, and Duncan A. Brown. Detecting binary compact-object mergers with gravitational waves: Understanding and improving the sensitivity of the PyCBC search. *The Astrophysical Journal*, 849(2):118, nov 2017.

[61] Tito Dal Canton and Ian W. Harry. Designing a template bank to observe compact binary coalescences in advanced ligo's second observing run, 2017.

[62] Sebastian Khan, Sascha Husa, Mark Hannam, Frank Ohme, Michael Pürrer, Xisco Jiménez Forteza, and Alejandro Bohé. Frequency-domain gravitational waves from nonprecessing black-hole binaries. ii. a phenomenological model for the advanced detector era. *Physical Review D*, 93(4), February 2016.

[63] Lionel London, Sebastian Khan, Edward Fauchon-Jones, Cecilio García, Mark Hannam, Sascha Husa, Xisco Jiménez-Forteza, Chinmay Kalaghatgi, Frank Ohme, and Francesco Pannarale. First higher-multipole model of gravitational waves from spinning and coalescing black-hole binaries. *Physical Review Letters*, 120(16), April 2018.

[64] Sebastian Khan, Katerina Chatziioannou, Mark Hannam, and Frank Ohme. Phenomenological model for the gravitational-wave signal from precessing binary black holes with two-spin effects. *Physical Review D*, 100(2), July 2019.

[65] Andrea Taracchini, Alessandra Buonanno, Yi Pan, Tanja Hinderer, Michael Boyle, Daniel A. Hemberger, Lawrence E. Kidder, Geoffrey Lovelace, Abdul H. Mroué, Harald P. Pfeiffer, Mark A. Scheel, Béla Szilágyi, Nicholas W. Taylor, and Anil Zenginoglu. Effective-one-body model for black-hole binaries with generic mass ratios and spins. *Physical Review D*, 89(6), March 2014.

[66] Alejandro Bohé, Lijing Shao, Andrea Taracchini, Alessandra Buonanno, Stanislav Babak, Ian W. Harry, Ian Hinder, Serguei Ossokine, Michael Pürrer, Vivien Raymond, Tony Chu, Heather Fong, Prayush Kumar, Harald P. Pfeiffer, Michael Boyle, Daniel A. Hemberger, Lawrence E. Kidder, Geoffrey Lovelace, Mark A. Scheel, and Béla Szilágyi. Improved effective-one-body model of spinning, nonprecessing binary black holes for the era of gravitational-wave astrophysics with advanced detectors. *Physical Review D*, 95(4), February 2017.

[67] Stephen Privitera, Satyanarayan RP Mohapatra, Parameswaran Ajith, Kipp Cannon, Nickolas Fotopoulos, Melissa A Frei, Chad Hanna, Alan J Weinstein, and John T Whelan. Improving the sensitivity of a search for coalescing binary black holes with nonprecessing spins in gravitational wave data. *Physical Review D*, 89(2):024003, 2014.

[68] Antoni Ramos-Buades, Patricia Schmidt, Geraint Pratten, and Sascha Husa. Validity of common modeling approximations for precessing binary black holes with higher-order modes. *Physical Review D*, 101(10):103014, 2020.

[69] Ian Harry, Juan Calderón Bustillo, and Alex Nitz. Searching for the full symphony of black hole binary mergers. *Physical Review D*, 97(2):023004, 2018.

[70] Alexandre Le Tiec, Luc Blanchet, and Bernard F. Whiting. First law of binary black hole mechanics in general relativity and post-newtonian theory. *Physical Review D*, 85(6), March 2012.

[71] Alejandro Bohé, Sylvain Marsat, Guillaume Faye, and Luc Blanchet. Next-to-next-to-leading order spin–orbit effects in the near-zone metric and precession equations of compact binaries. *Classical and Quantum Gravity*, 30(7):075017, March 2013.

[72] Geraint Pratten, Cecilio Garcia-Quiros, Marta Colleoni, Antoni Ramos-Buades, Hector Estelles, Maite Mateu-Lucena, Rafel Jaume, Maria Haney, David Keitel, Jonathan E. Thompson, and Sascha Husa. Computationally efficient models for the dominant and subdominant harmonic modes of precessing binary black holes. *Physical Review D*, 103(10), may 2021.

[73] Luc Blanchet, Alessandra Buonanno, and Guillaume Faye. Higher-order spin effects in the dynamics of compact binaries. ii. radiation field. *Physical Review D*, 74.

[74] Bohe Alejandro, Mark Hannam, Sascha Husa, Frank Ohme, Michael Puerrer, and Patricia Schmidt. Phenompv2 technical notes for lal implementation. *LIGO Technical Document, LIGO-T1500602-v4*, 2016.

[75] Marta Colleoni, Cecilio Garcia-Quiros, Sascha Husa, David Keitel, Maite Mateu-Lucena, Maria de Lluc Planas, and Antoni Ramos-Buades. New twists in compact binary waveform modeling: A fast time-domain model for precession. *Physical Review D*, 105(8), apr 2022.

[76] Patricia Schmidt, Frank Ohme, and Mark Hannam. Towards models of gravitational waveforms from generic binaries: Ii. modelling precession effects with a single effective precession parameter. *Physical Review D*, 91(2):024043, 2015.

[77] Patricia Schmidt, Mark Hannam, and Sascha Husa. Towards models of gravitational waveforms from generic binaries: A simple approximate mapping between precessing and nonprecessing inspiral signals. *Physical Review D*, 86(10):104063, 2012.

[78] Maite Mateu-Lucena, Sascha Husa, Marta Colleoni, Hector Estelles, Cecilio Garcia-Quiros, David Keitel, Maria de Lluc Planas, and Antoni Ramos-Buades. Parameter estimation with the current generation of phenomenological waveform models applied to the black hole mergers of GWTC-1. *Monthly Notices of the Royal Astronomical Society*, 517(2):2403–2425, oct 2022.

[79] T Adams, D Buskulic, V Germain, G M Guidi, F Marion, M Montani, B Mours, F Piergiovanni, and G Wang. Low-latency analysis pipeline for compact binary coalescences in the advanced gravitational wave detector era. *Classical and Quantum Gravity*, 33(17):175012, August 2016.

[80] F Aubin, F Brighenti, R Chierici, D Estevez, G Greco, G M Guidi, V Juste, F Marion, B Mours, E Nitoglia, O Sauter, and V Sordini. The mbta pipeline for detecting compact binary coalescences in the third ligo–virgo observing run. *Classical and Quantum Gravity*, 38(9):095004, April 2021.

[81] Francesco Piergiovanni. *Detectors characterization and low latency search of gravitational waves from binary neutron stars*. PhD thesis, Urbino U., 2 2016.

[82] Surabhi Sachdev, Sarah Caudill, Heather Fong, Rico KL Lo, Cody Messick, Debnandini Mukherjee, Ryan Magee, Leo Tsukada, Kent Blackburn, Patrick Brady,

et al. The gstlal search analysis methods for compact binary mergers in advanced ligo's second and advanced virgo's first observing runs. *arXiv preprint arXiv:1901.08580*, 2019.

[83] T Adams, D Buskulic, V Germain, GM Guidi, F Marion, Matteo Montani, B Mours, Francesco Piergiovanni, and Gang Wang. Low-latency analysis pipeline for compact binary coalescences in the advanced gravitational wave detector era. *Classical and Quantum Gravity*, 33(17):175012, 2016.

[84] Bruce Allen. χ 2 time-frequency discriminator for gravitational wave detection. *Physical Review D*, 71(6):062001, 2005.

[85] Gianluca M Guidi. A time-domain veto for binary inspirals search. *Classical and Quantum Gravity*, 21(20):S1767, 2004.

[86] Peter Shawhan and Evan Ochsner. A new waveform consistency test for gravitational wave inspiral searches. *Classical and Quantum Gravity*, 21(20):S1757, 2004.

[87] Cody Messick, Kent Blackburn, Patrick Brady, Patrick Brockill, Kipp Cannon, Romain Cariou, Sarah Caudill, Sydney J Chamberlin, Jolien DE Creighton, Ryan Everett, et al. Analysis framework for the prompt discovery of compact binary mergers in gravitational-wave data. *Physical Review D*, 95(4):042001, 2017.